Mix, A.C., Tiedemann, R., Blum, P., et al., 2003
Proceedings of the Ocean Drilling Program, Initial Reports Volume 202

6. SITE 1235[1]

Shipboard Scientific Party[2]

INTRODUCTION

Site 1235 (proposed Site SEPAC-14A) is located at 36°9.594′S, 73°33.983′W on a gently sloping terrace on the upper continental slope, at 489 m water depth, ~65 km shoreward of the Peru-Chile Trench and ~60 km offshore (Fig. **F1**). Basement is likely continental crust. The continental shelf here is ~60 km wide. Predrilling surveys indicate hemipelagic sedimentation at the site as indicated by gravity cores and seismic data (970312 *Revelle,* Mix et al., 1998; SO161-5, *Sonne,* Wiedicke-Hombach et al., 2002). The uppermost part of the seismic profile shows well-stratified, flat-lying, strong reflectors (Fig. **F2**). Farther below, deformed but continuous layers of moderate reflection are believed to smooth the original relief of the acoustic basement. This site was chosen to take advantage of the expected high sedimentation rates to decipher the late Quaternary history of continental climate and southeast Pacific oceanography on millennial to centennial timescales. Small canyons to the north and south of the site appear to channel most turbidity currents away from this shallow basin.

Site 1235 is ~7 km northeast of Site 1234 (1015 m water depth) but is located upslope in shallower waters (Fig. **F1**). These two sites are expected to be influenced by similar surface water conditions, so major differences in physical, chemical, and paleontological properties can be attributed to depth-related effects.

The regional surface circulation at both sites is marked by the northward-flowing Peru-Chile Current (PCC) and the Coastal Current (CC), which are separated by the poleward-flowing Peru-Chile Counter Current (PCCC) (Strub et al., 1998) (Fig. **F3A**). The PCC and the CC transport cold, nutrient-enriched subpolar water masses northward, whereas the CCC is significantly affected by admixture of low-salinity waters from the Chilean fjord region (Fig. **F3B**). The PCCC stretches from 100 to 300 km offshore and transports subtropical surface water to the

F1. Three-dimensional bathymetry image of Sites 1234 and 1235, p. 20.

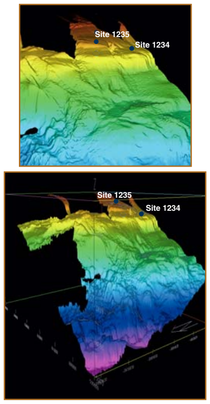

F2. Seismic profile at Site 1235, p. 21.

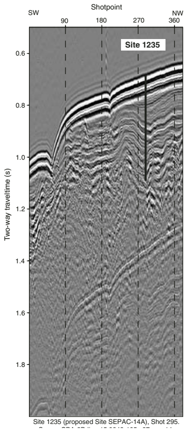

F3. Sites 1232–1235 and oceanographic features off southern and central Chile, p. 22.

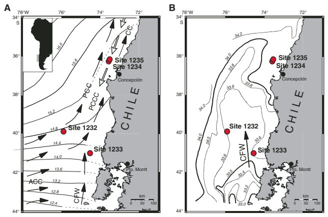

---

[1] Examples of how to reference the whole or part of this volume.
[2] Shipboard Scientific Party addresses.

Ms 202IR-106

south. Beneath these surface currents, at a depth of 100–400 m, the poleward-flowing Gunther Undercurrent (GUC) transports relatively low-oxygen and high-salinity water masses near the shelf edge. These nutrient-rich water masses provide the source of nearshore upwelled waters (Fonseca, 1989). At both sites, seasonal upwelling favors a high biogenic productivity during southern summer as long as wind directions from south to south-southwest dominate. During extreme upwelling events, upwelling of very low oxygen water from the GUC has caused fish kills (Ahumada, 1989). During winter, dominant wind directions from the north significantly reduce coastal upwelling (Strub et al., 1998).

The water depth of 489 m at Site 1235 reflects the modern transition zone between the relatively low-oxygen, high-salinity, nutrient-rich GUC and the relatively high-oxygen, low-salinity, nutrient-poor Antarctic Intermediate Water (AAIW) (Fig. F4). We expect that benthic proxies will reflect temporal and vertical changes of these water masses on millennial to centennial timescales throughout the late Quaternary.

F4. North-south cross section of water masses, p. 23.

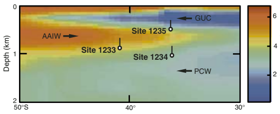

The continental climate of southern Chile constitutes a transition zone between summer-dry Mediterranean climates to the north and heavy year-round rainfall to the south of Site 1235, due to the influence of westerly winds. Interannual rainfall in this region of Chile is thought to reflect the influence of El Niño Southern Oscillation (ENSO) events emanating from the tropics (Hebbeln et al., 2000; Dettinger et al., 2001). Modern sediments on the southern Chile continental slope are primarily provided by rivers (Lamy et al., 2002). We expect variations in terrigenous sediment composition and mineralogy at Site 1235 to reflect changes in the latitudinal position of the westerly winds through time.

Primary goals of Site 1235 were to

1. Assess the late Quaternary history of biological production in a coastal upwelling center near Concepción, Chile, which is sensitive to regional winds, with millennial- to centennial-scale resolution;
2. Assess the late Quaternary history of terrigenous sedimentation off central Chile indicative of continental climate variability;
3. Assess variations in the boundary between oxygen-depleted GUC water, oxygen-rich AAIW, and oxygen-depleted Pacific Central Water (PCW) using tracers of paleo-oxygen and paleonutrients; and
4. Assess late Quaternary variations in paleomagnetic intensities in the southeast Pacific as a stratigraphic tool for comparison with similar data from the Northern Hemisphere.

OPERATIONS

The vessel was offset 7.0 nmi to Site 1235 (proposed Site SEPAC-14A) with the drill string deployed to 375 m and using the dynamic positioning system. The transit took 5.5 hr at an average speed of 1.3 kt. The 3.5-kHz precision depth recorder (PDR) was monitored throughout the transit and was used as a final check of site characteristics by comparison to precruise survey data. The vessel was on location at 0412 hr on 17 April 2002.

Hole 1235A

Hole 1235A was initiated with the advanced piston corer (APC) at 0603 hr on 17 April, with the bit at 494.0 meters below rig floor (mbrf). Core 1H recovered the mudline, indicating a seafloor depth of 500.7 mbrf, 1.7 m shallower than the corrected PDR depth estimate. Piston coring deepened the hole until Core 20H failed to achieve a full stroke at 181.3 meters below seafloor (mbsf). The recovery was 182.8 m (Table T1). Cores were oriented starting with Core 4H. Downhole temperature measurements were taken with the APC temperature (APCT) tool (Table T1). Most cores were afflicted with voids from gas that expanded during the retrieval process. Holes were drilled into the core liners to relieve some of the gas pressure before cores were processed on the catwalk. No extended core barrel (XCB) cores were attempted at this site based on the experience at Site 1234 and because of the coring disturbance associated with gas expansion and ship heave. The bit was pulled free of the seafloor at 1955 hr on 17 April.

T1. Operations summary, Site 1235, p. 51.

Hole 1235B

The vessel was offset 10 m east relative to Hole 1235A. A bottom water temperature measurement was first obtained with the APCT tool and the bit at 497 mbrf. This was also the bit depth to accomplish the desired stratigraphic overlap with the first hole. Hole 1235B was initiated with the APC at 2100 hr. The mudline was again recovered, indicating a seafloor depth of 499.5 mbrf. Piston coring advanced to the APC refusal depth of 176.2 mbsf. The last core (Core 19H) sustained liner damage resulting from deceleration forces incurred when the formation prevented a full stroke of the corer. The cores were oriented starting with Core 3H. Of the 176.2 m of sediment cored, 178.5 m was recovered (recovery = 101%) (Table T1). Downhole temperature measurements were taken with Cores 4H and 7H (35.5 and 64.0 mbsf, respectively). The bit was pulled free of the seafloor at 1000 hr on 18 April.

When the liner of Core 16H was being cut into sections on the catwalk, it suddenly fragmented into countless pieces and the sediment exploded as a result of gas pressure. The core was completely destroyed. Following this incident, the marine laboratory specialists wore plastic face shields and used Kevlar blankets while carrying the core to the core receiving platform as a precaution against possible injury.

Hole 1235C

The vessel was offset 10 m east of Hole 1235B. A second bottom water temperature measurement was taken before we cored Hole 1235C. Combined with all temperature measurements in the previous holes, a thermal gradient of ~3.8°C/100 m was determined for this site. The bit was positioned at a depth of 500 mbrf (0.5 mbsf in Hole 1223B) in order to cover the remaining stratigraphic gaps. Hole 1235C was initiated with the APC at 1110 hr on 18 April. Because this hole was started with the bit below the mudline, the inferred seafloor depth from the previous hole was assumed for Hole 1235C (499.5 mbrf). Piston coring had advanced to 152.5 mbsf when operations concluded at the site. A total of 152.0 m was cored and 151.8 m was recovered (recovery = 99.9%) (Table T1). The cores were oriented starting with Core 3H.

The nonmagnetic (monel) core barrel was deployed for the first time during Leg 202 (Cores 3H, 5H, 7H, 9H, and 11H) after an excessive magnetic overprint was discovered in connection with APCT tool deployments. Cores retrieved with the monel barrel turned out to have less overprint than those retrieved in the regular steel barrels.

This site was under the influence of a strong southerly wind that gradually built through the duration of the afternoon of 17 April and continued into the next day. The combined sea and swell eventually grew to >25 ft by the afternoon of 18 April and was responsible for an average vessel heave of 4 m. The combination of heave and gas expansion compromised the quality of the cores at this site.

The vessel was secured for transit and left location at 2300 hr on 18 April for the 4-day transit to Site 1236, the first site in Peruvian waters.

COMPOSITE SECTION

We built a composite depth scale (as defined in **"Composite Section,"** p. 4, in the "Explanatory Notes") that ranges from the top of Core 202-1235C-1H to the bottom of Section 202-1235A-20H-7 (0.00–214.38 meters composite depth [mcd]) (Table **T2**) and a splice (as defined in **"Composite Section,"** p. 4, in the "Explanatory Notes" chapter) for the upper 151.42 mcd. The splice ranges from the top of Core 202-1235A-1H to the bottom of Section 202-1235B-17H-7 (0.00–188.55 mcd). The splice is continuous to 63.97 mcd. Below this, we constructed four intervals of a floating splice. The mcd scale and splice are based on the stratigraphic correlation of whole-core magnetic susceptibility data from the ODP multisensor track (MST-MS) sampled at 2.5-cm intervals and data from the Oregon State University Fast Track (OSUS-MS) collected at 5-cm depth intervals (Tables **T3, T4, T5**). These data were complemented by other data from the multisensor track (MST) and by gamma ray attenuation (GRA) bulk density, natural gamma radiation (NGR), color reflectance (measured on the archive-half multisensor track), and magnetic intensity measurements from the cryogenic magnetometer track. The composite section and splice of MST-MS are illustrated in Figure **F5.**

T2. Composite depth scale, p. 52.

T3. OSUS-MS measurements, Hole 1235A, p. 53.

T4. OSUS-MS measurements, Hole 1235B, p. 54.

T5. OSUS-MS measurements, Hole 1235C, p. 55.

F5. MS vs. mcd, p. 24.

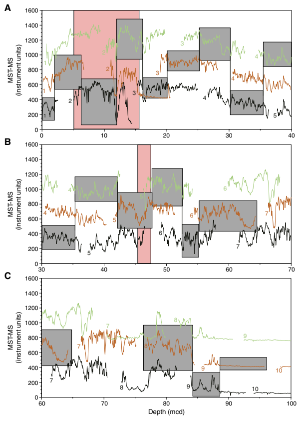

It is likely that a complete sediment section was recovered in the three holes drilled at Site 1235. However, significant ship heave, combined with gas expansion of cores recovered at Site 1235, led to poor correlation between MST data from adjacent holes in some intervals, and this made the construction of a composite section and a spliced record somewhat uncertain. In two intervals within the splice, precise correlation is problematic using available shipboard data. The first is at 4–16 mcd (between the top and bottom of Core 202-1235A-2H; Fig. **F5A**). The second is at ~45–49 mcd (between the base of Core 202-1235A-5H and the top of Core 6H; Fig. **F5B**). Core 202-1235B-5H may span this gap. In these two intervals, splice tie points are somewhat uncertain because of the poor correlation of the shipboard data between holes. Below Core 202-1235B-6H (63.97 mcd) there is a gap in the splice. The first section of floating splice begins at the top of Core 202-1235B-8H (76.54 mcd) and ends at the bottom of Core 202-1235B-9H (95.44 mcd) (Fig. **F5C**). The second section of floating splice begins at the top of Core 202-1235A-11H (103.87 mcd) and extends to the bottom of Core 202-1235B-11H (117.23 mcd) (Fig. **F5D**). The third section of floating splice begins at the top of Section 202-1235A-15H-1 (150.12 mcd) and ends at the bottom of Core 15H (163.93 mcd) (Fig. **F5E, F5F**).

The fourth section of floating splice begins at the top of Core 202-1235A-17H (175.55 mcd) and extends to the bottom of Section 17H-7 (188.55 mcd) (Fig. F5F, F5G). Tie points (Table T6) were then used to construct representative spliced records for MST track magnetic susceptibility (MST-MS), GRA bulk density data, and NGR attenuation (Fig. F6). Although the susceptibility in cores covering the interval 90–100 mcd is low (~30 instrument units), careful inspection of these data combined with other MST data supports the correlations shown in Figure F5C and F5D. Below Core 202-1235B-17H (~189 mcd) we cannot confirm continuous recovery (Fig. F5G).

T6. Splice tie points, p. 56.

F6. NGR, GRA bulk density, and MST-MS, p. 27.

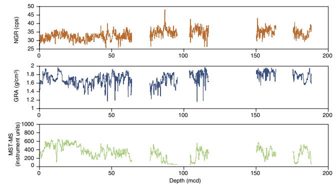

To aid in the construction of the composite section, as a first approximation we assumed an expansion factor of 13% to the top depth of all cores drilled at Site 1235. In the upper interval, where continuous recovery was documented, we found an expansion factor of 20%. The final expansion of 20% (Table T2) was applied to all cores below 172 mcd that could not be correlated (Fig. F5).

To facilitate the calculation of mass accumulation rates (MARs), we provide corrected meters composite depth (cmcd) in Table T2. The mcd growth factor for the composite interval at Site 1235 is 1.20 (Fig. F7).

F7. A comparison of mbsf and mcd scales, p. 28.

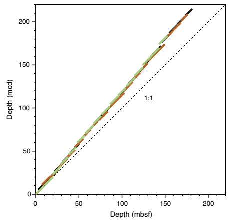

LITHOSTRATIGRAPHY

A 181.44-m-thick (214.46 mcd) hemipelagic sediment sequence from the late Quaternary was recovered from three holes at Site 1235. A single lithologic unit, Unit I, was defined on the basis of visual core description and smear slide analysis (Table T7). Lithologic Unit I is composed primarily of siliciclastic silty clay, with little lithologic variability. Millimeter-scale silt-rich layers and macrofossils (bivalves and gastropods) are present throughout the cored interval. The silt fraction is dominated by feldspar, with lesser amounts of quartz, pyroxenes, and volcanic glass. Biogenic components, mainly nannofossils and diatoms, are low, ranging from 0% to 18% of the sediment. The authigenic components, pyrite and disseminated authigenic carbonate, are present in variable abundance, and carbonate concretions are intermittently present downhole.

T7. Lithologic Unit I, p. 57.

Distinct minima in magnetic susceptibility associated with color reflectance maxima in b* (yellowish) and minima in a* (greenish) may indicate reductive diagenesis. Values of NGR are relatively constant until 180 mcd, where they increase by ~20 cps (Fig. F8). Sediment color varies between dark olive gray, olive gray, and, to a lesser extent, gray.

F8. Lithostratigraphic summary, p. 29.

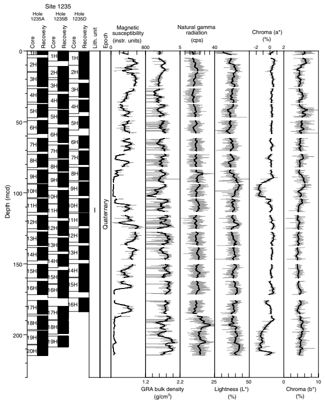

Overall, the sequence at Site 1235 represents rapidly accumulating hemipelagic sediments dominated by siliciclastics. Fossil biogenic components are typical of an active upwelling zone on a continental margin, and the presence of burrows and benthic faunal components reveals no episodes of bottom water anoxia. Microbial degradation of organic matter resulted in the formation of methane (and perhaps methane hydrate) and authigenic minerals deeper in the section.

Description of Lithologic Unit

Unit I

Intervals: Cores 202-1235A-1H through 20H; Cores 202-1235B-1H through 19H; and Cores 202-1235C-1H through 16H

Depths: Hole 1235A: 0.00–181.44 mbsf (0.00–214.46 mcd); Hole 1235B: 0.00–176.34 mbsf (0.10–208.41 mcd); and Hole 1235C: 0.50–152.86 mbsf (0.59–183.57 mcd).
Age: late Quaternary (<0.26 Ma)

The dominant lithology defining Unit I is a massive unit of silty clay with dispersed fragments of bivalves and gastropod fossils. Three minor lithologies with irregular distributions have been identified in Unit I: (1) silt-rich layers and patches, (2) authigenic carbonate-rich horizons (nodules and layers), and (3) an ash layer. Color changes are gradual, from dark olive gray to olive gray and gray, with the exception of a few distinct shifts toward light olive associated with the occurrence of carbonate concretions. Unstable iron monosulfides, which dissipated after 1–1.5 hr of exposure, are abundant at depths above 40 mcd. Bioturbation is pervasive. As a result of degassing after recovery, occasional larger voids and abundant small tissues are present in sediments throughout the sections in all three holes.

Siliciclastic components are dominated by clay minerals. Silt contents range from ~10% to 40% (Fig. **F9**). The primary minerals found in the silt fraction of the silty clay include feldspar, quartz, and pyroxenes; all increase in abundance within the relatively silt-rich intervals (30%–45% silt) observed at 50, 115, and 140 mcd. Enrichment of volcanic glass occurs mainly between 30 and 60 mcd, with a distinct peak at 40 mcd. Below ~130 mcd, percentages increase slightly (Fig. **F9**).

F9. Siliciclastic, biogenic, and authigenic components, p. 30.

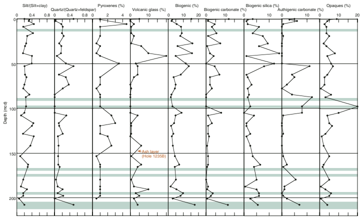

Calcareous nannofossils, diatoms, and lesser amounts of sponge spicules dominate the biogenic fraction. Foraminifers, radiolarians, and silicoflagellates are rare. Carbonate components, including nannofossils, foraminifers, and carbonate bioclasts, are grouped here as biogenic carbonate fraction, whereas diatoms, radiolarians, sponge spicules, and silicoflagellates make up the biogenic silica fraction (Fig. **F9**). Both biogenic fractions are more abundant in the upper part of the hole but decrease downhole from 50 mcd. The biogenic silica fraction again increases below 130 mcd, whereas the biogenic carbonate fraction remains relatively low to ~190 mcd, where it too increases (Fig. **F9**). Authigenic carbonate is common, and occasional carbonate nodules are present in intervals bearing <5% nannofossils and rare to absent foraminifers (Fig. **F9**). Opaque minerals, mainly authigenic pyrite, range in abundance from 0.5% to 20%. A notable peak in opaque minerals at 98 mcd is associated with an authigenic carbonate–rich interval (Fig. **F9**).

The most common minor lithology in Unit I comprises silt-rich layers and patches. With the exception of one layer (>1 cm) at 12.76 mcd, silt-rich layers are mostly millimeter scale and are randomly distributed downhole. Regardless of thickness, the silt layers appear more frequently in the top half of the drilled interval. In general, silt-rich layers have bioturbated contacts. Silty patches (0.5–3.0 cm thick and occasionally as long as 40 cm) are frequent and often related to bioturbation and/or represent the infilling of burrow traces. The silt within the discrete layers and patches has a mineralogic composition similar to the silt dispersed in the major lithology.

Authigenic carbonate, as nodules and partially lithified sediment layers, represents the second minor lithology. One of the nodules (interval 202-1235C-10H-1, 20–21 cm) had carbonate concentrations of ~55%. X-ray diffraction results from another nodule (interval 202-1235B-2H-6, 5–10 cm) demonstrated the dominant composition to be dolomite (Fig. **F10**). The nodules range in size from 2 to 15 cm. The partially lithified authigenic carbonate–rich sediment is present as 10- to 15-cm-thick lay-

F10. Authigenic carbonate nodule. p. 31.

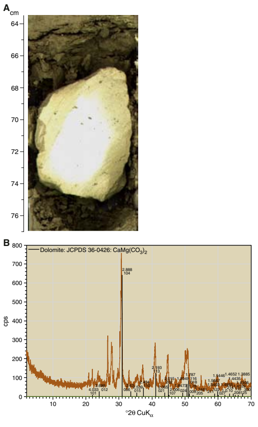

ers. This lithology, whether a completely formed nodule or a partially lithified layer, is typically present within light olive-colored sediment enriched in authigenic carbonate (Fig. **F10**). In addition, these intervals have characteristically low values in both magnetic susceptibility and a* color reflectance (Fig. **F11**). The carbonate-rich layers and nodules are present within intervals of authigenic carbonate–rich light olive-green sediments, which appear below a thick package (0.8–6 m) of highly bioturbated sediment that includes abundant color mottles, silty patches, and long burrows (up to 40 cm) apparently created by macrobenthic fauna (Fig. **F12**). Three examples of this facies succession, ranging in thickness from 3 to 16 m, are clearly recognizable and correlative among Holes 1235A, 1235B, and 1235C.

A 5- to 6-cm-thick pale ash layer represents the third minor lithology and is present only in Hole 1235B at 150.5 mcd (Fig. **F13**). The base of the ash has a sharp, scoured contact. Several ash patches 5–10 cm below the ash layer indicate bioturbation. The ash is composed mainly of volcanic glass shards associated with minor amounts of labradorite plagioclase and trace amounts of quartz, mica, amphiboles, and orthopyroxene.

Magnetic susceptibility at Site 1235 varies between 20 and 780 instrument units over most intervals. Four distinct extended intervals of low magnetic susceptibility are present at ~74–77, ~89–103, ~169–178, and ~188–214 mcd (Figs. **F8, F11**). Loss of magnetic minerals in these low-susceptibility intervals is presumably the result of strong reductive diagenesis (see **"Paleomagnetism,"** p. 11).

GRA bulk density (Fig. **F8**) and moisture and density (MAD) measurements (Fig. **F14**) track one another with a variable offset of ~0.1 to 0.3 g/cm^3 (Fig. **F15**). GRA data are noisy, presumably because of gas-related voids and fissures. The slight downhole increases in both GRA and MAD bulk densities and the decrease in porosity (Figs. **F8, F14**) are usually ascribed to compaction and dehydration. Bulk density and porosity may be affected by local diagenesis below ~180 mcd (Fig. **F14**) through textural modifications and cementation (e.g., authigenic carbonate precipitation) (see above and Fig. **F11**). The uppermost ~50 m of sediments exhibits low bulk density and high porosity (Fig. **F14**) that could be related to an increased content of biogenic silica (Fig. **F9**), which tends to keep pore spaces open with a more rigid structure (e.g., Silva et al., 1976).

In the a*-b* color space, all color measurements at Site 1235 plot in the "yellow" (b* positive) domain (Fig. **F16**). As at Site 1234, they exhibit a weak bimodal distribution, with one trend characteristic of brownish sediments (a* > 0) and the other representing more greenish sediments (a* < 0). Assuming a two-component chromatic system, preliminary predictive relationships between reflectance, carbonate, and total organic carbon (TOC) via a multiple linear regression are weaker than at Site 1233 for carbonate (r^2 = ~0.3) but stronger for TOC (r^2 = ~0.8).

The greenest sediments are present in diagenetically modified intervals (i.e., in magnetic susceptibility lows) and coincide with relatively high abundances of pyrite and sulfur (see **"Geochemistry,"** p. 13). Therefore, we infer that the green hue is the result of an increased Fe^{2+}/Fe^{3+} ratio in clay mineral structural iron due to intense sulfate reduction (e.g., Lyle, 1983; Giosan, 2001). These diagenetically modified intervals also show a consistent color pattern (Fig. **F11**), starting with a brownish zone (a* > 0) that passes into an increasingly green zone (increasing a*,

F11. Magnetic susceptibility and a*, p. 32

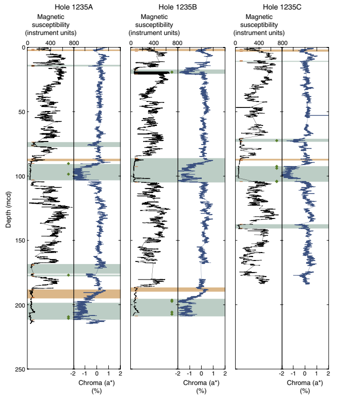

F12. Color transition and bioturbated sequence, p. 33.

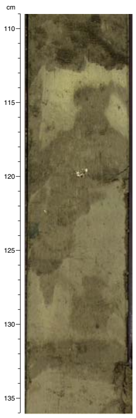

F13. Ash layer, p. 34.

F14. Moisture and density, p. 35.

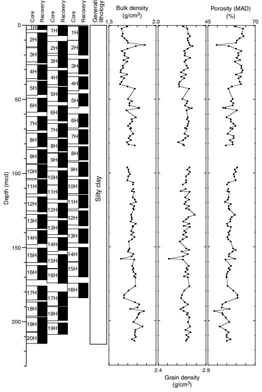

but with a* < 0) farther downhole. The brownish zones also contain hematite and probably goethite (Fig. **F17**).

Interpretation and Depositional History

The entire cored interval falls within nannofossil Zone NN21 (<0.26 Ma) (see **"Biostratigraphy,"** p. 9). The hemipelagic sedimentation is dominated by siliciclastic materials containing abundant feldspar, with minor quartz, pyroxenes, and volcanic glass, indicating a dominant Andean source for siliciclastic material. This composition is typical for surface sediments from the Chile margin between 25° and 43°S (Lamy et al., 1998). The dominance of the siliciclastic component and the extremely high sedimentation rates of >800 m/m.y. suggest a significant fluvial contribution by the nearby rivers (Bío-Bío and Itata). Although turbidites are channeled away from Site 1235 in large canyons, the presence of very thin silt-rich layers might be associated with distal turbidite or dilated overflow deposits.

The one volcanic ash layer, composed primarily of volcanic glass and trace labradorite plagioclase, is intermediate in composition and is likely derived from volcanism originating in the nearby Andes. An interval enriched in volcanic glass is present between 30 and 60 mcd, with a pronounced peak at 40 mcd, indicating increased volcanic activity and delivery of disseminated ash during this interval.

Site 1235 currently underlies a highly productive coastal upwelling zone off Chile. The relatively low percentages of biogenic components together with low TOC values (see **"Geochemistry,"** p. 13, for TOC concentrations) indicate that the signal of highly productive surface waters is strongly diluted by the terrigenous components. Evidence for high surface water productivity includes the common presence of an active macrofaunal population. The pervasive gas-produced fissures and voids also are consistent with the interpretation that abundant biogenic components, including organic carbon, are reaching the sediment, even if they are not well preserved and/or are diluted.

The decrease in biogenic components at >60 mcd may reflect increased dilution by terrigenous sediment or a decrease in either preservation or deposition of biogenic components. We found no systematic trends in the silt/(silt+clay) values or in the presence of silty layers and patches. However, the increased presence of both opaques (pyrite) and authigenic carbonate in discrete intervals is consistent with diagenesis and decreased biogenic carbonate preservation. These intervals likely represent times of enhanced productivity, with organic carbon and carbonate fluxes that led to intense biogenic carbonate dissolution, sulfate reduction, and precipitation of authigenic carbonate. Sulfate reduction is required to generate both the reduced sulfur and increased alkalinity sufficient to drive the formation of authigenic pyrite and carbonate, respectively. Organic carbon is the primary energy source to drive these reactions within the sediment. Variability in the bottom water oxygen characteristics could also drive the sedimentary system toward increased sulfate reduction, producing these diagenetic processes without an intensification of productivity. At present, Site 1235 lies near the boundary between the low-oxygen GUC and oxygen-rich AAIW. If the position of the GUC changed with time, either as the result of sea level changes or general variability in circulation, it may have modulated the oxidation rate of organic matter near the sediment/water interface.

The facies succession, with strongly bioturbated sediment overlying the enrichments in authigenic carbonate, indicates a repetitive pattern

F15. MAD and GRA bulk densities, p. 36.

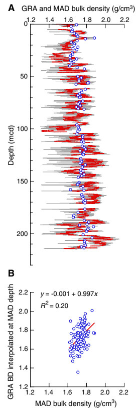

F16. Color measurements, p. 37.

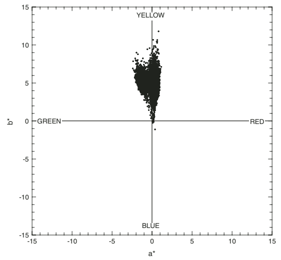

F17. First derivatives of reflectance, p. 38.

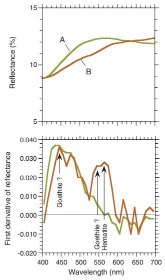

in the sequence of sedimentation. The presence of hematite and goethite demands preservation of former oxic zones that lay above strongly reduced green sediments containing authigenic carbonate and pyrite. The mineralogy and color are consistent with zones of strong redox gradients that are typical for periods of drastic change in sedimentation rates (e.g., Thomson et al., 1996; Giosan, 2001).

BIOSTRATIGRAPHY

Calcareous nannofossils, diatoms, and planktonic and benthic foraminifers were examined in mudline and core catcher samples from Hole 1235A. Calcareous nannofossils and diatoms were also examined in additional samples from all core sections of Hole 1235A. Drilling at Site 1235 revealed one major biostratigraphic unit of late Pleistocene age. The microfossils of this site are similar to those of Site 1234. The abundance of calcareous microfossils varies from rare to common, although a few samples are also barren (Fig. **F18**). Preservation of the four groups (calcareous nannofossils, diatoms, and planktonic and benthic foraminifers) is generally moderate. Reworking of microfossils, mainly from Neogene sediments, is apparent to some extent in all the fossil groups examined. In particular, benthic diatoms are present in most of the samples, indicating relatively persistent redeposition from the upper continental margin. Changes in benthic foraminiferal assemblages reflect variations in oxygenation in the bottom water masses. Calcareous nannofossils suggest that the base of the cored sequence is younger than 0.26 Ma (Zone NN21).

F18. Calcareous nannofossils, planktonic and benthic foraminifers, and diatoms, p. 39.

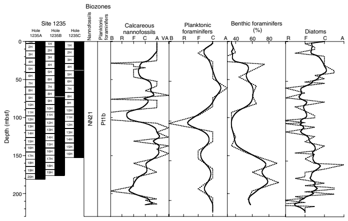

Calcareous Nannofossils

Calcareous nannofossil distribution and biostratigraphy at Site 1235 are similar to those at Site 1234. The main difference appears to be the generally lower abundance of nannofossils at this shallower water site. Calcareous nannofossils are mostly common and moderately well preserved in the upper 16 cores (Hole 1235A; 0–171.8 mcd) and are generally rare to few and poorly preserved in the lowermost four cores (Cores 202-1235A-17H through 20H; 171.8–214.7 mcd) (Table **T8**).

T8. Distribution of calcareous nannofossils, p. 58.

Common *Emiliania huxleyi* is found down to Sample 202-1235A-3H-CC (below which the species is generally rare to few) and is observed down to Sample 20H-7, 40 cm (213.8 mcd) at the base of the hole; this suggests an age younger than 0.26 Ma for the entire sediment sequence cored at this site (Table **T8**), corresponding with Zone NN21 (Martini, 1971). As at Site 1234, the *E. huxleyi* acme zone is difficult to delineate because of the abnormal abundance of the species. The reversal in abundance between medium-sized gephyrocapsids (mainly *Gephyrocapsa muellerae*) and *E. huxleyi* is not clear, based on current data. As at Site 1234, the relative abundances of the nannofossil taxa, especially those of *Helicosphaera carteri, Calcidiscus leptoporus,* and *Coccolithus pelagicus,* show significant changes at the site, presumably in responding to changes in surface-water properties.

Planktonic Foraminifers

Planktonic foraminifers are present in all samples, but abundance varies markedly (Table **T9**). For instance, Sample 202-1235A-10H-CC (103.1 mcd) is virtually barren, containing only a few poorly preserved

T9. Distribution of foraminifers, p. 59.

tests. Except for a few samples, tests are moderately well preserved overall and a significant number of tests are pyritized at distinct levels. The planktonic foraminiferal assemblage includes *Globorotalia truncatulinoides, Globorotalia inflata, Globorotalia scitula, Globorotalia ungulata, Globigerina bulloides, Globigerinita glutinata, Neogloboquadrina dutertrei, Neogloboquadrina pachyderma,* and *Orbulina universa*. This assemblage is present down to Sample 202-1235A-20H-CC (214.7 mcd), indicating the upper Pleistocene Subzone Pt1a of Berggren et al. (1995) (Fig. **F12,** p. 63, in the "Explanatory Notes" chapter). Changes in assemblage composition offer the potential to monitor variations in the intensity and position of the upwelling system with time.

Benthic Foraminifers

Benthic foraminifers are generally frequent to common (representing between 15% and 92% of the total foraminiferal assemblage) and are moderately well preserved, although a significant proportion of tests are pyritized at discrete levels. To assess assemblage composition and variability downhole, ~200 specimens from the >150-µm fraction were picked from each sample. Specimens were mounted onto slides prior to identification and counting. A total of 34 taxa were identified (Table **T9**). Common species are *Bolivina seminuda, Bolivina costata, Cassidulinoides bradyi, Eubuliminella exilis, Globobulimina pyrula, Globobulimina affinis, Nonionella auris, Nonionella stella, Planulina wuellerstorfi, Protoglobobulimina pupoides, Rotaliatinopsis semiinvoluta, Rutherfordoides mexicanus,* and *Uvigerina peregrina.*

The assemblages from Sites 1234 and 1235 are similar. Both are strongly dominated by high carbon-flux indicators typical of oxygen minimum zone environments and show marked changes in composition downhole, particularly in the relative proportion of *Bolivina* spp., *Globobulimina* spp., *Uvigerina* spp., and *Nonionella* spp. (Fig. **F19**). However, there are significant differences in species distribution between the two sites. For instance, the species *Bulimina mexicana* is virtually absent at Site 1235, whereas it shows marked fluctuations in numbers at Site 1234. The species *C. bradyi, E. exilis, R. semiinvoluta,* and *R. mexicanus* overall are more abundant at Site 1235 than at Site 1234. A distinct peak in the abundance of *Bolivina* spp. is observed at ~75–115 mcd (>40% of total benthic foraminifers), which points to an intense episode of seafloor dysoxia (Fig. **F19**) that may be linked to intensification of the GUC or perhaps a deepening of this undercurrent relative to the site, which is associated with Pleistocene sea level change.

F19. Variations in percent of benthic foraminifers, p. 40.

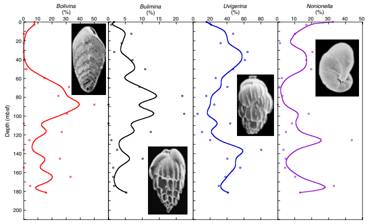

In spite of the somewhat poorer preservation at Site 1235 than at Site 1234, benthic foraminifers have good potential for investigation of temporal and spatial fluctuations in the upwelling system and water-mass distribution and, in particular, to decipher the relative influence of the GUC, PCW, and AAIW at the two sites.

Diatoms

Given the location of this site, closer to the coastal upwelling area of Concepción than Site 1234, abundant and well-preserved diatoms were expected. However, the core catcher and the split-core samples observed from Hole 1235A revealed lower abundances (frequent to common) and less well preserved diatom assemblages than those found in Hole 1234A (Table **T10**).

T10. Distribution of diatoms, p. 61.

The typical upwelling-related genus, *Chaetoceros* spores, bristles, and vegetative cells dominated the assemblages (Schuette, 1980; Abrantes 1988; Schrader and Sorknes, 1990; Abrantes and Moita, 1999). *Thalassiosira* sp., *Delphineis* sp., *Pseudonitzschia* sp., and *Thalassionema nitzschioides* appear as secondary components of the flora.

Floras are enriched in neritic and heavily silicified forms such as *Actinoptychus senarius* and *Stephanopyxis turris* between the mudline and Samples 202-1235A-3H-CC; 10H-CC; 12H-3, 40 cm; 14H-CC; and 15H-4, 40 cm. Freshwater diatoms are rare to frequent only in three levels: mudline to Sample 202-1235A-3H-CC; Section 8H-3, 40 cm, to 9H-CC; and Section 11H-3, 40 cm, to 13H-CC.

Displaced shallow-water marine benthic diatoms are found throughout the sequence above Core 202-1235A-17H (180 mcd), with higher abundances between the mudline and Section 3H-CC; from Section 10H-CC to 12H-3, 40 cm; and from Section 14H-CC to 15H-4, 40 cm.

Large diatom cells of the genus *Coscinodiscus* were found in the >63-µm fraction in Sample 202-1235A-18H-CC.

Given that biostratigraphically useful diatom species are not observed in Hole 1235A, no age assignments are possible.

Silicoflagellates, radiolarians, sponge spicules, and phytoliths are also observed in most samples.

PALEOMAGNETISM

Natural Remanent Magnetization

The natural remanent magnetization (NRM) of the archive halves of each core section initially was measured and then remeasured after alternating-field (AF) demagnetization at selected levels. Sections obviously affected by drilling disturbance were not measured. Core 202-1235A-1H was AF demagnetized at peak fields of 15, 20, and 25 mT. Cores 202-1234A-2H through 8H were AF demagnetized at 20 and 25 mT. Cores 202-1235A-9H through 20H and all cores from Holes 1235B and 1235C were only AF demagnetized at 25 mT.

Initial NRM intensities were generally high (Fig. F20), ranging from 0.5 to 2.1 A/m, although a few intervals, discussed below, had significantly lower intensities. The high NRM intensities are due, at least in part, to a drill string magnetization overprinting the natural remanence. This overprint, characterized by steep positive inclinations (averaging +79° in the upper 50 mcd of Hole 1235A), was incompletely removed even by demagnetization at peak AF fields up to 25 mT. After demagnetization, the NRM intensities are lower, with an average of ~0.01 to 0.1 A/m (Fig. F20). The ratio of NRM measured after 25-mT AF demagnetization to the initial NRM, ~0.04, is similar in magnitude to that observed at Site 1234 but about a factor of three lower than that observed at Site 1233. As with Site 1234, the lower ratio indicates that the high initial values are a function of a strong overprinting field (likely due to the drill string) affecting coarser (and more magnetically viscous) siliciclastic sediments. The inclinations are also affected by the drill string overprint, with average values after 20- or 25-mT AF demagnetization reduced to approximately –15° in the upper 50 mcd (Fig. F21). This is much shallower than would be expected for the latitude of Site 1235 (about –55° for an axial geocentric dipole during normal polarity), indicating that a significant drill string overprint remains. Calcareous nannofossil data suggest that the base of the cored sequence is

F20. Initial and demagnetized NRM, p. 41.

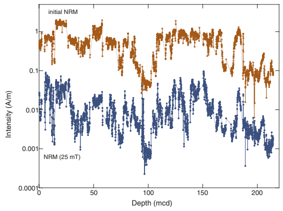

F21. Initial NRM and AF demagnetized inclinations, p. 42.

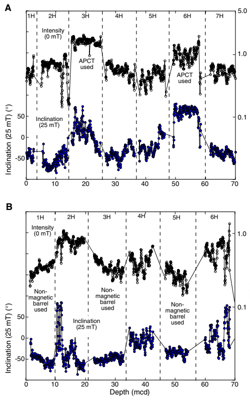

younger than 0.26 Ma (Zone NN21) (see **"Biostratigraphy,"** p. 9); therefore, these sediments were deposited/acquired their NRM during the Bruhnes Chron (0–0.78 Ma) and should be of normal polarity (negative inclinations). The positive inclinations observed below 50 mcd (Fig. **F22**) suggest that the overprint of these sediments is even more severe.

F22. NRM inclination and declination after demagnetization, p. 43.

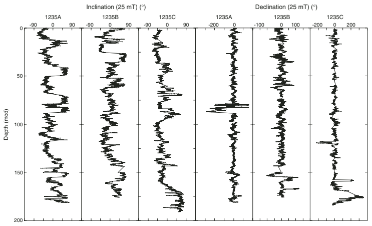

Anomalously large initial NRM intensities were measured in some of the cores from Hole 1235A (Fig. **F21A**), and the inclinations in these cores even after 25-mT AF demagnetization were still positive (overprinted). These cores were collected when the APCT tool was used. The APCT tool was used on Cores 202-1235A-3H, 6H, 9H, and 12H and on Cores 202-1235B-1H, 4H, and 8H. For Section 2 of each core, mean values for the intensity (NRM_{0mT}) and inclination (Inc_{0mT}) prior to demagnetization, the intensity (NRM_{25mT}) and inclination (Inc_{25mT}) after demagnetization at 25 mT, and the ratio of the demagnetized to undemagnetized intensities (NRM_{25mT}/NRM_{0mT}) were determined (Fig. **F23**). Subsequently, we have documented that this pattern of behavior is also apparent for the intermittently stronger NRM overprints at Sites 1232, 1233, and 1234 (see **Lund et al.,** this volume).

F23. Assessment of magnetic overprint strength, p. 44.

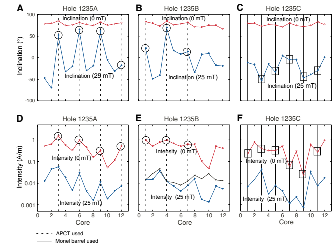

In Hole 1235C, a nonmagnetic core barrel was used in place of one of the two steel core barrels for odd-numbered cores. The NRM_{0mT} and Inc_{25mT} measurements for the first six cores of Holes 1235C showed an alternating pattern of high NRM_{0mT} and positive Inc_{25mT} in the even-numbered cores (normal core barrel) and relatively low NRM_{0mT} and negative Inc_{25mT} in the odd-numbered cores (nonmagnetic barrel) (Fig. **F21**). Therefore, nonmagnetic core barrels may substantially reduce the overprint acquired when coring viscous remanent magnetization–susceptible sediments, possibly improving the paleomagnetic data in such settings. The nonmagnetic core barrel was alternated with a normal (magnetic) core barrel for all remaining sites during Leg 202 to further assess its effect on a variety of sediment types.

Directional Variability

Inclinations after 25-mT AF demagnetization are normally negative (Fig. **F22**), but intermittent intervals of very shallow negative or positive inclinations are due to unremoved overprints. The declinations in Figure **F22** have been averaged within each core and rotated to a zero average. As noted before at Sites 1233 and 1234, the declinations seem to be much less affected by the drilling overprint. The declination patterns observed may reflect paleomagnetic secular variation (Fig. **F22**). The declinations can generally be correlated among the three holes at this site (Fig. **F24**), although not as much detail is initially discernable as was noted at Sites 1233 or 1234. Clearly, caution must be used because this record suffers from magnetic overprints and distinct intervals appear to be affected by time-dependent magnetic dissolution.

F24. Declinations for the Site 1235 splice, p. 45.

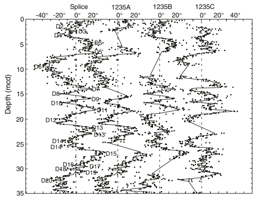

Several intervals below 60 mcd have NRM intensities that are more than one order of magnitude lower than the background sediments, from ~0.05 to 2×10^{-3} A/m (Fig. **F20**). This pattern is analogous to that found at the base of Site 1233 and at Site 1234 and may reflect time-dependent magnetic mineral dissolution associated with early sediment diagenesis.

GEOCHEMISTRY

Sediment Gases

Concentrations of headspace and vacutainer gases were routinely monitored in Hole 1235A sediments according to shipboard safety and pollution prevention considerations (Fig. **F25**; Table **T11**). The high gas pressures in the cores required perforating the core liners to prevent excessive core expansion. Methane concentrations increased rapidly to 55,648 ppmv at 19.6 mcd, and vacutainer samples had high methane concentrations (>95% by volume) at all depths sampled (43.2 to 208.6 mcd). Low ethane (C_2) concentrations were detected in the headspace and vacutainer samples. Ethane values gradually increase with depth and reach 105 ppmv at 208.6 mcd. No significant amounts of higher molecular weight hydrocarbons were observed.

High methane concentrations, low ethane concentrations, and the resulting high C_1/C_2 ratios (Fig. **F25**) indicate that methane originates from in situ formation (methanogenesis) of sedimentary organic matter (Claypool and Kvenvolden, 1983). A biogenic origin for the methane is supported by the disappearance of dissolved sulfate by 19.6 mcd, coincident with the increase in methane.

F25. Headspace and vacutainer methane and C_1/C_2 ratio, p. 46.

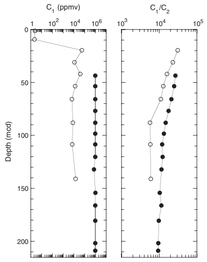

T11. Headspace and vacutainer gases and C_1/C_2 ratio, Hole 1235A, p. 63.

Interstitial Water Geochemistry

We collected 20 interstitial water samples from Hole 1235A. Chemical gradients at this site (Table **T12**; Fig. **F26**) reflect the likely presence of gas hydrates, the influence of organic matter diagenesis by microbially mediated oxidation reactions, a limited degree of biogenic opal dissolution, and the effects of authigenic mineralization reactions on fluid composition.

Chlorinity decreases by more than 12%, from 553 mM at 1.5 mcd to 483 mM by 210.0 mcd (Fig. **F26**). The chlorinity gradient with depth is not as steep as that observed at Site 1233, although both sites have similar chlorinity values from ~75 to 100 mcd. Salinity, measured refractively as total dissolved solids, ranges from 35 to 28, decreasing by ~20% with increasing depth (Table **T12**). Sodium concentrations measured by inductively coupled plasma–atomic emission spectrophotometry were typically within <1% of those estimated by charge balance reported here (Table **T12**). Sodium concentrations decrease by ~20% with depth from a high of 483 mM at 41.7 mcd to 381 mM at 210.0 mcd. Site 1235 was drilled to a greater depth than Site 1233, and the decreases in chlorinity, salinity, and sodium concentrations previously observed at Site 1233 continue through the total depth drilled at Site 1235.

The decreasing chlorinity gradient at Site 1235, like that at Site 1233, is significantly larger than those observed at the deeper-water midslope Peru basin sites drilled during Leg 112 (Sites 682, 683, 685, and 688; Suess, von Huene, et al., 1988). Decomposition of gas hydrates in Site 1235 sediments could explain the observed chloride gradient in interstitial water as a result of dilution, either through in situ decomposition at depth in the sediment column or during sediment recovery. Other possible explanations for the chloride gradient include mineral dehydration reactions at depth, clay membrane ion filtration reactions at depth, and advection of fresher fluid at depth (Kastner et al., 1990).

T12. Interstitial water geochemical data, Hole 1235A, p. 64.

F26. Interstitial water geochemical data, p. 47.

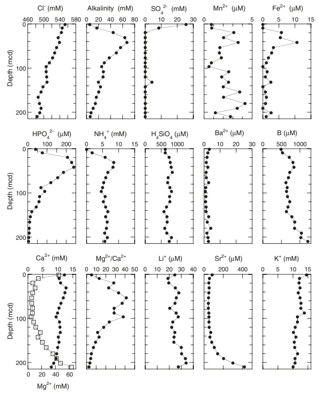

Organic matter diagenesis, driven by microbial oxidation reactions, dominates many of the interstitial water profiles. The relatively low organic carbon contents are apparently counterbalanced by high total sedimentation rates, as at Site 1234, and result in pronounced depth variations in interstitial water chemistry as typically observed in more organic carbon–rich continental margin settings. Sulfate concentration at 1.5 mcd is 25.5 mM, only slightly reduced from typical seawater values of 29 mM, and sulfate concentrations are below the detection limit (~0.6 mM) by 19.6 mcd.

Organic matter decomposition by sulfate reduction and methanogenesis drives large increases in alkalinity, which increases to peak values of >60 mM from 31.1 to 41.7 mcd, then decreases to a minimum of 25 mM at 96.5 mcd. After a slight increase, alkalinity declines to 6 mM at 210.0 mcd. The alkalinity maximum at Site 1235 has peak values ~10% lower than those at Site 1234, and the alkalinity maximum at Site 1235 is deeper and narrower than that at Site 1234. These differences are consistent with less rapid sulfate depletion with depth at Site 1235. Alkalinity declines with increasing depth below the maxima at Sites 1233, 1234, and 1235, with the lowest values seen in the deepest section of Site 1235 (>166 mcd), consistent with the greater degree of authigenic carbonate mineralization at Site 1235 (see **"Lithostratigraphy,"** p. 5).

The reduced forms of the secondary oxidants manganese and iron are not simply related to that of sulfate. Dissolved manganese averages 2 µM, and concentrations at Site 1235 are generally greater than those at Site 1234. The profile has a subsurface peak from 19.6 to 41.7 mcd, reaches minimum values around 100 mcd, and is followed by a secondary maximum at greater depth (Fig. **F26**), although concentrations throughout are not large relative to the blank levels for which they have been corrected. Dissolved iron concentrations reach a peak of 10.7 µM from 41.7 mcd, followed by a steep then more gradual decline to values generally <2 µM deeper than 77 mcd. Iron concentrations are generally higher at Site 1235 than those at Site 1234. Manganese and iron profiles do not show a clear succession of redox zonation with sulfate profiles.

Organic matter decomposition generates increases in phosphate and ammonium in interstitial water. Phosphate concentrations are >200 µM from 19.6 to 41.7 mcd then decline sharply to 62 µM at 108.2 mcd, then to 4 µM at 210.0 mcd. Maximum phosphate values at Site 1235 are higher than those at Site 1234, with a steeper decline with depth, indicating greater uptake in authigenic mineralization reactions.

Ammonium concentrations increase from below the detection limit (0.3 mM) at 1.5 mcd to values >8 mM from 31.1 to 41.7 mcd, decrease to a low of 4.6 mM at 96.5 mcd, and persist at concentrations of 5–7 mM throughout. The ammonium peak at Site 1235 is narrower in depth and lower in peak amplitude than that at Site 1234, consistent with the alkalinity differences between the two sites.

Dissolved silicate concentrations average ~720 µM, with little depth variation, (Fig. **F26**), similar to the profile at Site 1234. The interstitial waters are under saturation with respect to biogenic opal (saturation value >1000 µM). This may reflect the limited amount of biogenic opal available for dissolution or other controls on opal solubility in these sediments. Diatoms are less well preserved at Site 1235 than at Site 1234 (see **"Biostratigraphy,"** p. 9), despite similar silicate concentrations in interstitial waters. Barium concentrations are significantly lower than those at Sites 1233 (peak value = >35 µM) and 1234 (peak value = up to

25 µM), with barium always <4 µM at Site 1235. All three sites experience total sulfate reduction at shallow depth, which should drive barite dissolution and produce dissolved barium in proportion to the sulfate decline. The boron profile in the upper 150 mcd is similar in character to those at Sites 1233 and 1234, with an increase to values >800 µM from 31.1 to 41.7 mcd. The boron peak is lower in concentration and reached deeper at Site 1235 than that at Site 1234. Boron reaches a low of 637 µM at 142.2 mcd then increases steeply to >1200 µM at 210.0 mcd, indicating a source of boron at depth. The contrasts in alkalinity between Sites 1233, 1234, and 1235 profiles appears to be reflected in the boron profiles.

Calcium concentrations decrease sharply from 10.3 mM at 1.5 mcd to 1.7 mM at 19.6 mcd, persist at low values to a minimum of 1.1 mM at 96.5 mcd, and then increase sharply with depth to 14.6 mM (greater than seawater calcium) at 210.0 mcd. Sites 1233 and 1235, both characterized by strong chlorinity decreases with depth, have strong minima in calcium at ~100 mcd. Magnesium concentrations increase to >54 mM from 31.1 to 41.7 mcd, decrease to a minimum of 41.2 mM at 96.5 mcd, increase again, then decrease to 34.3 mM at 210.3 mcd. The very strong decrease in calcium by 19.6 mcd is consistent with authigenic mineralization reactions driven by the alkalinity increase. Increasing magnesium/calcium ratios with the calcium decrease indicate that calcite precipitation is the most likely reaction taking place in shallow sediments. Magnesium/calcium ratios increase to a maximum of 41 at 53.2 mcd, with a secondary maximum of 38 at 96.5 mcd driven by the strong calcium minimum at that depth. This peak in Mg/Ca is not observed at Site 1234. A strong decline in Mg/Ca below this depth, to 2.4 at 210.3 mcd, compares with higher values at the comparable depth range of Site 1234. This may reflect more significant uptake of Mg in authigenic dolomite at this site, where dolomite nodules were found (see **"Lithostratigraphy,"** p. 5).

Lithium profiles are similar at Sites 1233, 1234, and 1235, with a sharp initial decrease followed by a general increase with increasing depth before a decrease in the deepest samples (Fig. **F26**). Strontium concentrations decrease quickly with increasing depth at all three sites, reaching a broad minimum <55 µM at Site 1235 from 19.6 to 119.8 mcd. Strontium concentrations at Site 1235 increase sharply below ~150 mcd, to 420 µM at 210.0 mcd, a feature not seen at Site 1234. The strontium increase in the deepest part of Site 1235, like the calcium and boron increases over a similar depth range, requires a source at depth for these elements, presumably from the diffusive influence of basement alteration reactions. Potassium concentrations generally decrease from 14.6 mM at 1.5 mcd to 10.1 mM at 210.0 mcd (Fig. **F26**).

Sedimentary Inorganic Carbon and Organic Carbon, Nitrogen, and Sulfur Concentrations

Inorganic carbon (IC), total carbon (TC), total nitrogen (TN), and total sulfur (TS) concentrations were determined on sediment samples from Holes 1235A and 1235B (Table **T13**). Organic matter carbon/nitrogen ratios and Rock-Eval pyrolysis were employed to characterize the organic matter.

Calcium carbonate concentrations are low, ranging between 0.3 and 15.5 wt% (average = 2.4 wt%) (Fig. **F27**). In the uppermost 70 mcd, the calcium carbonate concentrations are small. Below this depth, calcium carbonate concentrations are somewhat higher and show larger ampli-

T13. IC, $CaCO_3$, TC, TOC, TN, TOC/TN ratio, TS and TOC/TS ratio, p. 65.

F27. $CaCO_3$, TOC, TN, and TOC/TN vs. depth, p. 48.

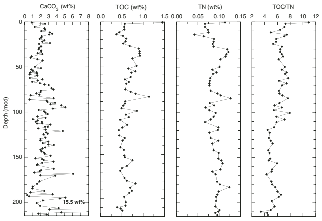

tude variations of 2–5 wt%. The highest calcium carbonate concentration of 15.5 wt% is present between 206.4 and 213.6 mcd. Calcium carbonate originates mainly from calcareous plankton, although diagenetic inorganic carbon is visible in some intervals (see **"Lithostratigraphy,"** p. 5). The low calcium carbonate concentrations and amplitude fluctuations result from high fluvial supply of siliciclastics. The control of calcium carbonate at Site 1235 by dilution rather than productivity and dissolution, is consistent with well-preserved microfossils observed in sediments. Calcium carbonate concentrations at Site 1235 are lower than those at Site 1234, suggesting an even stronger dilution effect at the shallower Site 1235 than at the deeper Site 1234.

TOC concentrations range between 0.4 and 1.5 wt% (average = 0.6 wt%) (Fig. **F27**). The shallowest sample at 0.7 mcd has the highest concentration measured at the site. Below this surface sample, TOC contents remain and small variations throughout the sedimentary record. Two intervals have slightly higher TOC concentrations, between 27.4 and 65.1 mcd and between 78.9 and 84.3 mcd. The TN record contains very similar trends. We infer that the TOC variations are driven by the interplay between siliciclastic dilution and export productivity from the overlying waters. As it was for calcium carbonate, the dilution effect on TOC is more pronounced at the shallower Site 1235 than at the deeper Site 1234. Such a large supply of siliciclastics is not typical for upwelling regions. For example, the coastal upwelling areas of the Namibia and California margins are characterized by upper Pleistocene TOC contents as high as 17 and 7 wt%, respectively (Lyle, Koizumi, Richter, et al., 1997; Berger et al., 1998).

F28. TN vs. TOC and TOC/TN vs. TOC, p. 49.

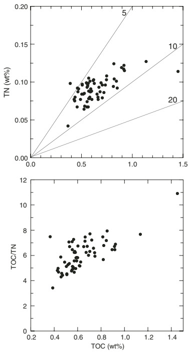

TS concentrations are high throughout the record, varying between 0.3 and 2.1 wt% (Table **T13**), with a long-term tendency for higher contents toward the bottom of the sedimentary record.

TOC/TN ratios typically range between 5 and 10, which indicates a predominantly marine origin of the organic material (Fig. **F28**) (Bordovskiy, 1965; Emerson and Hedges, 1988; Meyers, 1997). Lower TOC/TN ratio are associated with lower TOC concentrations (Fig. **F28**) indicating an increased supply of terrigenous organic matter and/or differential preservation during diagenesis.

Five samples were selected for Rock-Eval measurements. Low T_{max} values indicate that the organic matter is thermally immature (Table **T14**). The relationship between S_2 and TOC concentrations shows that the organic matter is dominantly Type II (Fig. **F29**) (i.e., marine algal organic matter) (Tissot and Welte, 1984; Langford and Blanc-Valleron, 1990), which is consistent with the low TOC/TN ratios at Site 1235.

T14. Rock-Eval pyrolysis analyses, Hole 1235A, p. 68.

Fresh marine plankton has a relatively high lipid content and thus high H/C ratios. Therefore, well-preserved organic matter of marine algal origin yields high hydrogen index (HI) values when subjected to pyrolysis. The HIs measured in these samples are low, ranging from 220 to 289 (Table **T14**). This indicates a significant degradation of organic matter. The correspondence between decreases in both TOC concentrations and HI values (Fig. **F29**) could indicate that preservation of marine organic matter during diagenesis is important in controlling the organic carbon concentrations on the Chile margin.

F29. S_2 vs. TOC and HI vs. TOC, p. 50.

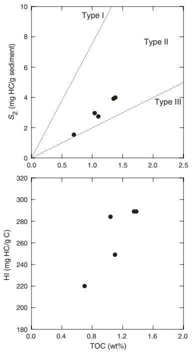

AGE MODEL AND MASS ACCUMULATION RATES

A 215.5-mcd thick (181.3 mbsf) Pleistocene to Holocene hemipelagic sequence was recovered at Site 1235. Calcareous nannofossils indicate a basal age < 0.26 (Zone NN21; see **"Biostratigraphy,"** p. 9). The entire record is of normal polarity and within the Bruhnes Chron (1n; see **"Paleomagnetism,"** p. 11). A conservative estimate of the average sedimentation rate is therefore ~696 m/m.y. A detailed age-depth model was not created shipboard, as datums are not abundant enough at this site of extremely high sedimentation rates.

REFERENCES

Abrantes, F., 1988. Diatom assemblages as upwelling indicators in surface sediments off Portugal. *Mar. Geol.,* 85:15–39.

Abrantes, F., and Moita, T., 1999. Water column and recent sediment data on diatoms and coccolithophorids, off Portugal, confirm sediment record as a memory of upwelling events. *Oceanol. Acta*, 22:319–336.

Ahumada, R., 1989. Produccion y destino de la masa fitplantonica en sistema de bahias en Chile central: una hipotesis. *Biol. Pesq.,* 18:53–66

Berger, W.H., Wefer, G., Richter, C., Lange, C.B., Giraudeau, J., Hermelin, O., and Shipboard Scientific Party, 1998. The Angola-Benguela upwelling system: paleoceanographic synthesis of shipboard results from Leg 175. *In* Wefer, G., Berger, W.H., and Richter, C., et al., *Proc. ODP, Init. Repts.,* 175: College Station, TX (Ocean Drilling Program), 505–531.

Berggren, W.A., Kent, D.V., Swisher, C.C., III, and Aubry, M.-P., 1995. A revised Cenozoic geochronology and chronostratigraphy. *In* Berggren, W.A., Kent, D.V., Aubry, M.-P., and Hardenbol, J. (Eds.), *Geochronology, Time Scales and Global Stratigraphic Correlation*. Spec. Publ.—SEPM, 54:129–212.

Bordovskiy, O.K., 1965. Accumulation and transformation of organic substances in marine sediment, 2. Sources of organic matter in marine basins. *Mar. Geol.,* 3:5–31.

Brandhorst, W., 1971. Condiciones oceanográficas extivales frente a la costa de Chile. *Revista Biologica Marina (Valparaiso),* 14:45–84.

Claypool, G.E., and Kvenvolden, K.A., 1983. Methane and other hydrocarbon gases in marine sediment. *Annu. Rev. Earth Planet. Sci.,* 11:299–327.

Deaton, B.C., and Balsam, W.L., 1991. Visible spectroscopy: a rapid method for determining hematite and goethite concentrations in geological materials. *J. Sediment. Petrol.,* 61:628–632.

Dettinger, M.D., Battisti, D.S., Garreaud, R.D., McCabe, G.J., Jr., and Blitz, C.M., 2001. Interhemispheric effects of interannual and decadal ENSO-like climate variations on the Americas. *In* Markgraf, V. (Ed.), *Interhemispheric Climate Linkages:* San Diego (Academic Press), 1–16.

Emerson, S., and Hedges, J.I., 1988. Processes controlling the organic carbon content of open ocean sediments. *Paleoceanography,* 3:621–634.

Fonseca, T.R., 1989. An overview of the poleward undercurrent and upwelling along the Chilean coast. *In* Neshyba, S.J., Mooers, C.N.K., Smith, R.L., and Barber. R.T. (Eds.), *Poleward Flows along Eastern Ocean Boundaries:* New York (Springer), 203–228.

Giosan, L., 2001. The use of sediment color in paleoceanography: Pliocene–Pleistocene sedimentation in the western North Atlantic [Ph.D. dissert.]. State Univ. of New York, Stony Brook.

Hebbeln, D., Marchant, M., and Wefer, G., 2000. Seasonal variations of the particle flux in the Peru Chile Current at 30°S under “normal” and El Niño conditions. *Deep-Sea Res. II,* 47:2101–2128.

Kastner, M., Elderfield, H., Martin, J.B., Suess, E., Kvenvolden, K.A., and Garrison, R.E., 1990. Diagenesis and interstitial water chemistry at the Peruvian continental margin—major constituents and strontium isotopes. *In* Suess, E., von Huene, R., et al., *Proc. ODP, Sci. Results,* 112: College Station, TX (Ocean Drilling Program), 413–440.

Lamy, F., Hebbeln, D., and Wefer, G., 1998. Terrigenous sediment supply along the Chilean continental margin: modern regional patterns of texture and composition. *Geol. Rundsch.,* 87:477–494.

Lamy, F., Rühlemann, C., Hebbeln, D., and Wefer, G., 2002. High- and low-latitude control on the position of the southern Peru-Chile current during the Holocene. *Paleoceanography,* 17:10.1029/2001PA000727.

Langford, F.F., and Blanc-Valleron, M.M., 1990. Interpreting Rock-Eval pyrolysis data using graphs of pyrolizable hydrocarbons vs. total organic carbon. *AAPG Bull.,* 74:799–804.

Lyle, M., 1983. The brown-green color transition in marine sediments: a marker of the Fe(III)–Fe(II) redox boundary. *Limnol. Oceanogr.,* 28:1026–1033.

Lyle, M., Koizumi, I., Richter, C., et al., 1997. *Proc. ODP, Init. Repts.,* 167: College Station, TX (Ocean Drilling Program).

Martini, E., 1971. Standard Tertiary and Quaternary calcareous nannoplankton zonation. *In* Farinacci, A. (Ed.), *Proc. 2nd Int. Conf. Planktonic Microfossils Roma:* Rome (Ed. Tecnosci.), 2:739–785.

Meyers, P.A., 1997. Organic geochemical proxies of paleoceanographic, paleolimnologic, and paleoclimatic processes. *Org. Geochem.,* 27:213–250.

Mix, A.C., Pisias, N.G., Bloomer, S.F., and Mayer, L.A., 1998. *Southeast Pacific Paleoceanographic Transects, Site Survey Data Package 3: 3.5 kHz Data, Genesis Leg III, R/V* Roger Revelle, *Feb.–Apr. 1997:* Corvallis (Oregon State Univ.).

Ocean Climate Laboratory, 1999. *World Ocean Atlas 1998 (WOA98)* [CD-ROM]. Available from: National Climatic Data Center, Asheville NC 28801-5001, USA.

Schrader, H., and Sorknes, R., 1990. Spatial and temporal variation of Peruvian coastal upwelling during the latest Quaternary. *In* Suess, E., von Huene, R., et al., *Proc. ODP, Sci. Results,* 112: College Station, TX (Ocean Drilling Program), 391–406.

Schuette, G., 1980. Recent marine diatom taphocoenoses off Peru and off southwest Africa: reflection of coastal upwelling [Ph.D. dissert.]. Oregon State Univ., Corvallis.

Silva, A.J., Hollister, C.D., Laine, E.P., and Beverly, B., 1976. Geotechnical properties of the Northern Bermuda Rise. *Mar. Geotechnol.,* 1:195–232.

Strub, P.T., Mesias, J.M., Montecino, V., Rutllant, J., and Salinas, S., 1998. Coastal ocean circulation off western South America. *In* Robinson, A.R., and Brink, K.H. (Eds.), *The Sea* (Vol. 11): *Coastal Oceans:* New York (Wiley), 273–313.

Suess, E., von Huene, R., et al., 1988. *Proc. ODP, Init. Repts.,* 112: College Station, TX (Ocean Drilling Program).

Thomson, J., Higgs, N.C., and Colley, S., 1996. Diagenetic redistribution of redox-sensitive elements in northeast Atlantic glacial-interglacial transition sediments. *Earth Planet. Sci. Lett.,* 139: 366–377.

Tissot, B.P., and Welte, D.H., 1984. *Petroleum Formation and Occurrence* (2nd ed.): Heidelberg (Springer-Verlag).

Wiedicke-Hombach, M., and Shipboard Scientific Party, 2002. *Cruise Report* Sonne *SO 161/5 (Subduction Processes of Chile)-Geology-Geochemistry-Heatflow.* Archive Number 11241/02, March 2002.

Figure F1. Three-dimensional bathymetry image of the upper continental margin and locations of Sites 1234 and 1235, based on Parasound data (SO161/5, *Sonne;* Wiedicke-Hombach et al., 2002).

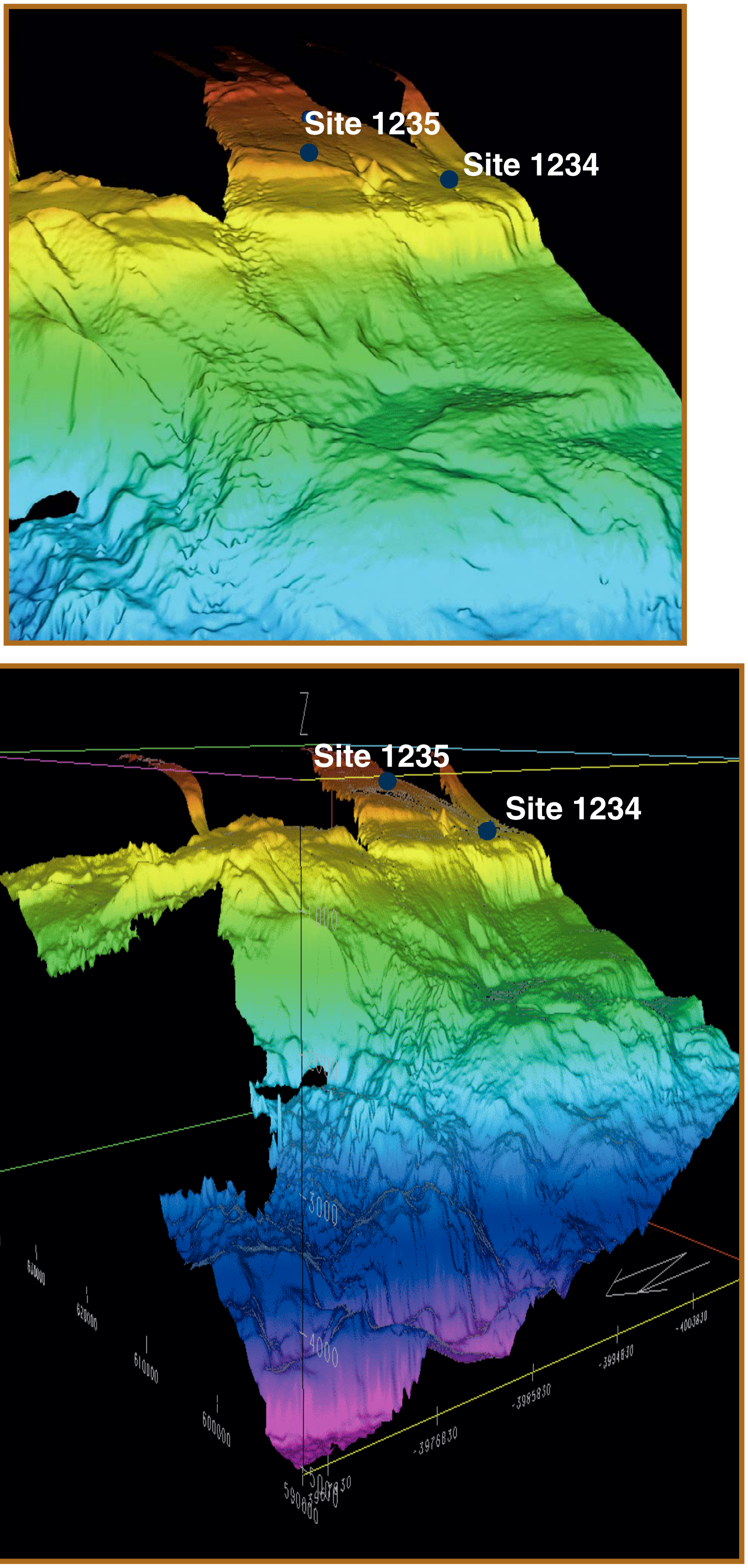

Figure F2. Seismic profile at Site 1235 (line 970313, *Revelle,* 80-in^3 water gun at 30–400 Hz).

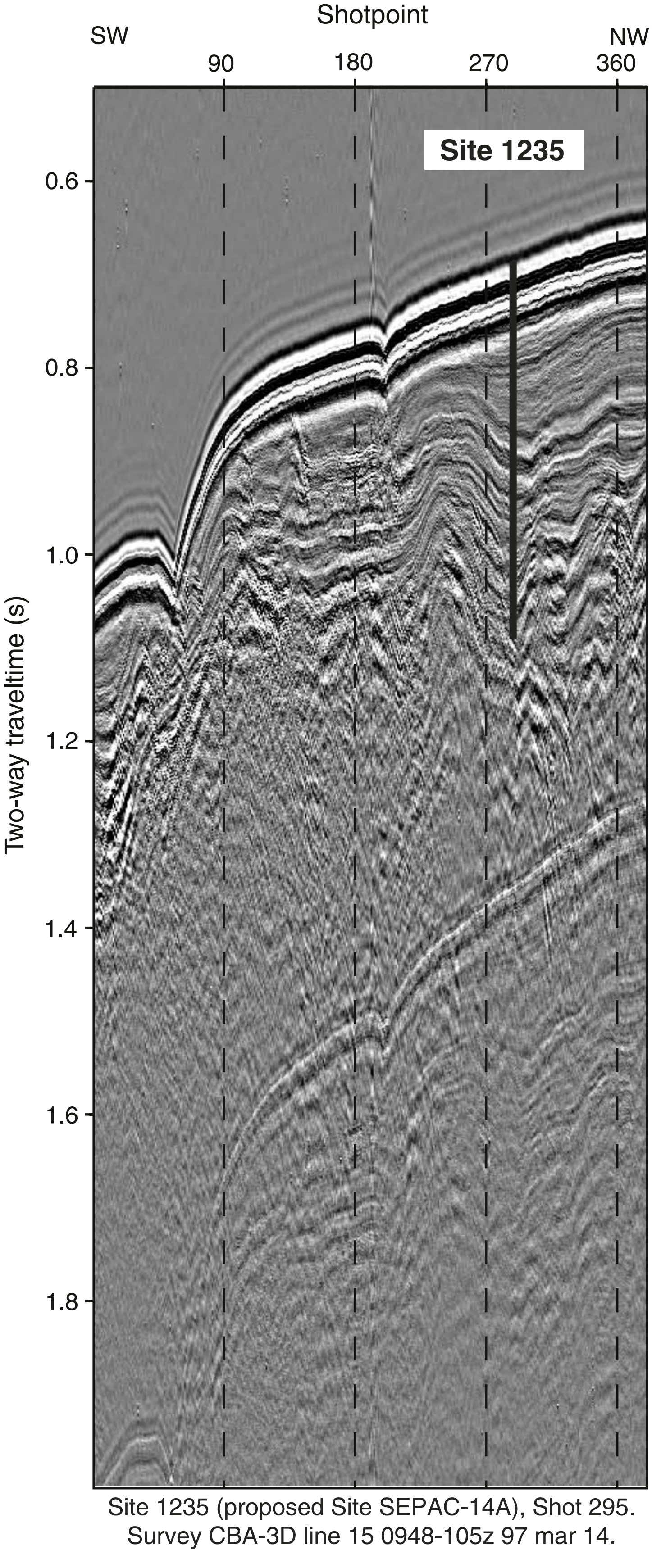

Figure F3. Locations of Sites 1232–1235 and oceanographic features off southern and central Chile (ACC = Antarctic Circumpolar Current, PCC = Peru-Chile Current, PCCC = Peru-Chile Countercurrent, CC = Chile Coastal Current, CFW = Chilean Fjord Water) after Strub et al. (1998) and Lamy et al. (2002). **A.** Modern mean annual sea-surface temperatures (SSTs) (contours are in degrees Celsius, after Ocean Climate Laboratory, 1999; dashed isotherms are extrapolated). **B.** Modern sea-surface salinities (SSSs) measured during the *Marchile* cruise in February to March 1960 (Brandhorst, 1971).

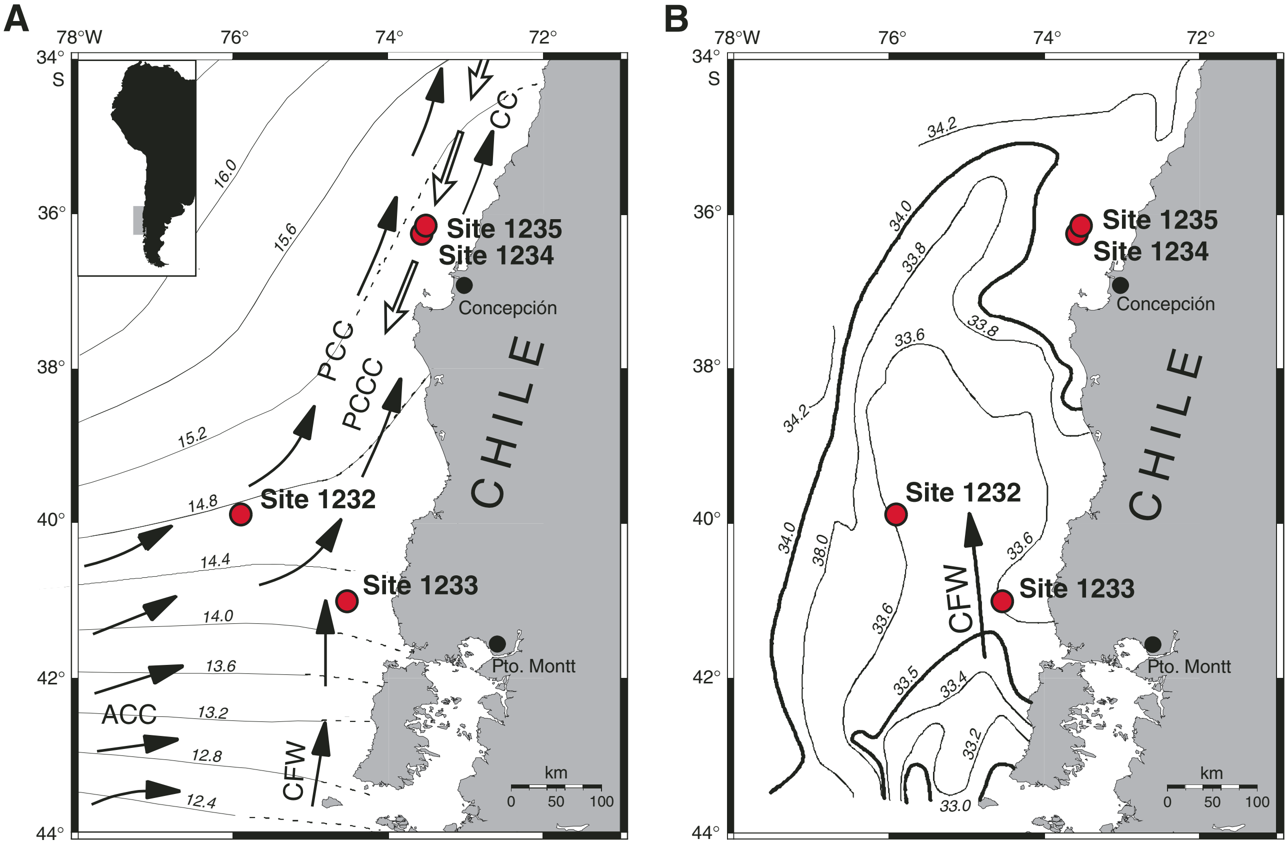

Figure F4. North-south cross section of water masses, characterized by dissolved oxygen concentrations in the southeast Pacific (Ocean Climate Laboratory, 1999). Southward-spreading middepth waters (PCW = Pacific Central Water) are characterized by relatively low oxygen and salinity and high nutrients. Northward-spreading Antarctic Intermediate Water (AAIW), above 1 km depth, is high in oxygen but is low in both salinity and nutrients. The Gunther Undercurrent (GUC) flows southward between 100 and 400 m water depth and is characterized by relatively low oxygen, high nutrients, and high salinity. Vertical bars indicate the water depth range of Sites 1233, 1234, and 1235 relative to the last glacial sea level lowering of ~130 m.

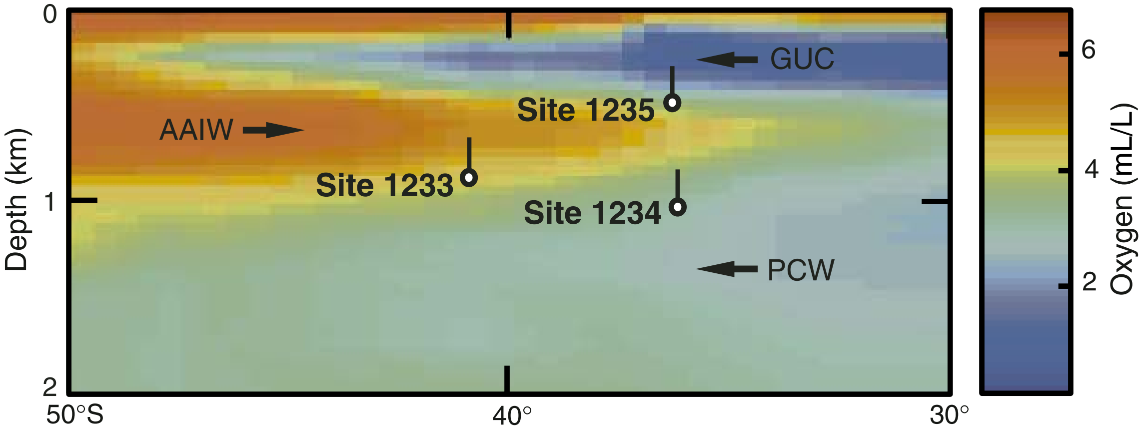

Figure F5. Magnetic susceptibility (MST-MS) vs. mcd for Holes 1235A through 1235C. Gray boxes indicate the portions of cores that are in the splice. Pink boxes indicate intervals within the splice of poor correlation between holes. **A.** 0–40 mcd. **B.** 30–70 mcd. **C.** 60–100 mcd. (Continued on next two pages.)

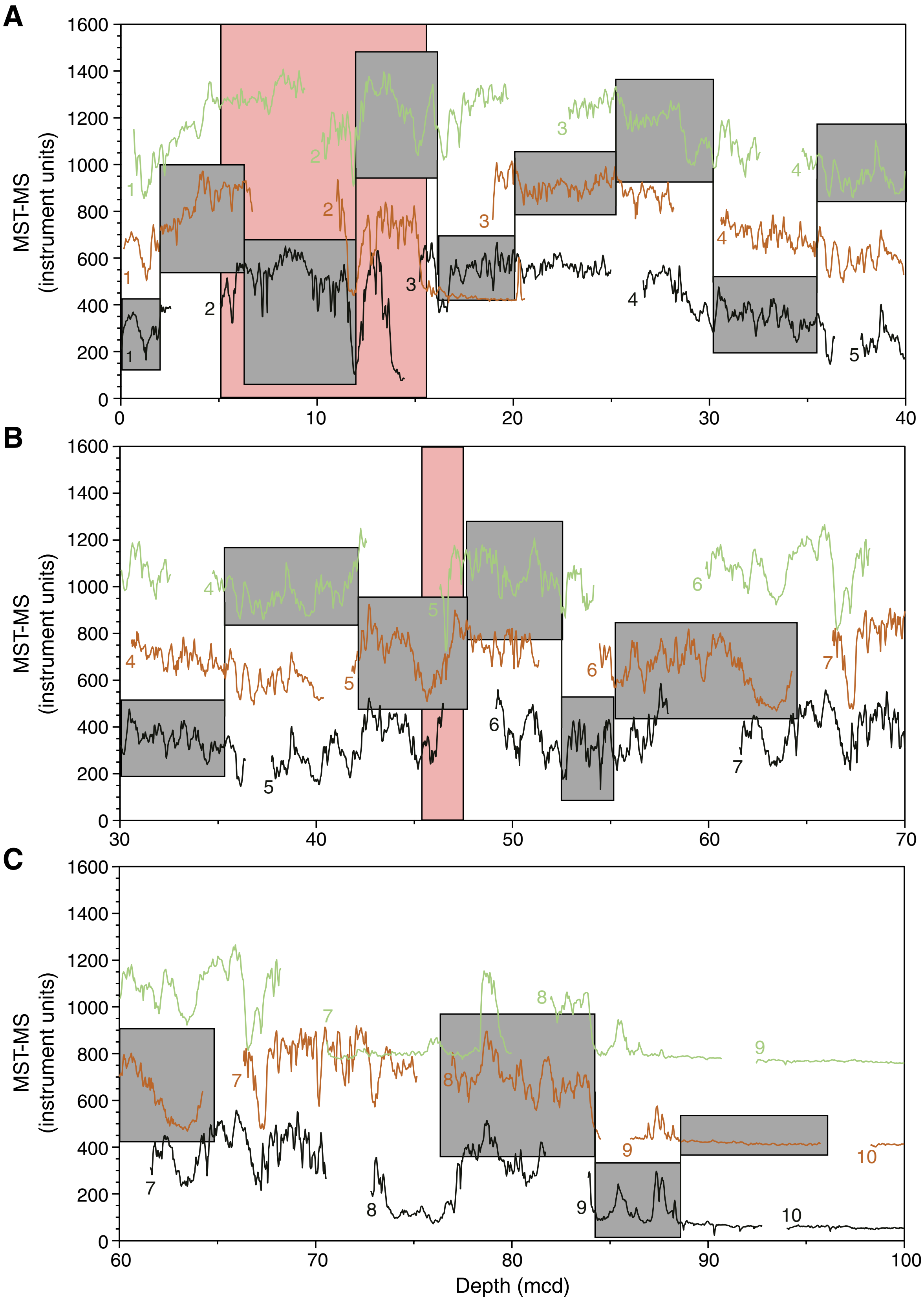

Figure F5 (continued). D. 90–130 mcd. **E.** 120–160 mcd. **F.** 150–190 mcd.

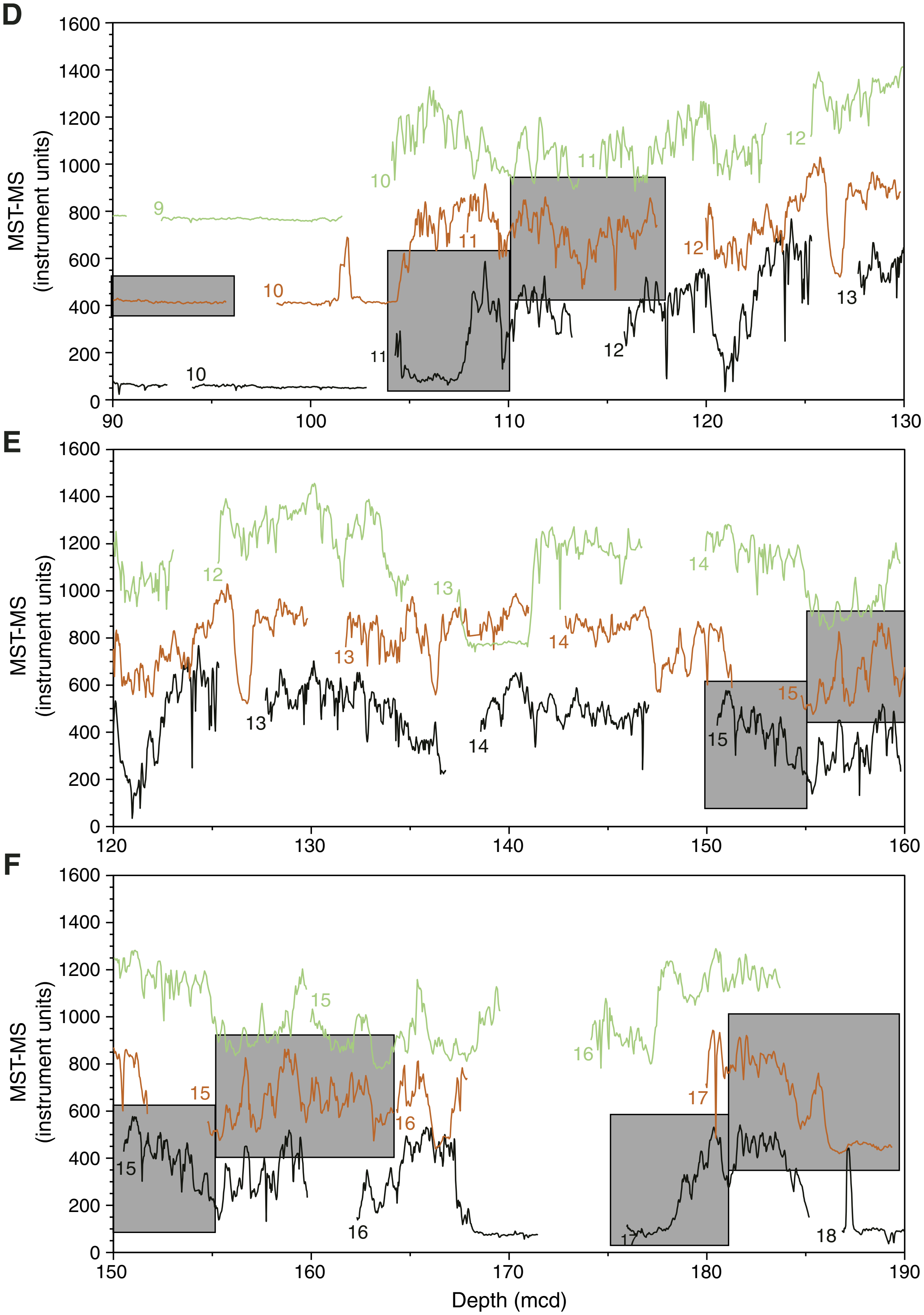

Figure F5 (continued). **G.** 180–220 mcd.

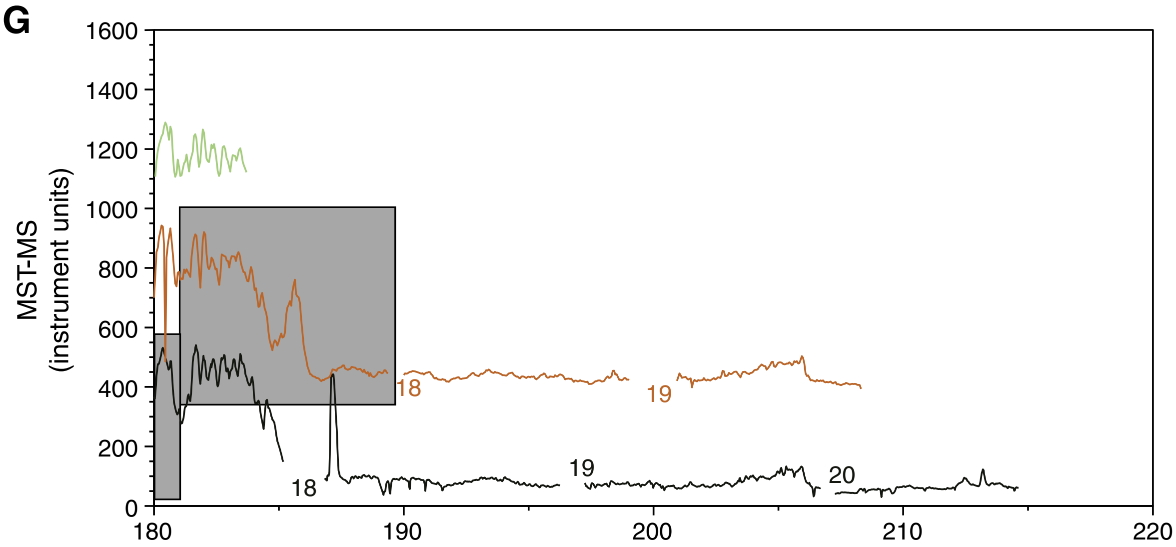

Figure F6. Smoothed (9-point Gaussian) spliced records of natural gamma radiation (NGR), gamma ray attenuation (GRA) bulk density, and magnetic susceptibility (MST-MS) for Site 1235.

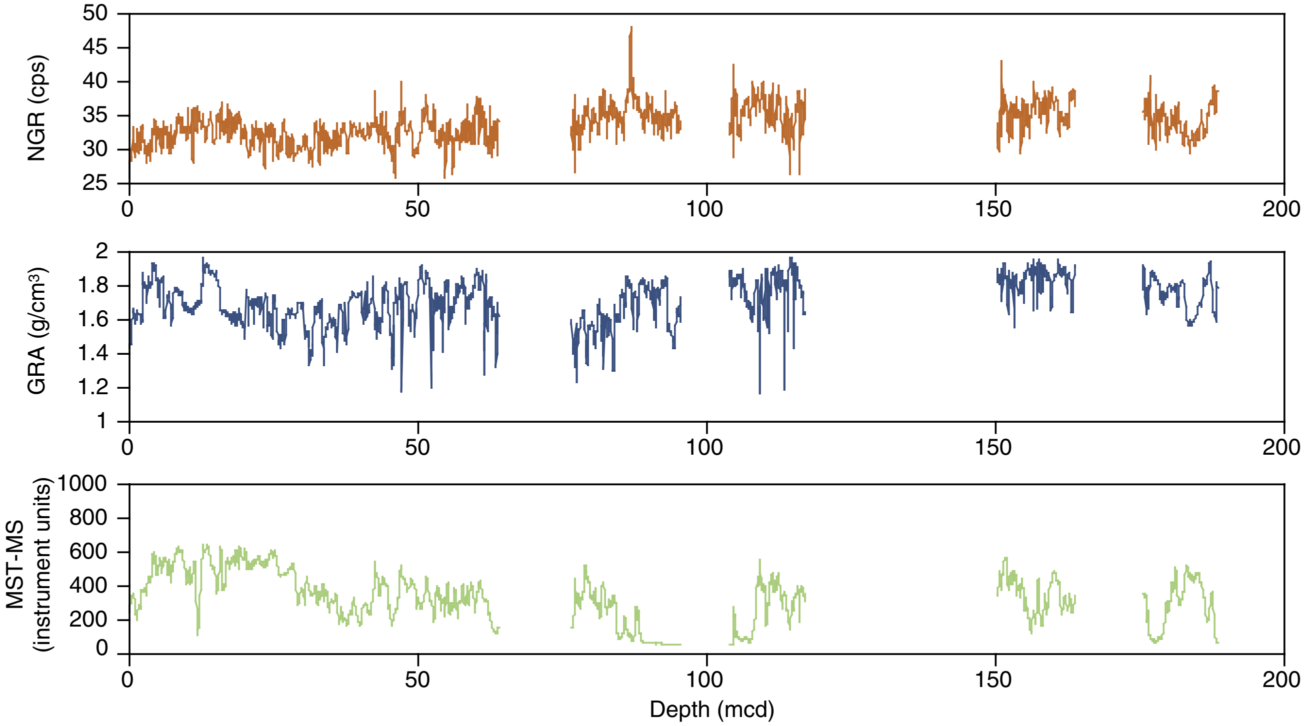

Figure F7. A comparison of the drillers depth (mbsf) and meters composite depth (mcd) scales in Holes 1235A through 1235C. On average, mcd is 20% greater than mbsf. The 1:1 (mbsf:mcd) line is also shown for comparison.

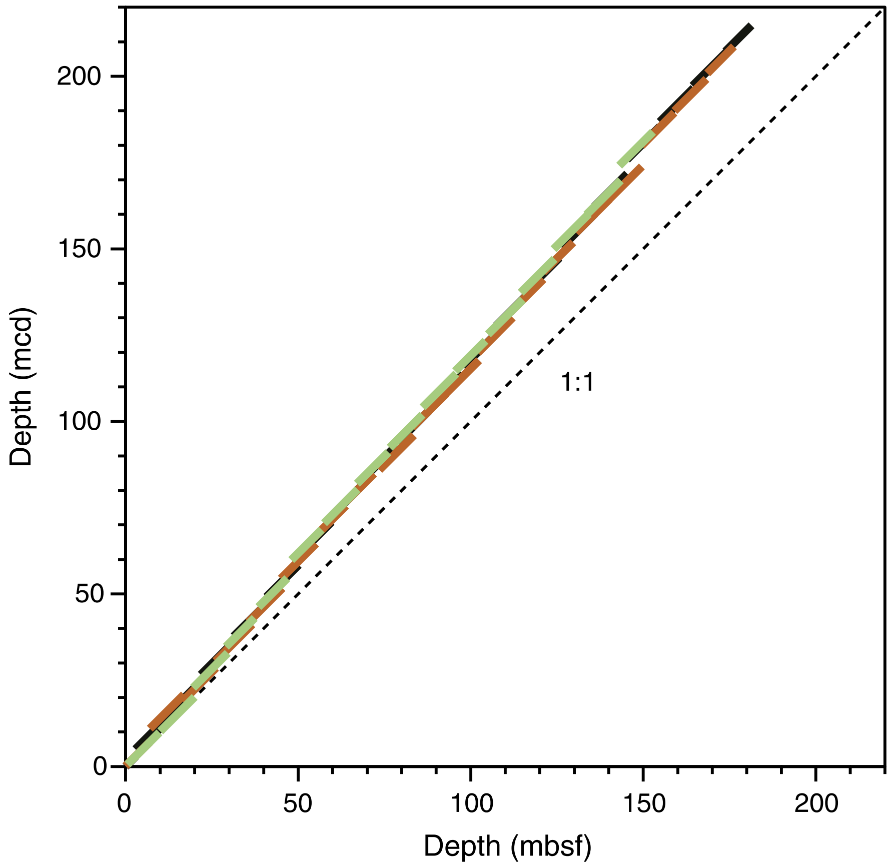

Figure F8. Core recovery, lithostratigraphy, age, magnetic susceptibility, gamma ray attenuation (GRA) bulk density, natural gamma radiation, and color reflectance (chroma a* and b*) of recovered sediments from Site 1235. Lighter lines show the original data, and the dark lines are 50-point smoothing averages of the original data.

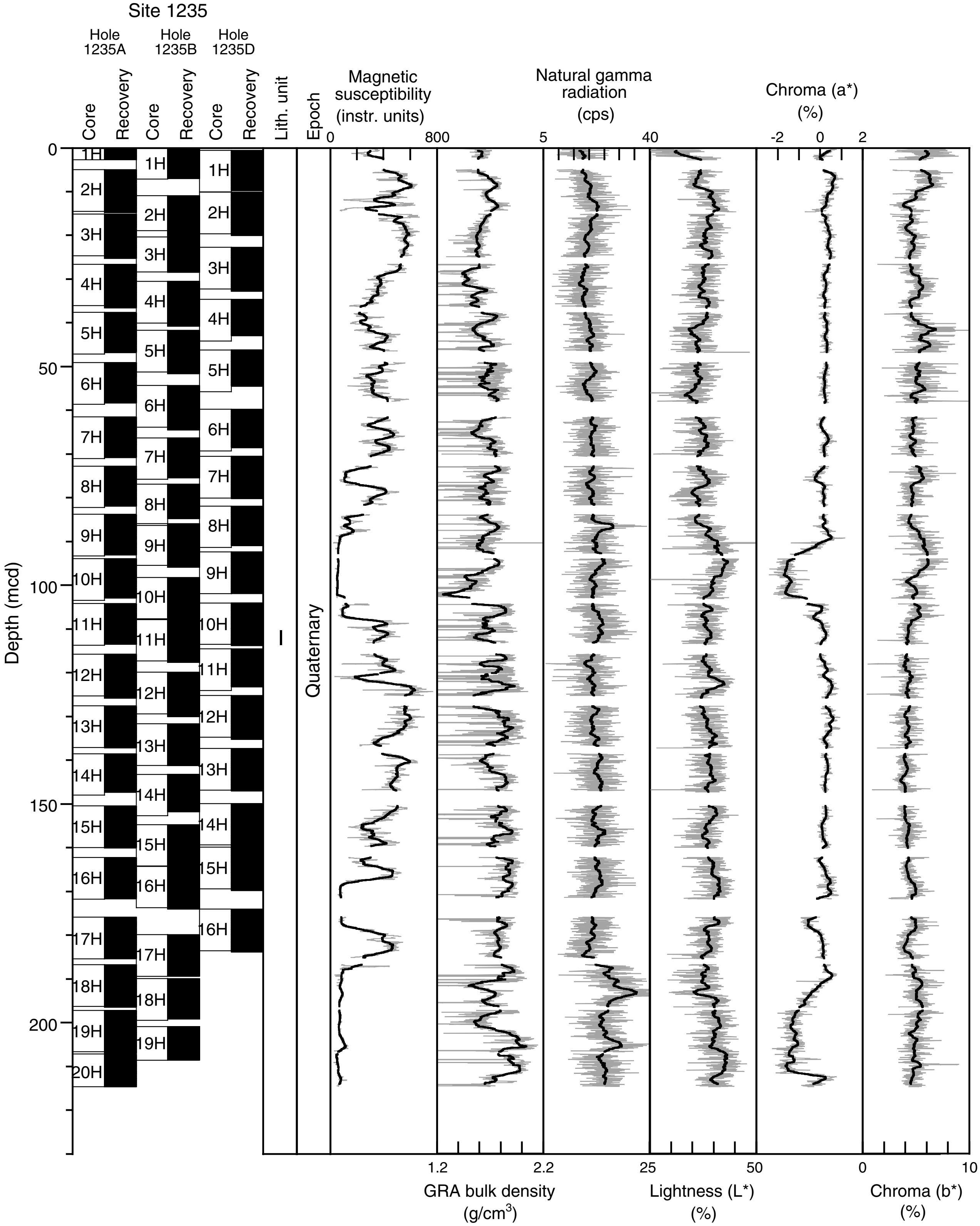

Figure F9. Major siliciclastic, biogenic, and authigenic components observed in Hole 1235A smear slides. The shaded bars indicate depth of carbonate nodules. Biogenetic carbonate = nannofossils + foraminifers + carbonate bioclasts. Biogenic silica = diatoms + radiolarians + sponge spicules + silicollagellates.

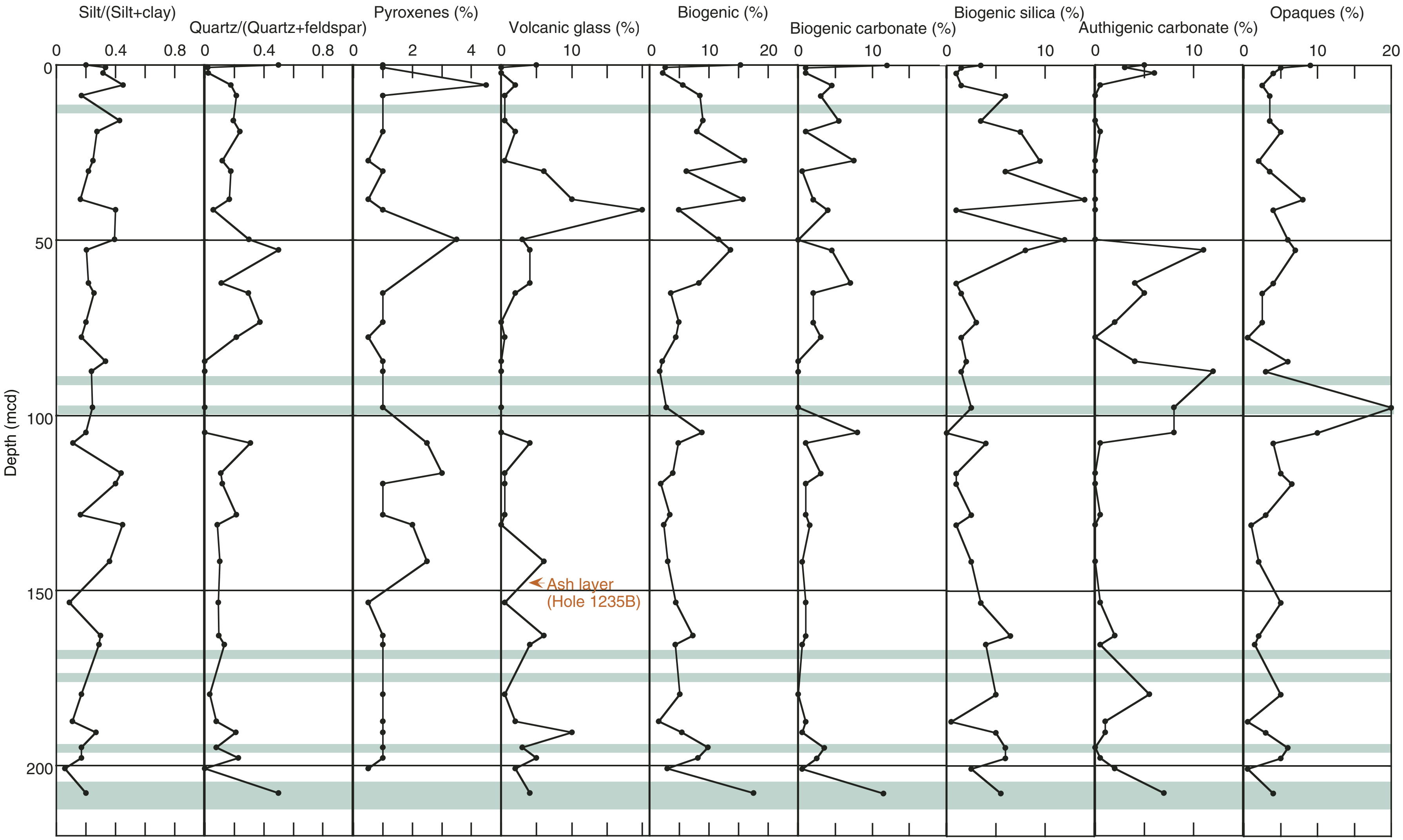

Figure F10. **A.** Close-up photograph showing authigenic carbonate nodule from interval 202-1235A-9H-5, 64–77 cm. **B.** Diffractogram of the X-ray diffraction (XRD) measurement made on a sample taken from one of the nodules (interval 202-1235B-2H-6, 4–5 cm). The major peaks correspond to dolomite.

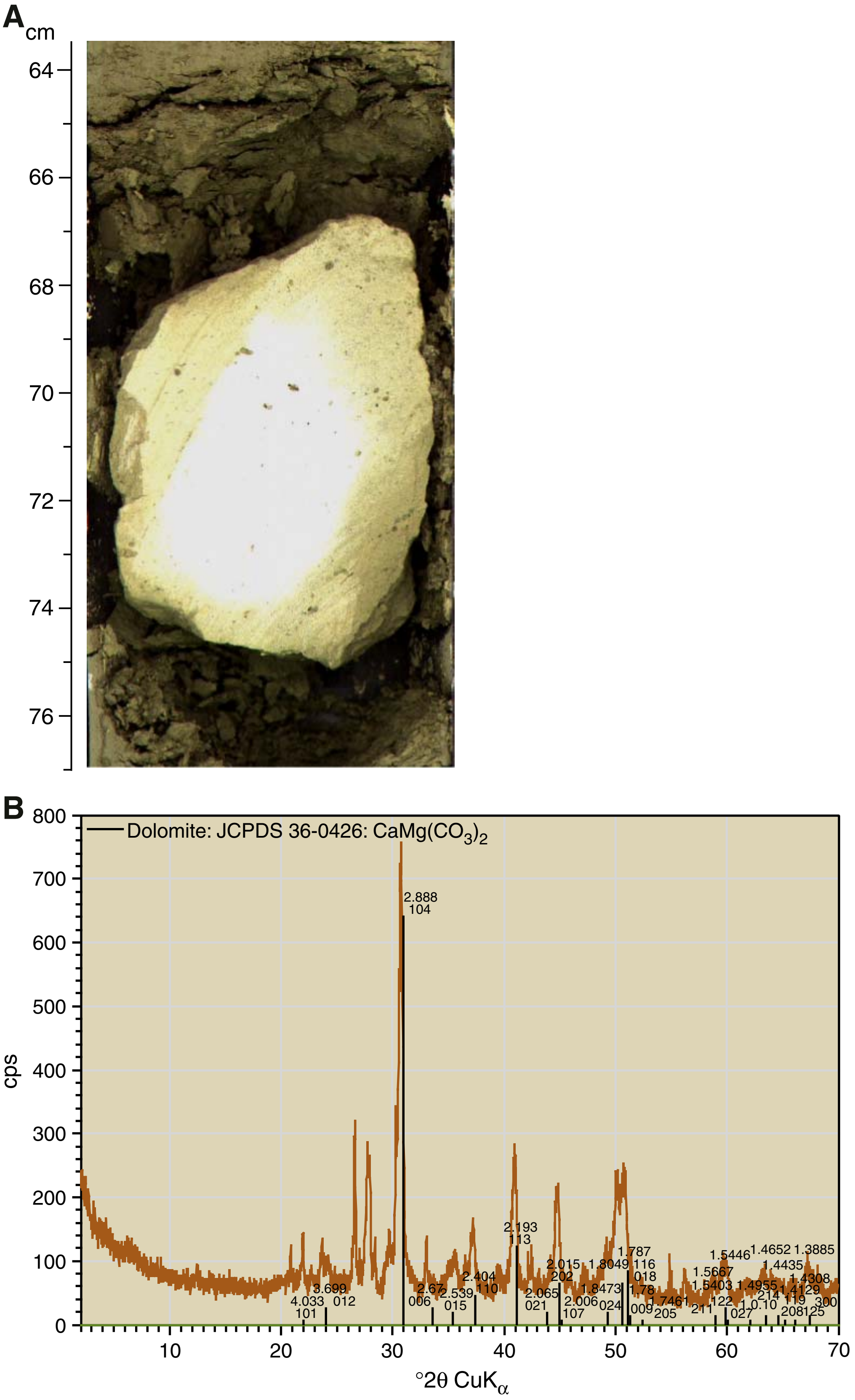

Figure F11. Downhole records of magnetic susceptibility and chroma (a*) for Site 1235. Green bars = the location of the greenish intervals in each of the holes, yellow bars = the position of the associated bioturbated intervals. Green diamonds = the depth of the carbonate nodules.

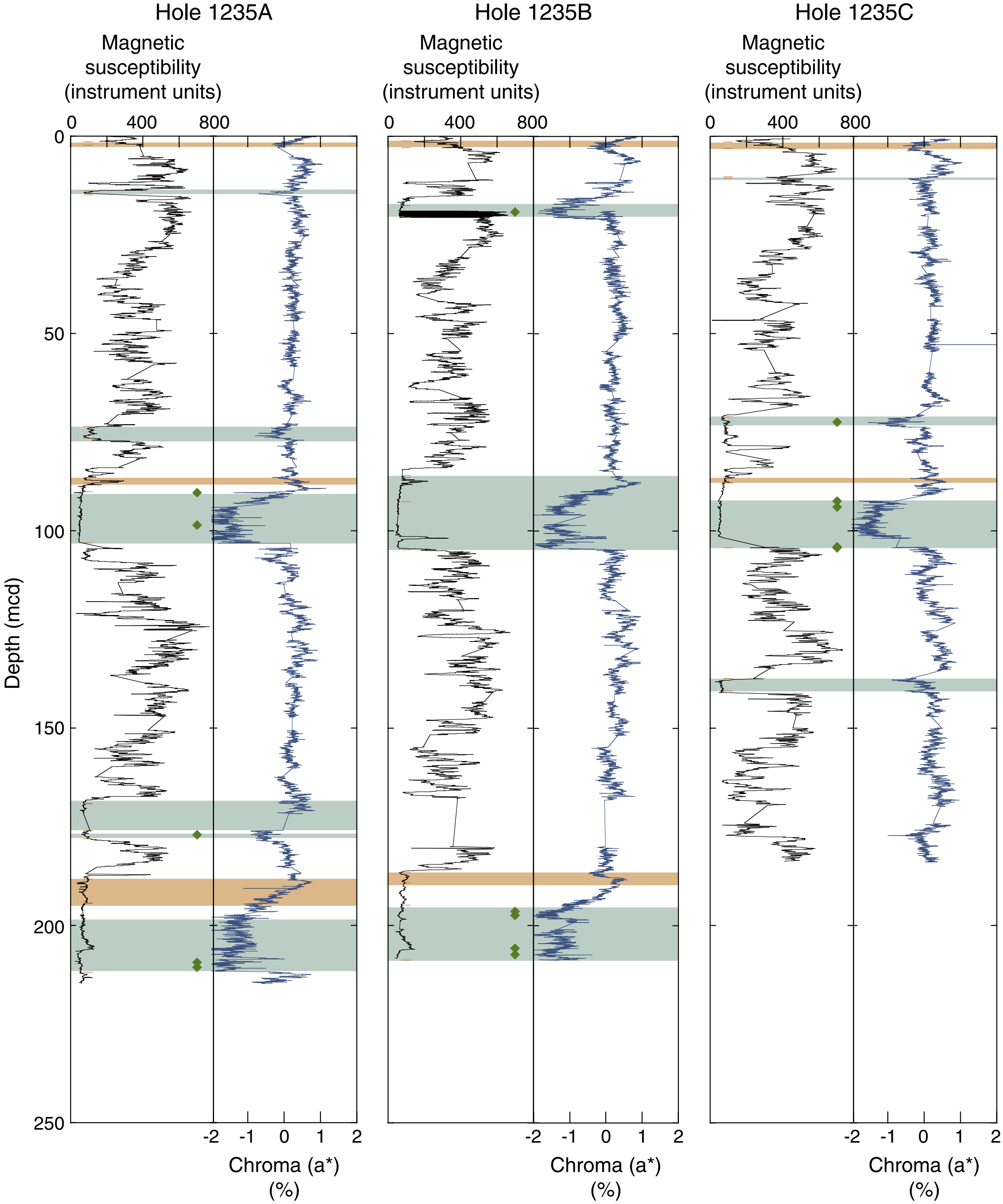

Figure F12. Close-up photograph of a representative color transition and bioturbated sequence (interval 202-1235A-9H-2, 109–136 cm).

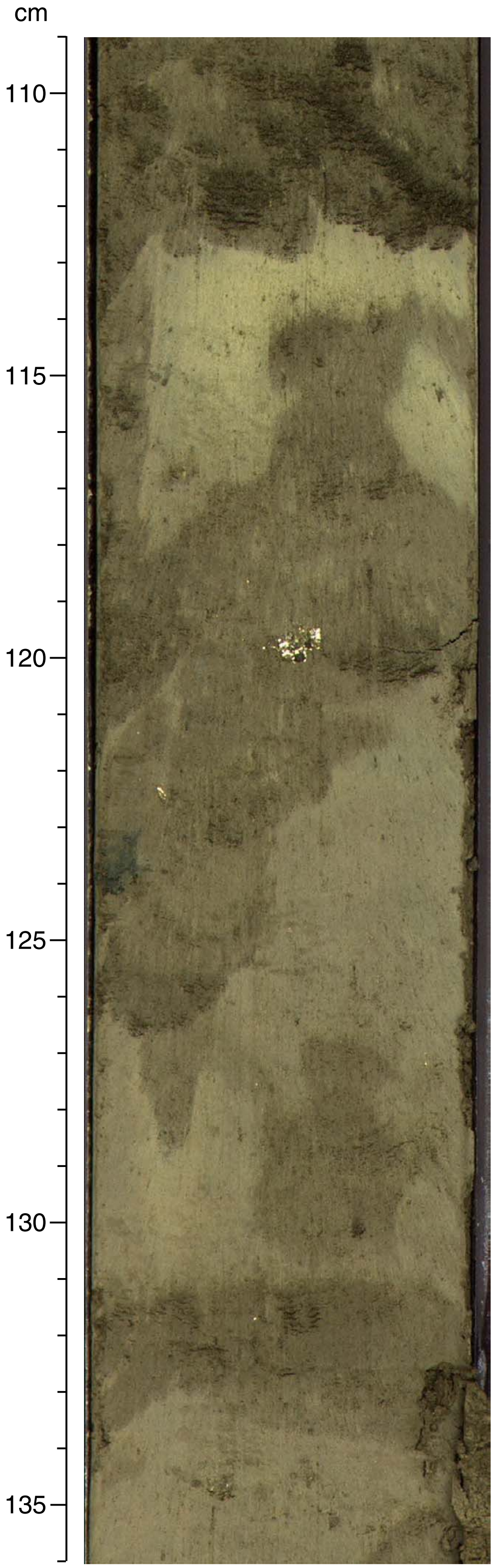

Figure F13. Ash layer (interval 202-1235B-14H-5, 121–126 cm).

Figure F14. Lithology, bulk density, grain density, and porosity. MAD = moisture and density.

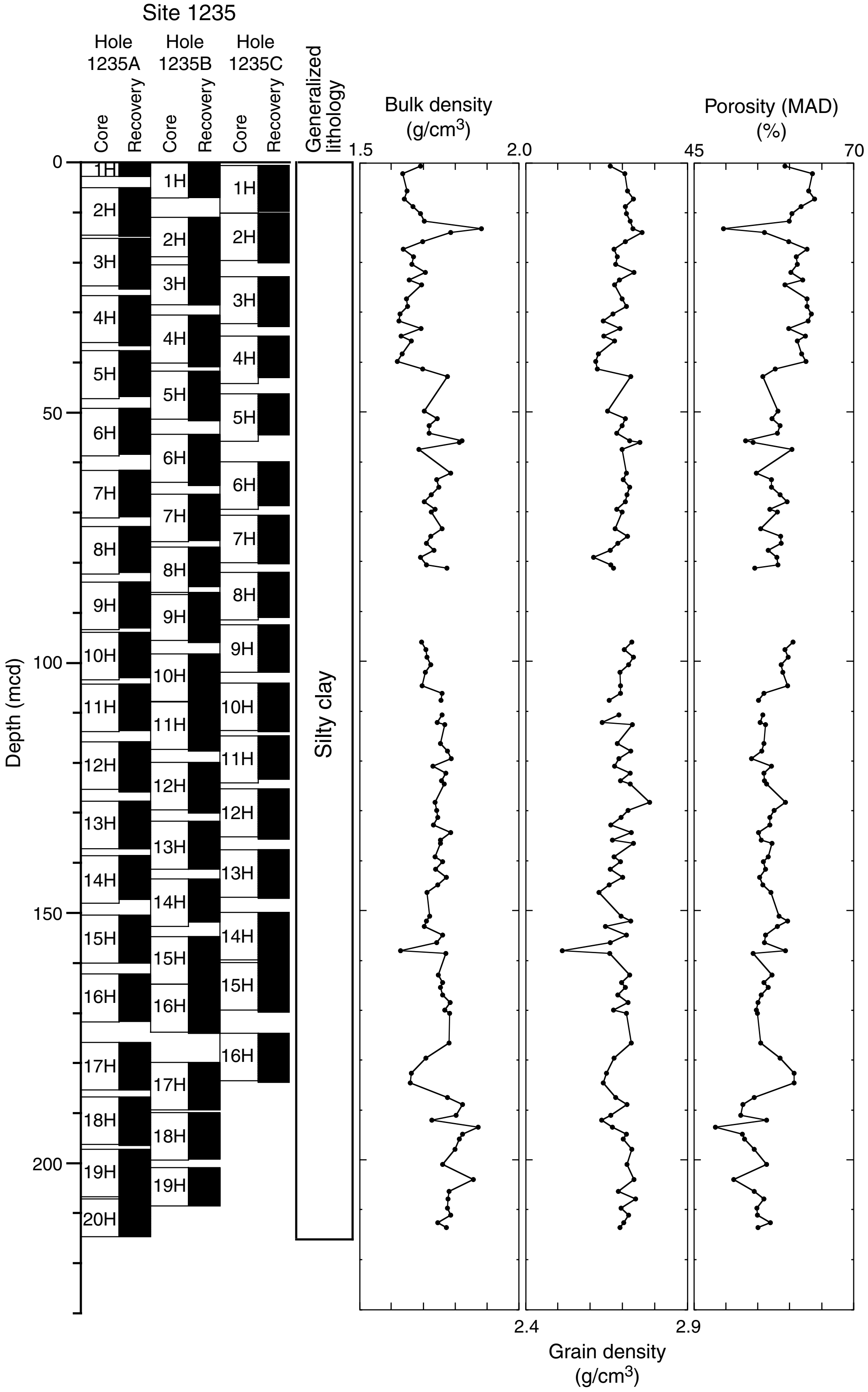

Figure F15. A. Moisture and density (MAD) (circles) and gamma ray attenuation (GRA) (gray line) bulk densities. The thick line represents the smoothed GRA bulk density. **B.** Linear regression between the MAD and GRA bulk density (BD) at MAD measurement locations.

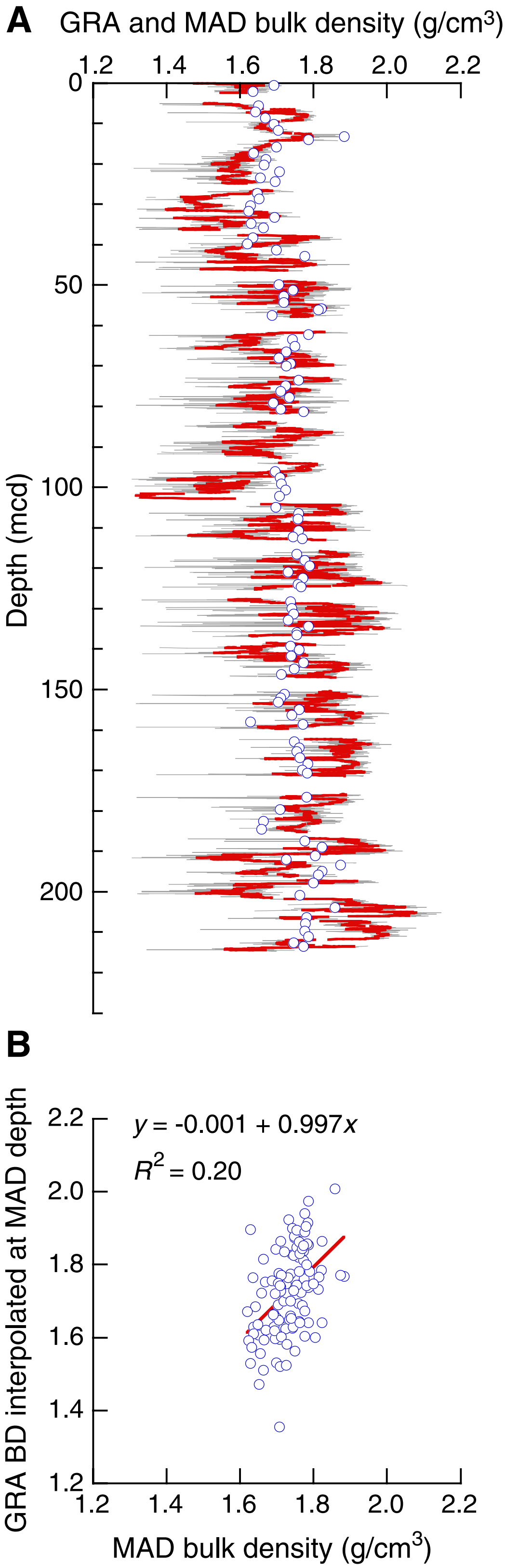

Figure F16. Color measurements for Site 1235 (spliced, 0–214.85 mcd) plotted in the a*-b* color plane.

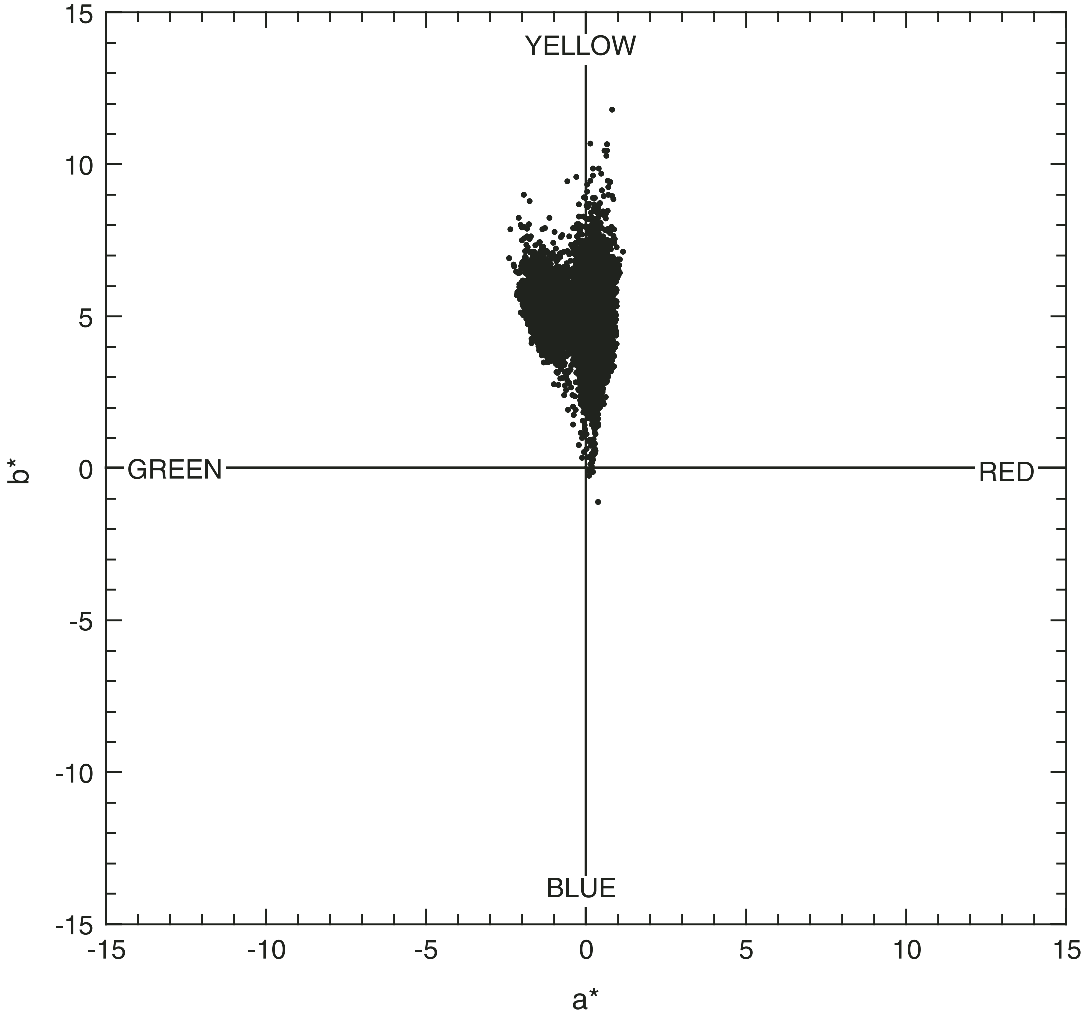

Figure F17. Examples of first derivatives of reflectance spectra in (**A**) green sediments from a region of strong reductive diagenesis (Section 202-1235-A-20H-5, 100 cm) and (**B**) brownish sediments overlaying the green sediments (Section 202-1235-A-18H-2, 70 cm). The presence of hematite and goethite is inferred from characteristic first-derivative peaks (Deaton and Balsam, 1991).

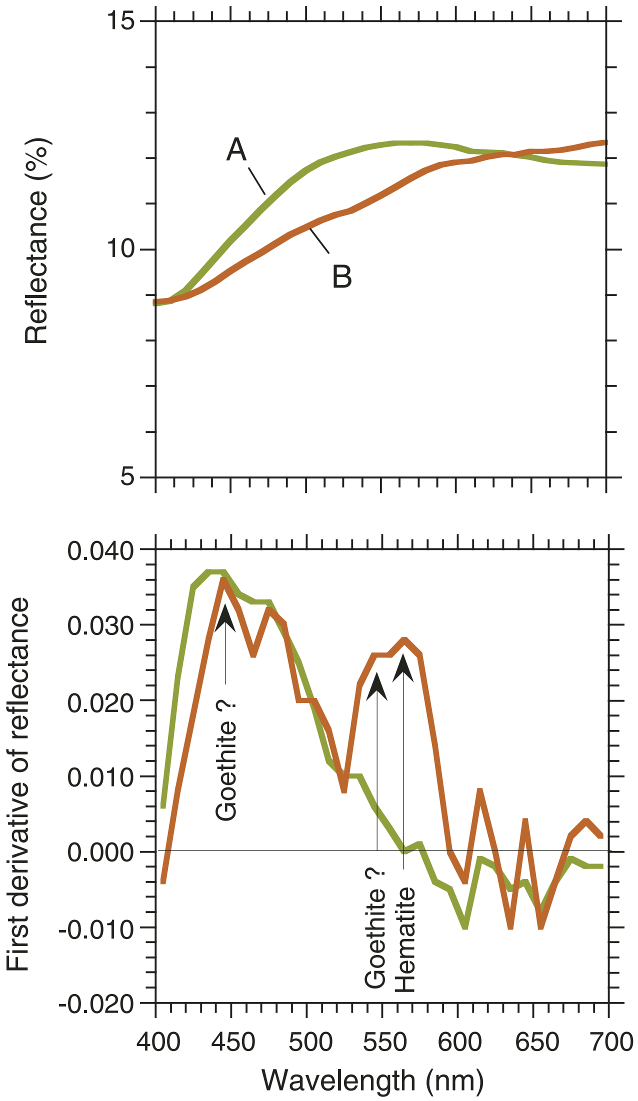

Figure F18. Core recovery, calcareous nannofossil and planktonic foraminifer abundance, benthic foraminifer percentage of total foraminifers, and diatom abundance in Hole 1235A (smoothed lines). B = barren, R = rare, F = few, C = common, A = abundant, VA = very abundant.

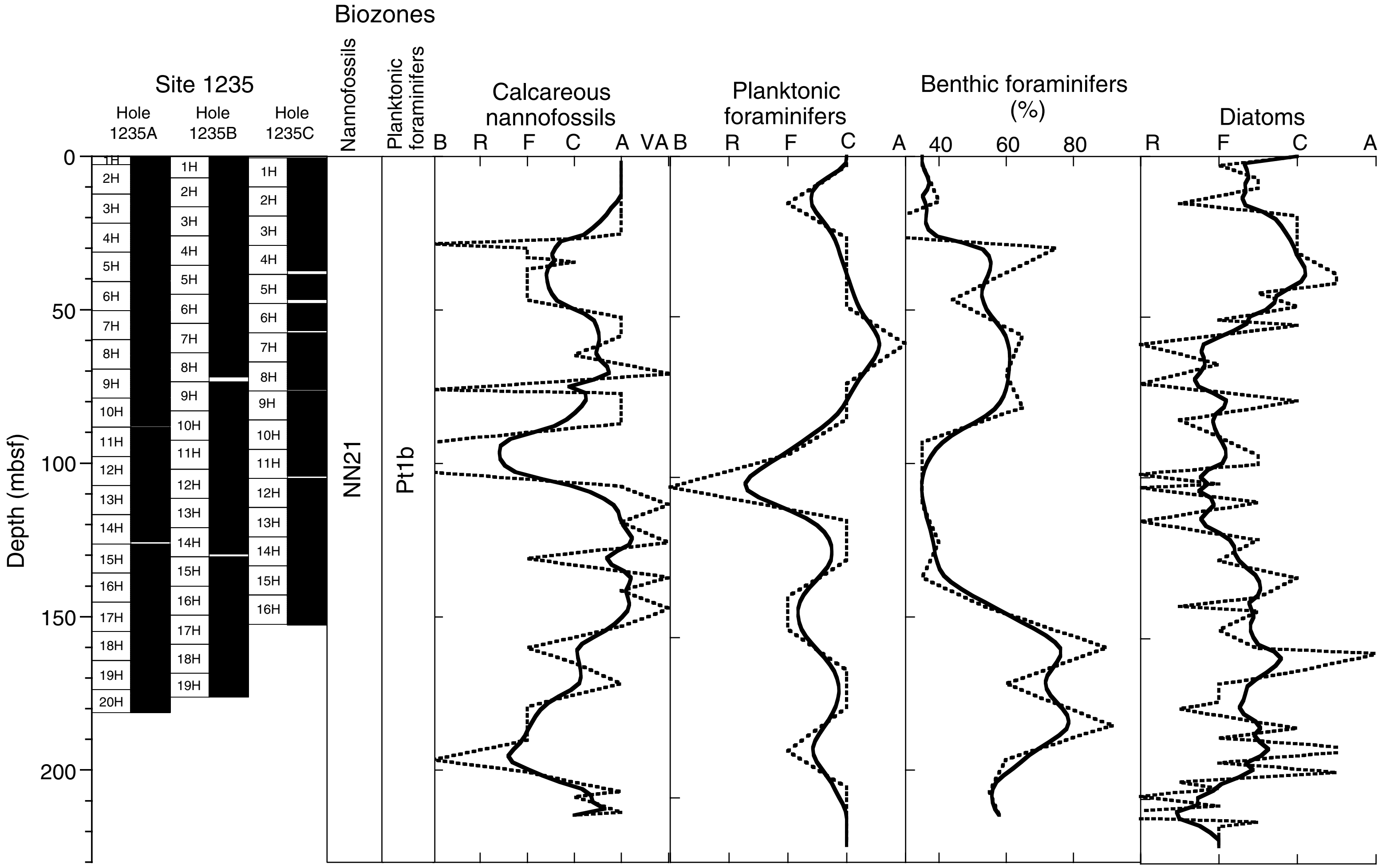

Figure F19. Variations in percent of selected benthic foraminifers (*Bolivina, Bulimina, Uvigerina,* and *Nonionella*) in Hole 1235A (smoothed lines).

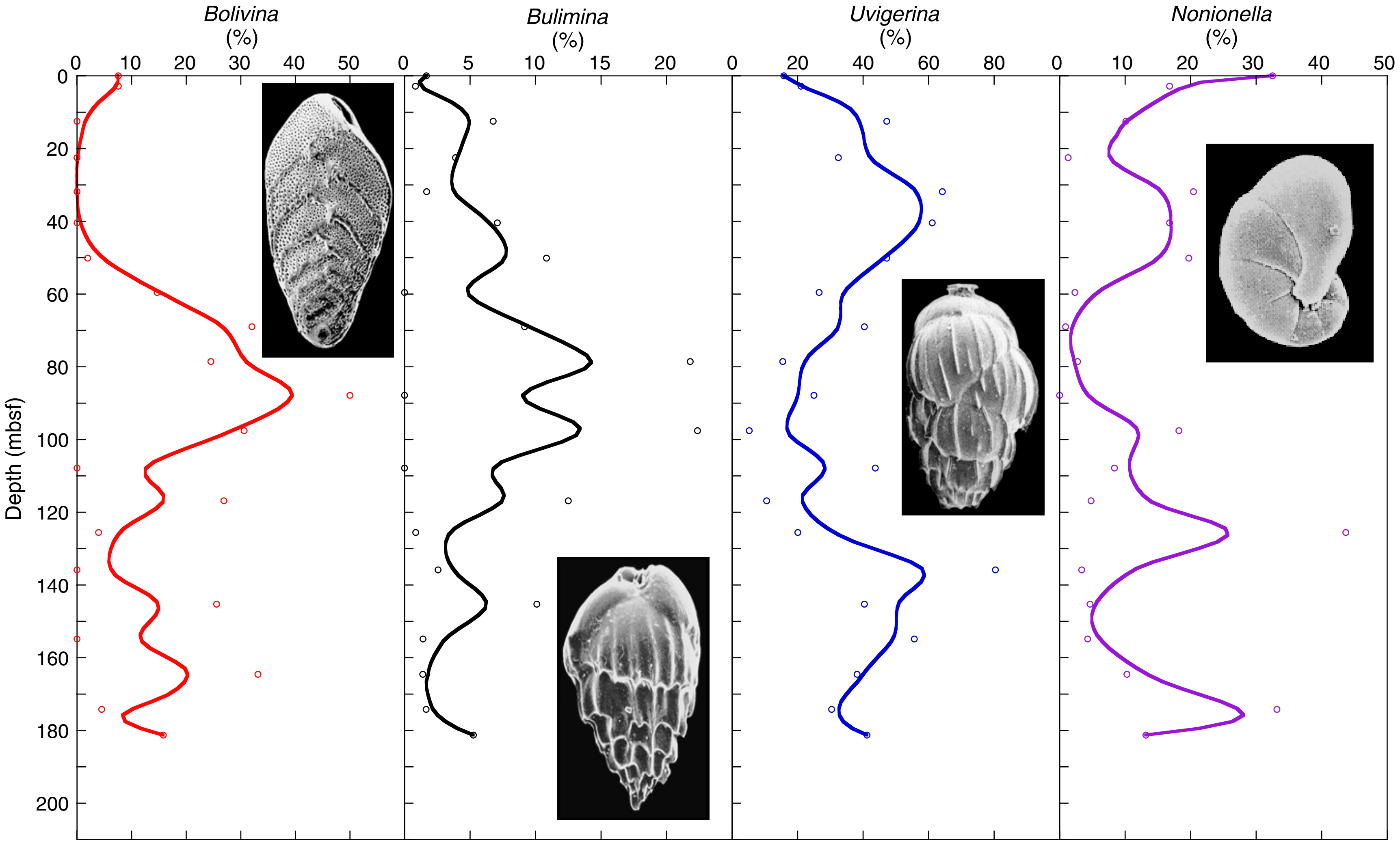

Figure F20. Initial natural remanent magnetization (NRM) and demagnetized NRM (25 mT AF) intensity for Hole 1235A.

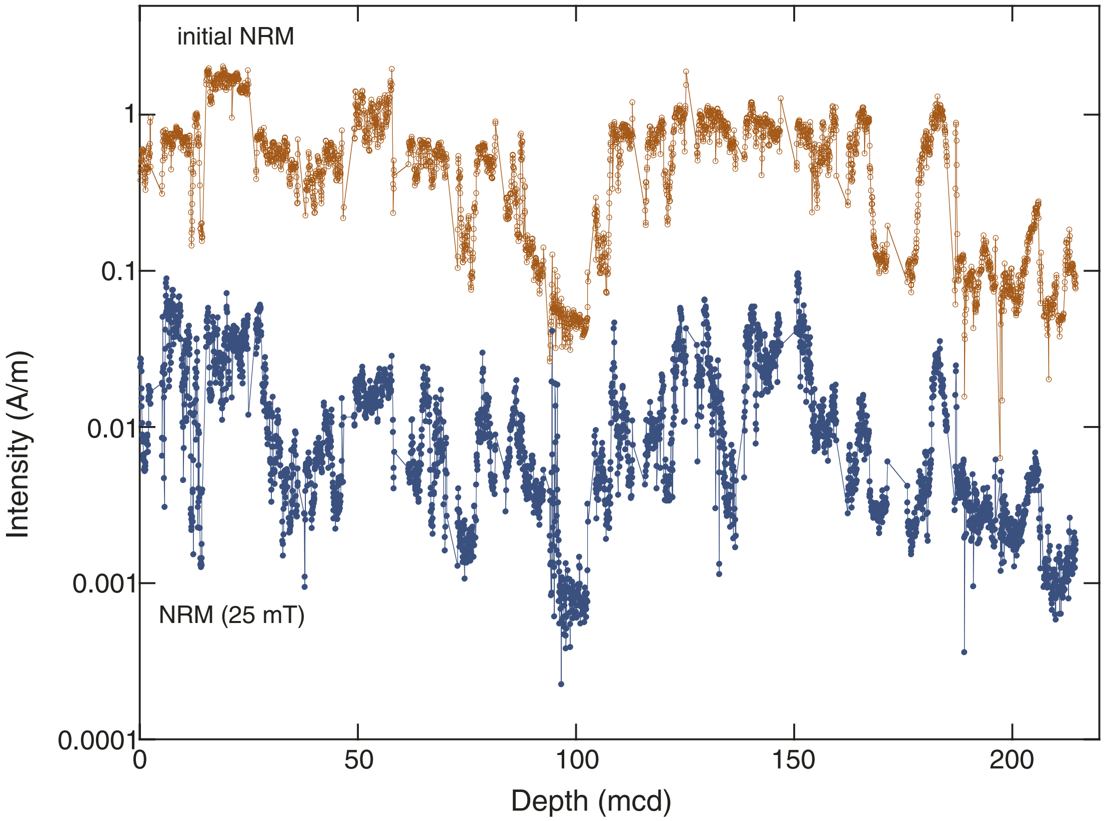

Figure F21. **A.** Initial natural remanent magnetization (NRM) and AF demagnetized inclinations (25 mT) for the upper 70 mcd of Hole 1235A. Individual cores are noted. The APC temperature (APCT) tool was used when recovering Cores 202-1235A-3H and 6H. **B.** Initial NRM and AF demagnetized inclinations (25 mT) for the upper 70 mcd of Hole 1235C. Individual cores are noted. The nonmagnetic core barrel was used on the odd-numbered cores.

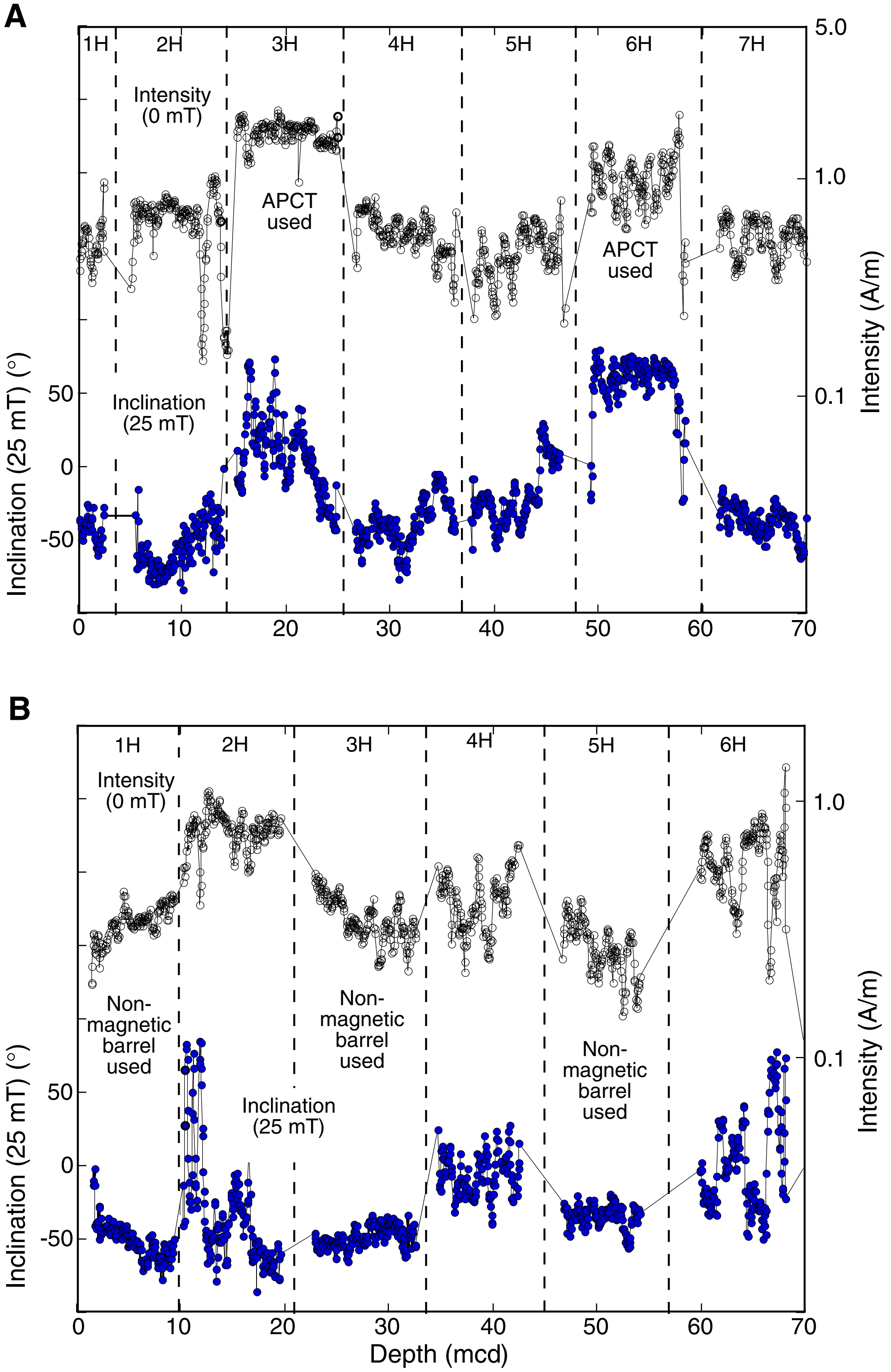

Figure F22. NRM inclination after demagnetization at 20 or 25 mT for Holes 1235A, 1235B, and 1235C (left) and NRM declination after demagnetization at 20 or 25 mT for Holes 1235A, 1235B, and 1235C (right). Average declinations for each core have been returned to a mean of zero.

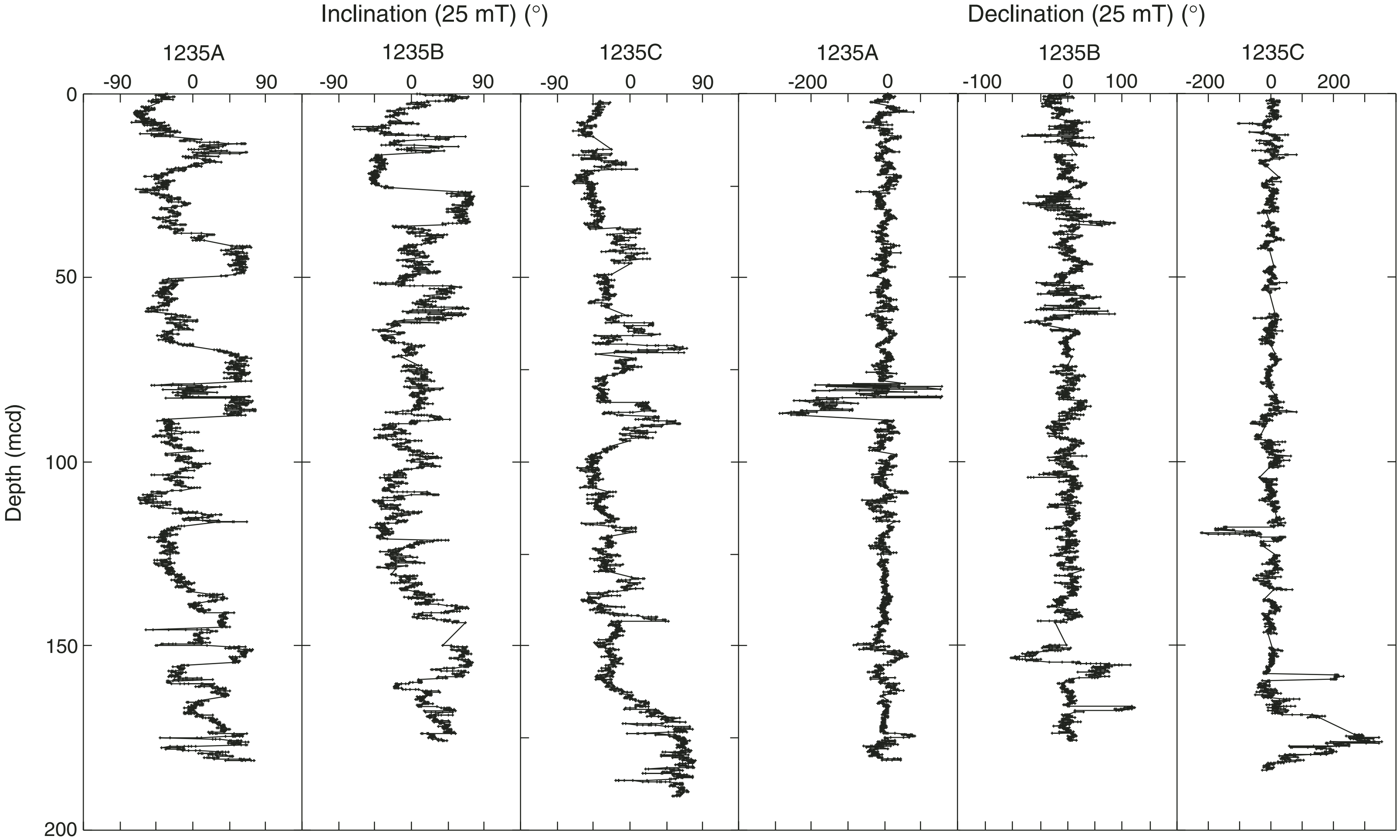

Figure F23. Statistical assessment of magnetic overprint strength in Holes 1235A, 1235B, and 1235C. **A–C.** Initial NRM inclination and AF demagnetized inclination (25 mT). **D–F.** Initial NRM intensity and AF demagnetized NRM (25 mT) intensity. APCT = APC temperature tool.

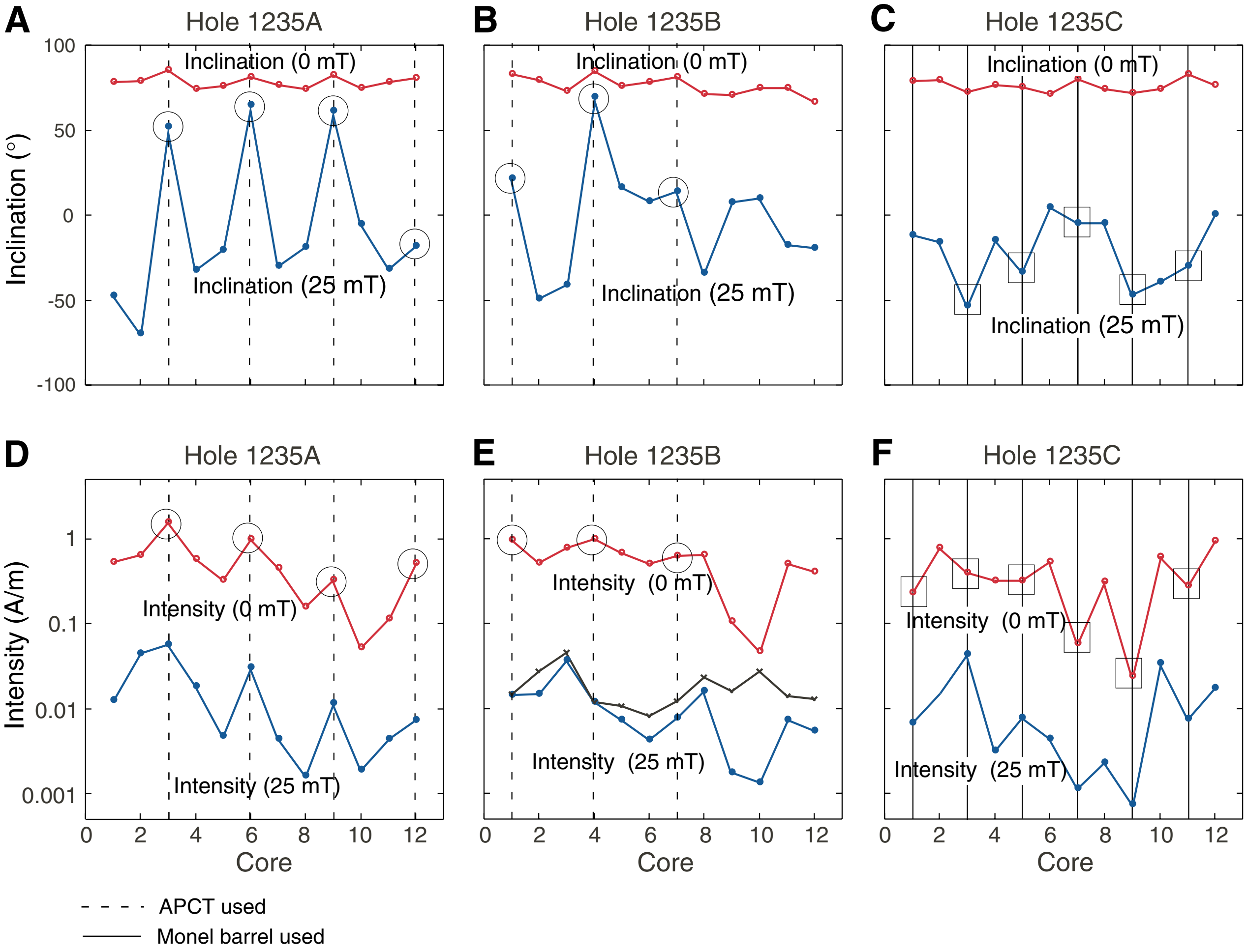

Figure F24. Declinations (20 or 25 mT) for the Site 1235 splice and Holes 1235A, 1235B, and 1235C in the uppermost 35 mbsf. Selected declination features are tentatively correlated among the three holes.

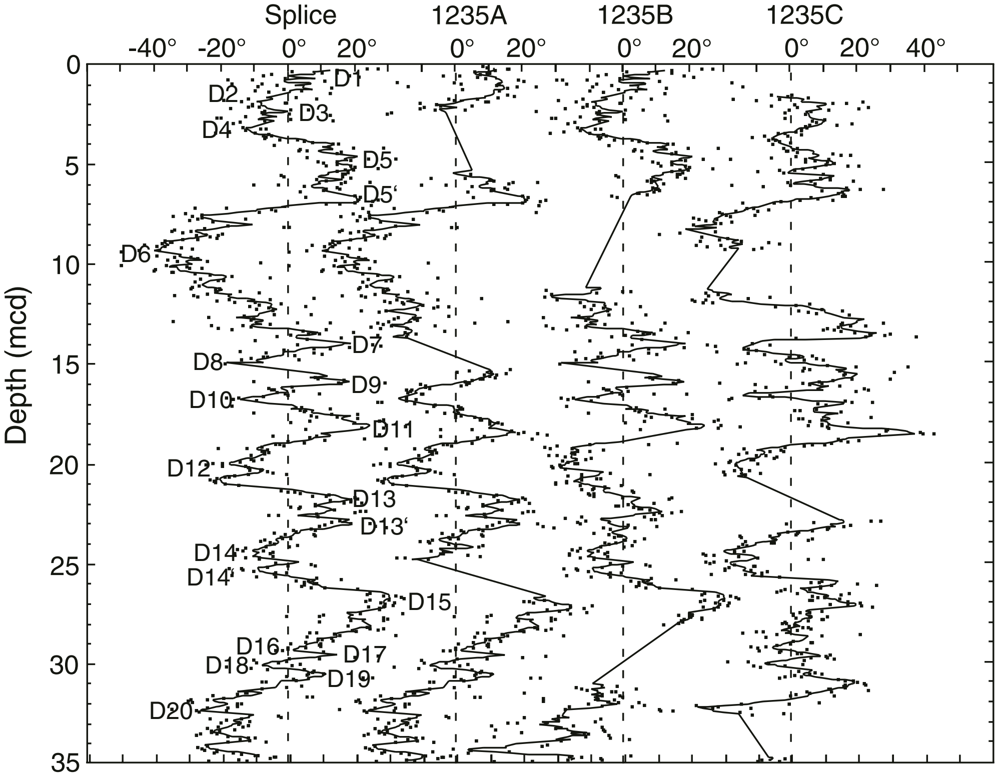

Figure F25. Headspace and vacutainer methane (C_1) concentrations and C_1/C_2 ratio in sediments from Hole 1235A vs. depth. Because of the direct sampling method, vacutainer gas concentrations are higher than headspace gas concentrations. Open circles = headspace, solid circles = vacutainer.

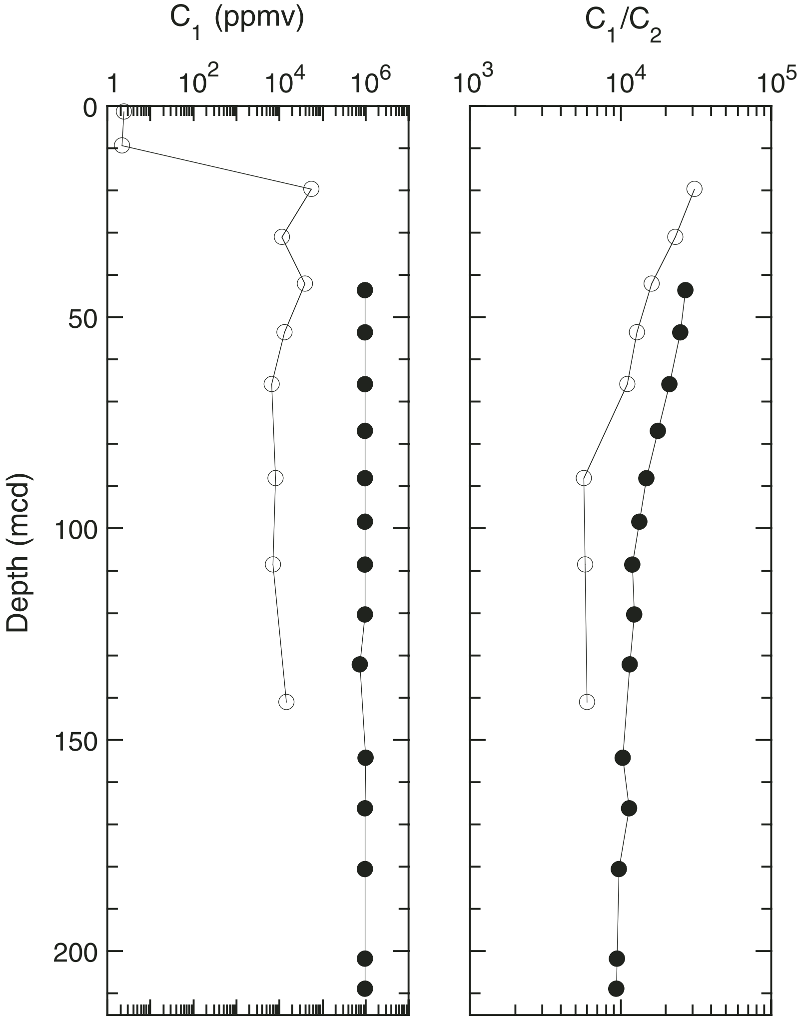

Figure F26. Interstitial water geochemical data, Site 1235. Values below the detection limits (0.6 mM for sulfate, 0.5 µM for iron, and 0.3 mM for ammonium) are plotted at zero. Open squares = calcium concentrations.

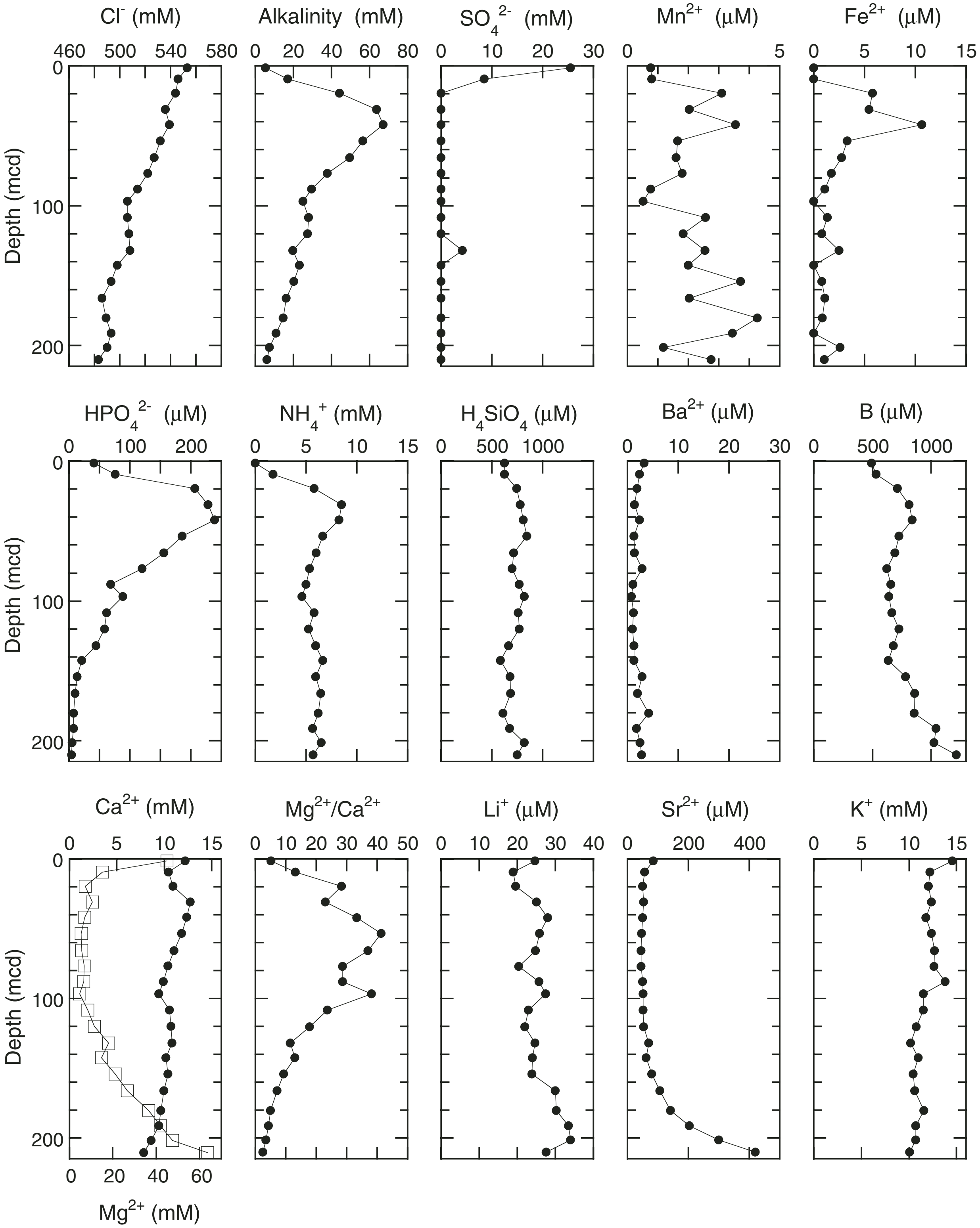

Figure F27. Calcium carbonate ($CaCO_3$), total organic carbon (TOC), and total nitrogen (TN) concentrations, and TOC/TN vs. depth in sediments from Site 1235. Data from Holes 1235A and 1235B are used to constitute single profiles in meters composite depth.

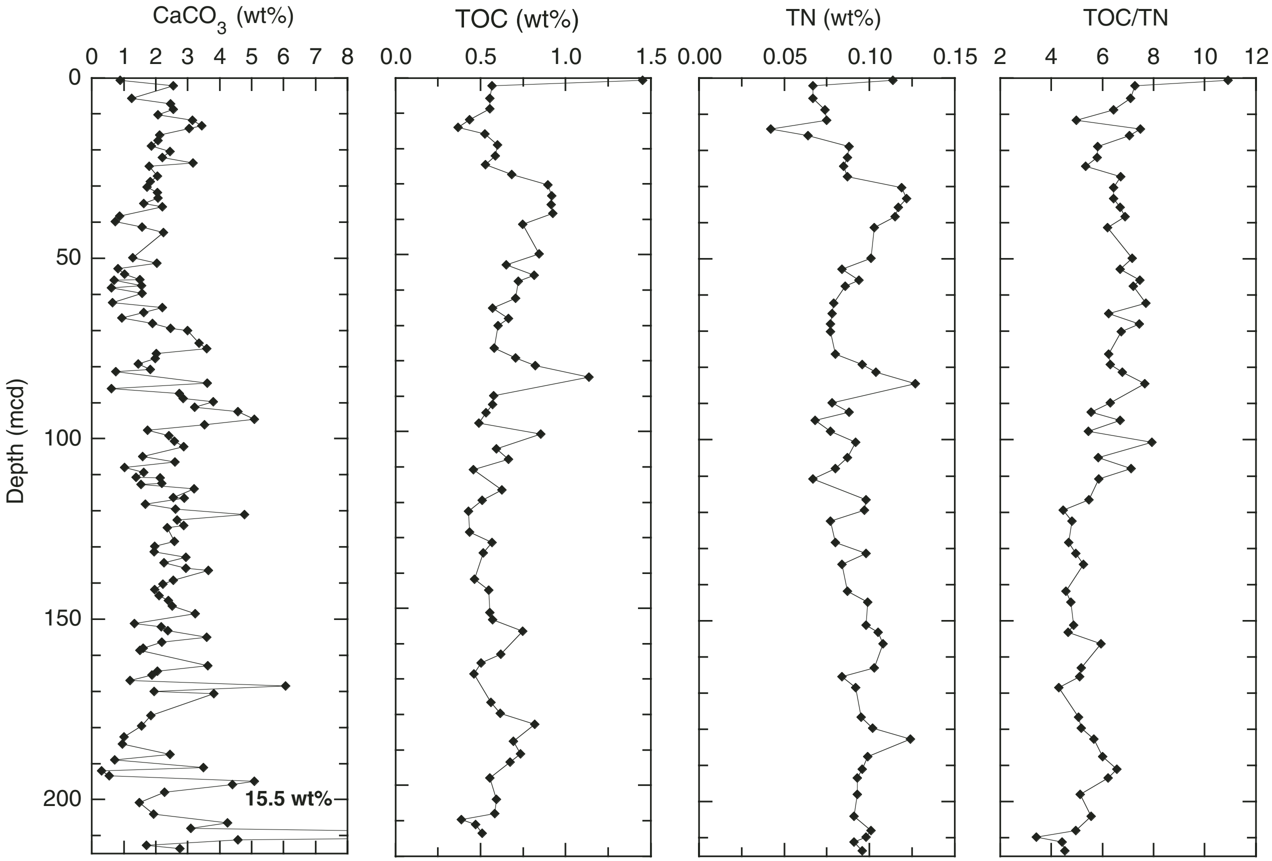

Figure F28. Total nitrogen (TN) vs. total organic carbon (TOC) and TOC/TN vs. TOC in sediments at Site 1235.

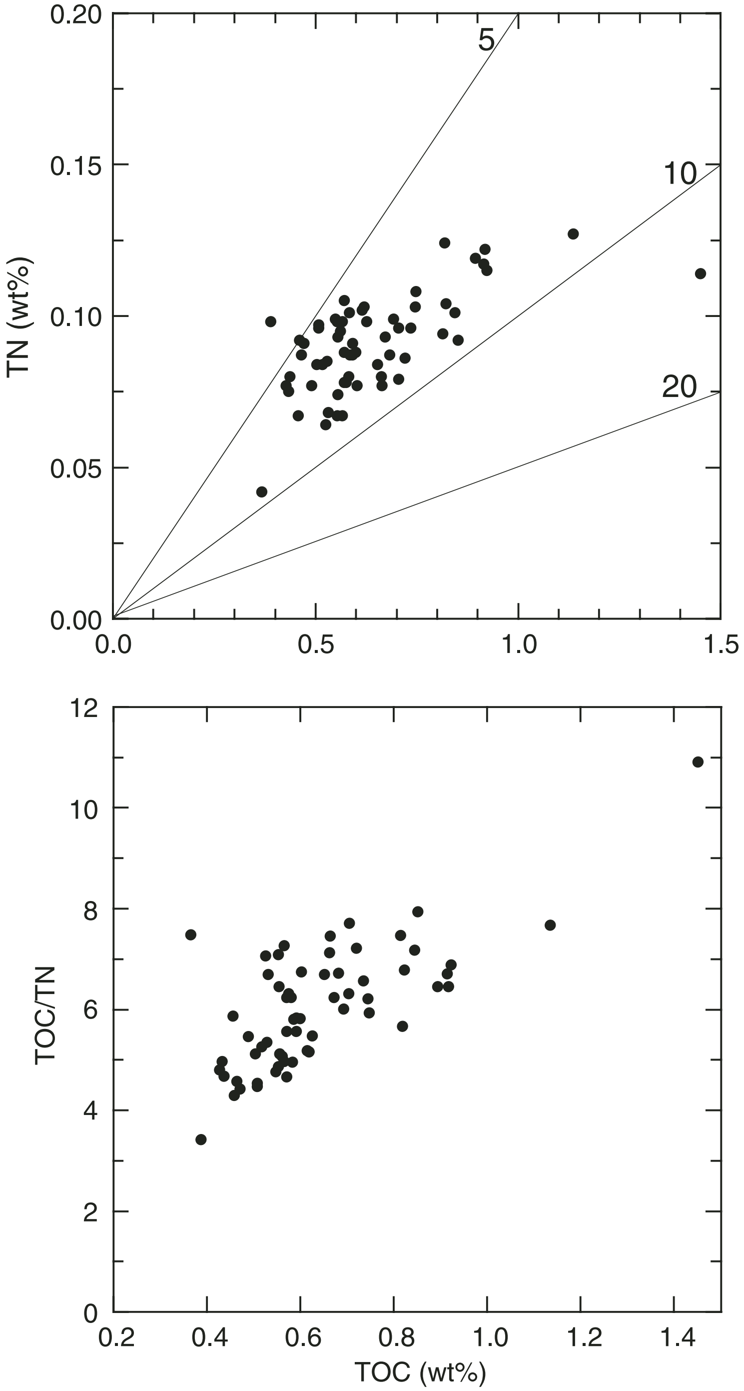

Figure F29. S_2 vs. total organic carbon (TOC) and hydrogen index (HI) vs. TOC in selected samples from Site 1235. Boundaries for Types I, II, and III kerogen fields are taken from Langford and Blanc-Valleron (1990).

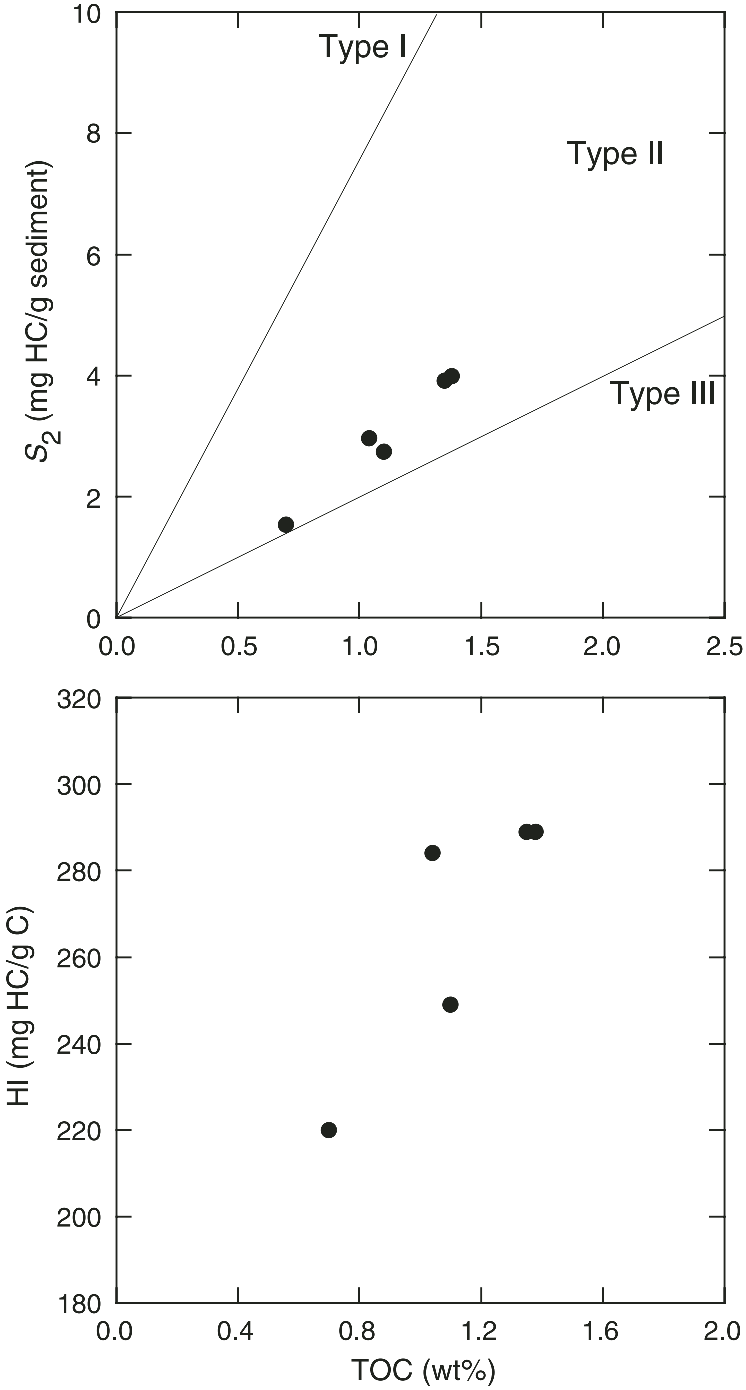

Table T1. Operations summary, Site 1235.

Core	Date (Apr 2002)	Local time (hr)	Depth (mbsf)		Length (m)		Recovery (%)	APCT	Orientation	NMCB
			Top	Bottom	Cored	Recovered				
202-1235A-										
1H	17	0610	0.0	2.8	2.8	2.87	102.5			
2H	17	0645	2.8	12.3	9.5	9.89	104.1			
3H	17	0735	12.3	21.8	9.5	10.24	107.8	X		
4H	17	0803	21.8	31.3	9.5	10.11	106.4		Tensor	
5H	17	0826	31.3	40.8	9.5	9.24	97.3		Tensor	
6H	17	0910	40.8	50.3	9.5	9.33	98.2	X	Tensor	
7H	17	0935	50.3	59.8	9.5	9.36	98.5		Tensor	
8H	17	0955	59.8	69.3	9.5	9.25	97.4		Tensor	
9H	17	1038	69.3	78.8	9.5	9.33	98.2	X	Tensor	
10H	17	1110	78.8	88.3	9.5	9.13	96.1		Tensor	
11H	17	1150	88.3	97.8	9.5	9.45	99.5		Tensor	
12H	17	1250	97.8	107.3	9.5	10.05	105.8	X	Tensor	
13H	17	1320	107.3	116.8	9.5	9.62	101.3		Tensor	
14H	17	1400	116.8	126.3	9.5	8.87	93.4		Tensor	
15H	17	1430	126.3	135.8	9.5	9.67	101.8		Tensor	
16H	17	1500	135.8	145.3	9.5	9.53	100.3		Tensor	
17H	17	1530	145.3	154.8	9.5	9.55	100.5		Tensor	
18H	17	1555	154.8	164.3	9.5	9.79	103.1		Tensor	
19H	17	1645	164.3	173.8	9.5	9.91	104.3		Tensor	
20H	17	1715	173.8	181.3	7.5	7.59	101.2		Tensor	
				Cored totals:	181.3	182.78	100.8			
202-1235B-										
1H	17	2105	0.0	7.0	7.0	7.00	100.0	X		
2H	17	2140	7.0	16.5	9.5	9.88	104.0			
3H	17	2210	16.5	26.0	9.5	9.69	102.0		Tensor	
4H	17	2259	26.0	35.5	9.5	10.38	109.3	X	Tensor	
5H	17	2325	35.5	45.0	9.5	9.94	104.6		Tensor	
6H	17	2358	45.0	54.5	9.5	10.21	107.5		Tensor	
7H	18	0048	54.5	64.0	9.5	9.34	98.3	X	Tensor	
8H	18	0125	64.0	73.5	9.5	7.97	83.9		Tensor	
9H	18	0200	73.5	83.0	9.5	10.02	105.5		Tensor	
10H	18	0235	83.0	92.5	9.5	9.80	103.2		Tensor	
11H	18	0305	92.5	102.0	9.5	9.89	104.1		Tensor	
12H	18	0350	102.0	111.5	9.5	10.16	107.0		Tensor	
13H	18	0420	111.5	121.0	9.5	9.58	100.8		Tensor	
14H	18	0450	121.0	130.5	9.5	8.70	91.6		Tensor	
15H	18	0540	130.5	140.0	9.5	9.70	102.1		Tensor	
16H	18	0620	140.0	149.5	9.5	9.89	104.1		Tensor	
17H	18	0650	149.5	159.0	9.5	9.56	100.6		Tensor	
18H	18	0725	159.0	168.5	9.5	9.31	98.0		Tensor	
19H	18	0810	168.5	176.2	7.7	7.79	101.2		Tensor	
				Cored totals:	176.2	178.81	101.5			
202-1235C-										
1H	18	1115	0.5	10.0	9.5	9.25	97.4	X		X
2H	18	1145	10.0	19.5	9.5	9.97	105.0			
3H	18	1220	19.5	29.0	9.5	10.11	106.4		Tensor	X
4H	18	1245	29.0	38.5	9.5	8.37	88.1		Tensor	
5H	18	1315	38.5	48.0	9.5	8.33	87.7		Tensor	X
6H	18	1342	48.0	57.5	9.5	8.82	92.8		Tensor	
7H	18	1415	57.5	67.0	9.5	9.77	102.8		Tensor	X
8H	18	1450	67.0	76.5	9.5	9.15	96.3		Tensor	
9H	18	1520	76.5	86.0	9.5	9.56	100.6		Tensor	X
10H	18	1550	86.0	95.5	9.5	9.84	103.6		Tensor	
11H	18	1635	95.5	105.0	9.5	8.79	92.5		Tensor	X
12H	18	1700	105.0	114.5	9.5	10.08	106.1		Tensor	
13H	18	1750	114.5	124.0	9.5	9.79	103.1		Tensor	
14H	18	1815	124.0	133.5	9.5	10.21	107.5		Tensor	
15H	18	1852	133.5	143.0	9.5	9.98	105.1		Tensor	
16H	18	1955	143.0	152.5	9.5	9.81	103.3		Tensor	
				Cored totals:	152.0	151.83	99.9			
				Site totals:	509.5	513.42	100.8			

Notes: APCT = advanced piston corer temperature tool (stainless-steel housing is cutting shoe). NMCB = nonmagnetic core barrel, including cutting shoe (made from monel). X = APCT or NMCB was used. Tensor = brand name for core-barrel orientation tool.

Table T2. Composite depth scale, Site 1235.

	Depth of core top		Depth offset		Translation to cmcd	
Core	Drillers (mbsf)	Composite (mcd)	Cumulative (m)	Differential (m)	Growth factor*	Depth (cmcd)†
202-1235A-						
1H	0.0	0.00	0.00		1.20	0.00
2H	2.8	4.90	2.10	2.10	1.20	4.08
3H	12.3	15.10	2.80	0.70	1.20	12.58
4H	21.8	26.65	4.85	2.05	1.20	22.21
5H	31.3	37.24	5.94	1.09	1.20	31.03
6H	40.8	48.78	7.98	2.04	1.20	40.65
7H	50.3	61.20	10.90	2.92	1.20	51.00
8H	59.8	72.42	12.62	1.72	1.20	60.35
9H	69.3	83.51	14.21	1.59	1.20	69.59
10H	78.8	93.62	14.82	0.61	1.20	78.02
11H	88.3	103.87	15.57	0.75	1.20	86.56
12H	97.8	115.45	17.65	2.08	1.20	96.21
13H	107.3	127.28	19.98	2.33	1.20	106.07
14H	116.8	138.17	21.37	1.39	1.20	115.14
15H	126.3	150.12	23.82	2.45	1.20	125.10
16H	135.8	161.89	26.09	2.27	1.20	134.91
17H	145.3	175.55	30.25	4.16	1.20	146.29
18H	154.8	186.44	31.64	1.39	1.20	155.37
19H	164.3	196.84	32.54	0.90	1.20	164.03
20H	173.8	206.86	33.06	0.52	1.20	172.38
202-1235B-						
1H	0.0	0.10	0.10		1.20	0.08
2H	7.0	10.90	3.90	3.80	1.20	9.08
3H	16.5	18.80	2.30	–1.60	1.20	15.67
4H	26.0	30.61	4.61	2.31	1.20	25.51
5H	35.5	41.39	5.89	1.28	1.20	34.49
6H	45.0	54.04	9.04	3.15	1.20	45.03
7H	54.5	65.92	11.42	2.38	1.20	54.93
8H	64.0	76.54	12.54	1.12	1.20	63.78
9H	73.5	85.63	12.13	–0.41	1.20	71.36
10H	83.0	97.87	14.87	2.74	1.20	81.56
11H	92.5	107.52	15.02	0.15	1.20	89.60
12H	102.0	119.57	17.57	2.55	1.20	99.64
13H	111.5	131.34	19.84	2.27	1.20	109.45
14H	121.0	142.87	21.87	2.03	1.20	119.06
15H	130.5	154.39	23.89	2.02	1.20	128.66
16H	140.0	163.94	23.94	0.05	1.20	136.62
17H	149.5	179.58	30.08	6.14	1.20	149.65
18H	159.0	189.63	30.63	0.55	1.20	158.03
19H	168.5	200.57	32.07	1.44	1.20	167.14
202-1235C-						
1H	0.5	0.61	0.11		1.20	0.51
2H	10.0	10.10	0.10	–0.01	1.20	8.42
3H	19.5	22.70	3.20	3.10	1.20	18.92
4H	29.0	34.70	5.70	2.50	1.20	28.92
5H	38.5	45.87	7.37	1.67	1.20	38.23
6H	48.0	59.44	11.44	4.07	1.20	49.53
7H	57.5	70.15	12.65	1.21	1.20	58.46
8H	67.0	81.54	14.54	1.89	1.20	67.95
9H	76.5	92.03	15.53	0.99	1.20	76.69
10H	86.0	103.68	17.68	2.15	1.20	86.40
11H	95.5	114.20	18.70	1.02	1.20	95.17
12H	105.0	124.86	19.86	1.16	1.20	104.05
13H	114.5	136.96	22.46	2.60	1.20	114.13
14H	124.0	149.51	25.51	3.05	1.20	124.59
15H	133.5	159.54	26.04	0.53	1.20	132.95
16H	143.0	173.72	30.72	4.68	1.20	144.77

Notes: * = calculated based on mbsf-mcd relationship for splice shown in Figure F6, p. 27. † = within the splice, the following equations apply: cmcd = mcd/growth factor; mcd = mbsf + cumulative depth offset; mcd = cmcd x growth factor; mbsf = cmcd x growth factor – cumulative offset. This table is also available in ASCII.

Table T3. OSUS-MS measurements, Hole 1235A.

Core, section, interval (cm)	Depth		Magnetic susceptibility (instrument units)	Run number	Depth from top of core (cm)
	(mbsf)	(mcd)			
202-1235A-					
1H-1, 5	0.05	0.05	125	432	5
1H-1, 10	0.10	0.10	157	432	10
1H-1, 15	0.15	0.15	169	432	15
1H-1, 20	0.20	0.20	176	432	20
1H-1, 25	0.25	0.25	185	432	25
1H-1, 30	0.30	0.30	185	432	30
1H-1, 35	0.35	0.35	192	432	35
1H-1, 40	0.40	0.40	196	432	40
1H-1, 45	0.45	0.45	189	432	45
1H-1, 50	0.50	0.50	193	432	50
1H-1, 55	0.55	0.55	199	432	55
1H-1, 60	0.60	0.60	204	432	60
1H-1, 65	0.65	0.65	201	432	65
1H-1, 70	0.70	0.70	198	432	70
1H-1, 75	0.75	0.75	196	432	75
1H-1, 80	0.80	0.80	186	432	80
1H-1, 85	0.85	0.85	171	432	85
1H-1, 90	0.90	0.90	165	432	90
1H-1, 95	0.95	0.95	160	432	95
1H-1, 100	1.00	1.00	150	432	100
1H-1, 105	1.05	1.05	144	432	105
1H-1, 110	1.10	1.10	100	432	110
1H-1, 115	1.15	1.15	126	432	115
1H-1, 120	1.20	1.20	116	432	120
1H-1, 125	1.25	1.25	100	432	125
1H-1, 130	1.30	1.30	117	432	130
1H-1, 135	1.35	1.35	130	432	135
1H-1, 140	1.40	1.40	133	432	140
1H-2, 5	1.55	1.55	154	433	155
1H-2, 10	1.60	1.60	168	433	160
1H-2, 15	1.65	1.65	162	433	165
1H-2, 20	1.70	1.70	156	433	170
1H-2, 25	1.75	1.75	170	433	175
1H-2, 30	1.80	1.80	151	433	180
1H-2, 35	1.85	1.85	140	433	185
1H-2, 40	1.90	1.90	151	433	190
1H-2, 45	1.95	1.95	171	433	195
1H-2, 50	2.00	2.00	202	433	200
1H-2, 55	2.05	2.05	217	433	205
1H-2, 60	2.10	2.10	210	433	210
1H-2, 65	2.15	2.15	216	433	215
1H-2, 70	2.20	2.20	206	433	220
1H-2, 75	2.25	2.25	209	433	225
1H-2, 80	2.30	2.30	216	433	230
1H-2, 85	2.35	2.35	215	433	235
1H-2, 90	2.40	2.40	215	433	240
1H-2, 95	2.45	2.45	217	433	245
1H-2, 100	2.50	2.50	218	433	250
1H-2, 105	2.55	2.55	212	433	255
2H-1, 5	2.85	4.95	225	434	5
2H-1, 10	2.90	5.00	224	434	10
2H-1, 15	2.95	5.05	245	434	15
2H-1, 20	3.00	5.10	239	434	20
2H-1, 25	3.05	5.15	249	434	25
2H-1, 30	3.10	5.20	262	434	30
2H-1, 35	3.15	5.25	279	434	35
2H-1, 40	3.20	5.30	280	434	40
2H-1, 45	3.25	5.35	248	434	45
2H-1, 50	3.30	5.40	243	434	50
2H-1, 55	3.35	5.45	225	434	55
2H-1, 60	3.40	5.50	199	434	60
2H-1, 65	3.45	5.55	181	434	65
2H-1, 70	3.50	5.60	213	434	70

Note: Only a portion of this table appears here. The complete table is available in ASCII.

Table T4. OSUS-MS measurements, Hole 1235B.

Core, section, interval (cm)	Depth		Magnetic susceptibility (instrument units)	Run number	Depth from top of core (cm)
	(mbsf)	(mcd)			
202-1235B-					
1H-1, 5	0.05	0.15	157	567	5
1H-1, 10	0.10	0.20	171	567	10
1H-1, 15	0.15	0.25	180	567	15
1H-1, 20	0.20	0.30	177	567	20
1H-1, 25	0.25	0.35	174	567	25
1H-1, 30	0.30	0.40	181	567	30
1H-1, 35	0.35	0.45	186	567	35
1H-1, 40	0.40	0.50	195	567	40
1H-1, 45	0.45	0.55	193	567	45
1H-1, 50	0.50	0.60	189	567	50
1H-1, 55	0.55	0.65	181	567	55
1H-1, 60	0.60	0.70	179	567	60
1H-1, 65	0.65	0.75	185	567	65
1H-1, 70	0.70	0.80	182	567	70
1H-1, 75	0.75	0.85	180	567	75
1H-1, 80	0.80	0.90	168	567	80
1H-1, 85	0.85	0.95	153	567	85
1H-1, 90	0.90	1.00	138	567	90
1H-1, 95	0.95	1.05	135	567	95
1H-2, 5	1.56	1.66	206	568	155
1H-2, 10	1.61	1.71	188	568	160
1H-2, 15	1.66	1.76	157	568	165
1H-2, 20	1.71	1.81	158	568	170
1H-2, 25	1.76	1.86	173	568	175
1H-2, 30	1.81	1.91	157	568	180
1H-2, 35	1.86	1.96	163	568	185
1H-2, 40	1.91	2.01	197	568	190
1H-2, 45	1.96	2.06	211	568	195
1H-2, 50	2.01	2.11	197	568	200
1H-2, 55	2.06	2.16	196	568	205
1H-2, 60	2.11	2.21	215	568	210
1H-2, 65	2.16	2.26	209	568	215
1H-2, 70	2.21	2.31	215	568	220
1H-2, 75	2.26	2.36	205	568	225
1H-2, 80	2.31	2.41	197	568	230
1H-2, 85	2.36	2.46	208	568	235
1H-2, 90	2.41	2.51	209	568	240
1H-2, 95	2.46	2.56	202	568	245
1H-3, 5	3.06	3.16	239	569	305
1H-3, 10	3.11	3.21	257	569	310
1H-3, 15	3.16	3.26	258	569	315
1H-3, 20	3.21	3.31	253	569	320
1H-3, 25	3.26	3.36	256	569	325
1H-3, 30	3.31	3.41	253	569	330
1H-3, 35	3.36	3.46	242	569	335
1H-3, 40	3.41	3.51	234	569	340
1H-3, 45	3.46	3.56	233	569	345
1H-3, 50	3.51	3.61	237	569	350
1H-3, 55	3.56	3.66	246	569	355
1H-3, 60	3.61	3.71	258	569	360
1H-3, 65	3.66	3.76	245	569	365
1H-3, 70	3.71	3.81	274	569	370
1H-3, 75	3.76	3.86	282	569	375
1H-3, 80	3.81	3.91	291	569	380
1H-3, 85	3.86	3.96	304	569	385
1H-3, 90	3.91	4.01	332	569	390
1H-3, 95	3.96	4.06	328	569	395
1H-4, 5	4.56	4.66	247	570	455
1H-4, 10	4.61	4.71	253	570	460
1H-4, 15	4.66	4.76	279	570	465
1H-4, 20	4.71	4.81	297	570	470
1H-4, 25	4.76	4.86	298	570	475
1H-4, 30	4.81	4.91	291	570	480

Note: Only a portion of this table appears here. The complete table is available in **ASCII**.

Table T5. OSUS-MS measurements, Hole 1235C.

Core, section, interval (cm)	Depth (mbsf)	Depth (mcd)	Magnetic susceptibility (instrument units)	Run number	Depth from top of core (cm)
202-1235C-					
1H-1, 5	0.55	0.66	228	697	5
1H-1, 10	0.60	0.71	191	697	10
1H-1, 15	0.65	0.76	173	697	15
1H-1, 20	0.70	0.81	143	697	20
1H-1, 25	0.75	0.86	181	697	25
1H-1, 30	0.80	0.91	179	697	30
1H-1, 35	0.85	0.96	182	697	35
1H-1, 40	0.90	1.01	151	697	40
1H-1, 45	0.95	1.06	131	697	45
1H-1, 50	1.00	1.11	136	697	50
1H-2, 5	1.07	1.18	80	698	155
1H-2, 10	1.12	1.23	94	698	160
1H-2, 15	1.17	1.28	88	698	165
1H-2, 20	1.22	1.33	97	698	170
1H-2, 25	1.27	1.38	112	698	175
1H-2, 30	1.32	1.43	126	698	180
1H-2, 35	1.37	1.48	115	698	185
1H-2, 40	1.42	1.53	124	698	190
1H-2, 45	1.47	1.58	149	698	195
1H-2, 50	1.52	1.63	186	698	200
1H-2, 55	1.57	1.68	187	698	205
1H-2, 60	1.62	1.73	169	698	210
1H-2, 65	1.67	1.78	152	698	215
1H-2, 70	1.72	1.83	157	698	220
1H-2, 75	1.77	1.88	159	698	225
1H-2, 80	1.82	1.93	174	698	230
1H-2, 85	1.87	1.98	198	698	235
1H-2, 90	1.92	2.03	206	698	240
1H-2, 95	1.97	2.08	209	698	245
1H-2, 100	2.02	2.13	182	698	250
1H-2, 105	2.07	2.18	151	698	255
1H-2, 110	2.12	2.23	144	698	260
1H-2, 115	2.17	2.28	182	698	265
1H-2, 120	2.22	2.33	186	698	270
1H-2, 125	2.27	2.38	179	698	275
1H-2, 130	2.32	2.43	192	698	280
1H-2, 135	2.37	2.48	212	698	285
1H-2, 140	2.42	2.53	215	698	290
1H-2, 145	2.47	2.58	207	698	295
1H-3, 5	2.57	2.68	219	699	305
1H-3, 10	2.62	2.73	224	699	310
1H-3, 15	2.67	2.78	218	699	315
1H-3, 20	2.72	2.83	207	699	320
1H-3, 25	2.77	2.88	221	699	325
1H-3, 30	2.82	2.93	224	699	330
1H-3, 35	2.87	2.98	231	699	335
1H-3, 40	2.92	3.03	241	699	340
1H-3, 45	2.97	3.08	244	699	345
1H-3, 50	3.02	3.13	251	699	350
1H-3, 55	3.07	3.18	243	699	355
1H-3, 60	3.12	3.23	243	699	360
1H-3, 65	3.17	3.28	254	699	365
1H-3, 70	3.22	3.33	258	699	370
1H-3, 75	3.27	3.38	245	699	375
1H-3, 80	3.32	3.43	249	699	380
1H-3, 85	3.37	3.48	250	699	385
1H-3, 90	3.42	3.53	252	699	390
1H-3, 95	3.47	3.58	250	699	395
1H-3, 100	3.52	3.63	254	699	400
1H-3, 105	3.57	3.68	259	699	405
1H-3, 110	3.62	3.73	259	699	410
1H-3, 115	3.67	3.78	245	699	415
1H-3, 120	3.72	3.83	236	699	420

Note: Only a portion of this table appears here. The complete table is available in ASCII.

Table T6. Splice tie points, Site 1235

Core, section, interval (cm)	Depth				Core, section, interval (cm)	Depth		
	(mbsf)	(mcd)	(cmcd)			(mbsf)	(mcd)	(cmcd)
202-					202-			
1235A-1H-2, 80.0	2.30	2.30	1.92	Tie	1235B-1H-2, 70.0	2.20	2.30	1.92
1235B-1H-4, 140.0	5.90	6.00	5.00	Tie	1235A-2H-1, 110.0	3.90	6.00	5.00
1235A-2H-6, 25.0	10.55	12.65	10.54	Tie	1235C-2H-2, 105.0	12.55	12.65	10.54
1235C-2H-4, 120.0	15.70	15.80	13.17	Tie	1235A-3H-1, 70.0	13.00	15.80	13.17
1235A-3H-4, 50.0	17.30	20.10	16.75	Tie	1235B-3H-1, 130.0	17.80	20.10	16.75
1235B-3H-5, 30.0	22.80	25.10	20.92	Tie	1235C-3H-2, 90.0	21.90	25.10	20.92
1235C-3H-6, 5.0	27.05	30.25	25.21	Tie	1235A-4H-3, 60.0	25.40	30.25	25.21
1235A-4H-7, 45.0	31.25	36.10	30.08	Tie	1235C-4H-1, 140.0	30.40	36.10	30.08
1235C-4-H-6, 10.0	36.54	42.24	35.20	Tie	1235B-5H-1, 85.0	36.35	42.24	35.20
1235B-5H-4, 130.0	41.30	47.19	39.33	Tie	1235C-5H-1, 130.5	39.82	47.19	39.33
1235C-5H-5, 45.0	44.81	52.18	43.48	Tie	1235A-6H-3, 40.0	44.20	52.18	43.48
1235A-6H-5, 55.0	47.33	55.31	46.09	Tie	1235B-6H-1, 125.5	46.27	55.31	46.09
1235B-6H-7, 85.0	54.85	63.89	53.24	Append	1235B-8H-1, 0.0	64.00	76.54	63.78
1235B-8H-6, 40.0	71.32	83.86	69.88	Tie	1235A-9H-1, 35.0	69.65	83.86	69.88
1235A-9H-4, 10.0	73.68	87.89	73.24	Tie	1235B-9H-2, 74.0	75.76	87.89	73.24
1235B-9H-7, 75.0	83.25	95.38	79.48	Append	1235A-11H-1, 0.0	88.30	103.87	86.56
1235A-11H-5, 35.0	94.55	110.12	91.77	Tie	1235B-11H-3, 40.0	95.10	110.12	91.77
1235B-11H-8, 45.0	102.14	117.16	97.63	Append	1235A-15H-1, 0.0	126.30	150.12	125.10
1235A-15H-4, 100.0	131.10	154.92	129.10	Tie	1235B-15H-1, 52.0	131.03	154.92	129.10
1235B-15H-7, 40.0	139.90	163.79	136.49	Append	1235A-17H-1, 0.0	145.30	175.55	146.29
1235A-17H-5, 30.0	151.60	181.85	151.54	Tie	1235B-17H-2, 75.5	151.77	181.85	151.54
1235B-17H-7, 110.0	158.36	188.44	157.03					

Note: This table is also available in ASCII.

Table T7. Lithologic Unit I, Site 1235.

	Top			Base				
		Depth			Depth			
Unit	Core	(mbsf)	(mcd)	Core	(mbsf)	(mcd)	Description	Interpretation
	202-			202-				
I	1235A-1H	0.0	0.0	1235A-20H	181.4	214.5	Dark olive gray to gray silty clay, with occasional minor abundances of nannofossils and diatoms	Hemipelagic sequence
	1235B-1H	0.0	0.1	1235B-19H	176.3	208.4		
	1235C-1H	0.5	0.6	1235C-16H	152.9	183.6		

Table T8. Distribution of calcareous nannofossils, Hole 1235A.

Core, section, interval (cm)	Depth (mbsf)	Depth (mcd)	Preservation	Abundance	*Braarudosphaera bigelowii*	*Calcidiscus leptoporus*	*Coccolithus pelagicus*	*Emiliania huxleyi*	*Gephyrocapsa oceanica* (large)	*Gephyrocapsa* spp. (*G. caribbeanica*) (medium)	*Gephyrocapsa* spp. (*G. muellerae*) (medium)	*Gephyrocapsa* spp. (small)	*Helicosphaera carteri*
202-1235A-													
1H-2, 40	1.90	1.90	G	C		F	R	C			C	F	R
1H-CC, 20	2.82	2.82	G	C		R	R	C	R		C	C	R
2H-3, 40	6.22	8.32	M	C			F	C			C	F	R
2H-CC, 23	12.50	14.60	M	C		R	R	C	R		C	F	R
3H-3, 40	15.73	18.53	G	C		R	R	C			F	F	R
3H-CC, 38	22.54	25.34	G	C		R	R	C		R	C	F	R
4H-1, 40	22.20	27.05	M	F			F	R			F		
4H-2, 40	23.71	28.56		B									
4H-3, 40	25.22	30.07	M	R				R			R		R
4H-4, 40	26.72	31.57	M	R		R	R	R			F		R
4H-5, 40	28.23	33.08	M	R				R			R		R
4H-6, 40	29.74	34.59	M	F		R		R		R	F		R
4H-CC, 22	31.92	36.77	G	R				R				R	
5H-3, 40	34.70	40.64	M	R		R		R			R	R	
5H-CC, 27	40.46	46.40	M	R		R	R	R			R	R	
6H-3, 40	44.21	52.19	M	C		R	F	R			C	F	R
6H-CC, 43	50.12	58.10	M	C				R	F	F	F	F	
7H-3, 40	53.53	64.43	M	F		R	R	R	R		F	R	R
7H-CC, 29	59.64	70.54	M	A		R	R	R	F	F	A	F	
8H-3, 40	63.07	75.69		B									
8H-4, 40	64.46	77.08	M	C		R	F	R			C	C	
8H-CC, 20	69.03	81.65	M	C		R	R	R			C	F	
9H-3, 40	72.65	86.86	M	C		R	R	R			C	C	R
9H-CC, 34	78.60	92.81		B									
10H-3, 40	82.22	97.04		B									
10H-4, 40	83.73	98.55		B									
10H-5, 40	85.23	100.05		B									
10H-CC, 16	87.94	102.76		B									
11H-3, 40	91.67	107.24	M	C		R	R	R			C	F	F
11H-CC, 34	97.66	113.23	G	A		F	R	F			C	C	R
12H-3, 40	101.19	118.84	M	C		F	R	F			C	C	R
12H-CC, 42	107.81	125.46	G	A		R	R	R			C	C	R
13H-3, 40	110.71	130.69	M	R		F		R			R	R	
13H-CC, 34	116.91	136.89	G	A		R	R	R			C	C	F
14H-3, 40	119.74	141.11	M	C		R	R	R			C	F	R
14H-CC, 22	125.63	147.00	G	A		F					C	C	R
15H-3, 40	128.96	152.78	M	C		R		R			F	C	R
15H-CC, 26	135.96	159.78	P	R			R	R					R
16H-3, 40	138.68	164.77	m	F		F	R	R			F	F	R
16H-CC, 22	145.31	171.40	M	C		F	F	R			C	F	
17H-3, 40	148.72	178.97	P	R		R	R	R				R	
17H-CC, 18	154.87	185.12	P	R			R					R	
18H-3, 40	158.19	189.83	P	R		R			R	?		R	
18H-CC, 23	164.61	196.25	F	P			F				F		F
19H-3, 40	167.71	200.25	R	M		R	R	R			R	R	
19H-CC, 30	174.23	206.77	M	C			F				C		F
20H-3, 20	175.36	208.42	P	F			R		R	F	R		F
20H-7, 40	180.42	213.48	P	C		R	R	R			R	C	
20H-CC, 1	181.33	214.39	P	F			R		R	F			R

Notes: Preservation: G = good, M = moderate, P = poor. Abundance: A = abundant, C = common, F = few, R = rare, B = barren.

Table T9. Distribution of foraminifers, Hole 1235A. (Continued on next page.)

Core, section interval (cm)	Depth (mbsf)	Depth (mcd)	Preparation	Preservation	Abundance	Remarks	Benthic/planktonic foraminifers (%)	*Globigerina bulloides*	*Globigerinita glutinata*	*Globorotalia inflata*	*Globorotalia ruber*	*Globorotalia scitula*	*Globorotalia truncatulinoides*	*Neogloboquadrina dutertrei*	*Neogloboquadrina pachyderma* (d)	*Neogloboquadrina pachyderma* (s)	*Orbulina universa*	*Bolivina costata*	*Bolivina seminuda*	*Bolivina* sp. 1	*Bulimina mexicana*	*Cassidulina teretis*	*Cassidulinoides bradyi*	*Cibicidoides* spp.	*Ehrenbergina serrata*	*Eubuliminella exilis*	*Fissurina* spp.
202-1235A-																											
Mudline	0.00	0.00	S	M	C	Radiolarians: R; Glauconite: F	35/65	C	C	R	R	R	C	C	F	F		9			1		1	2		2	
1H-CC, 20	2.82	2.82	S	M	C	Radiolarians: R; sponge spicules, mica	35/65	F	F	C			C	F	F	F	F	8		1				8		1	
2H-CC, 23	12.50	14.60	S	M	F	Radiolarians: R; sponge spicules, mica	40/60	C		F		R	F		F	F						6			3		
3H-CC, 38	22.54	25.34	S	M	C		15/85	C	F	C				F	R	R	R					2	1	3		1	
4H-CC, 22	31.92	36.77	S	M	C	Radiolarians: R; Silica: A	75/25	C	F	R			C	F	R	R	R						8			3	
5H-CC, 27	40.46	46.40	S	M	C	Radiolarians: F	44/56	C	F	R			R	F	R	R	R									8	
6H-CC, 43	50.12	58.10	S	M	A	Radiolarians: R	65/35	C	F	R			R	F	R	R	R	4								22	
7H-CC, 29	59.64	70.54	S	M	C	Radiolarians: R Large shell fragments	60/40	F	F	R			A	F			R	19		19							
8H-CC, 20	69.03	81.65	S	M	C	Radiolarians: R; Phosphate: C	65/35	F	F	F		R	C	R	R	R		4	31							10	
9H-CC, 34	78.60	92.81	S	M	F	Glauconite: A; pyritized burrows	35/65	R	F	C			C	C	R	R		24	3							24	
10H-CC, 16	87.94	102.76	S	P	T	Radiolarians: R; Glauconite A; phosphate			R				R						2								
11H-CC, 34	97.66	113.23	S	G	C	Radiolarians: R; fish debris, teeth	35/65	C	F				R	C	R	R		52								38	
12H-CC, 42	107.81	125.46	S	M	C	Radiolarians: R	40/60	F	F	R			R	F	F	R							8	4			3
13H-CC, 34	116.91	136.89	S	M	F	Pyritized burrows	35/65	F	F				F	F	F	R		12	2	14			9	1		13	
14H-CC, 22	125.63	147.00	S	M	F		55/45	F	F	R		F		F	F	R				9		2	3	2			5
15H-CC, 26	135.96	159.78	S	M	C	Radiolarians: C	90/10	C	F	F			R		R	R	R									3	
16H-CC, 22	145.31	171.40	S	M	C	Radiolarians: R	60/40	C	F	C		R	C	R	F			33					1	2		13	
17H-CC, 18	154.87	185.12	S	M	F	Radiolarians: F	92/8	F	F	C		R	C	F	R											2	
18H-CC, 23	164.61	196.25	S	M	C	Radiolarians: R; Glauconite: C; Diatoms: F; Radiolarians: F	60/40	C	F	C		R	R	R	R			8	62	1			2			3	1
19H-CC, 30	174.23	206.77	S	M	C	Radiolarians: R	55/45	C	F	A		R	R	R	R		R		11				3	5		4	8
20H-CC, 1	181.33	214.39	S	G	C		58/42	C	F	C		R	F	R	R				18				2	3		6	

Notes: Preparation: S = sieve. Preservation: G = good, M = moderate, P = poor. Abundance: A = abundance, C = common, F = few, T = trace.

Table T9 (continued).

Core	Depth (mbsf)	Depth (mcd)	Preparation	Preservation	Abundance	*Globobulimina affinis*	*Globobulimina pyrula*	*Globulina prisca*	*Globulina* spp.	*Gyroidinoides orbicularis*	*Hoeglundina elegans*	*Melonis affinis*	*Melonis* spp.	*Nonionella auris*	*Nuttallides umbonifera*	*Oolina* spp.	*Oolina sulcata*	*Planulina wuellerstorfi*	*Praeglobobulimina spinescens*	*Protoglobobulimina pupoides*	*Pyrgo serrata*	*Pyrgo* spp.	*Quinqueloculina* spp.	*Rutherfordoides mexicanus*	*Rotaliatinopsis semiinvoluta*	*Textularia* sp. 1	*Trifarina tricarinata*	*Uvigerina peregrina*
202-1235A-																												
Mudline	0.00	0.00	S	M	C	2	2	2		1				39				1					1	23	15			19
1H-CC, 20	2.82	2.82	S	M	C		7							20	1	1				6			1	35	5			25
2H-CC, 23	12.50	14.60	S	M	F	9						2		9		2	1	6			3		3		3			42
3H-CC, 38	22.54	25.34	S	M	C		8			1				1	1					21	1		6	2	4			25
4H-CC, 22	31.92	36.77	S	M	C									36				16										113
5H-CC, 27	40.46	46.40	S	M	C	4	1							19			1	4		3				4				69
6H-CC, 43	50.12	58.10	S	M	A	17	1							40				14		4	2		1			2		96
7H-CC, 29	59.64	70.54	S	M	C	32	2						1	6	1							3	1	53	53			69
8H-CC, 20	69.03	81.65	S	M	C	5								1			2	2						4	6			44
9H-CC, 34	78.60	92.81	S	M	F	1								3		1		6					1	24	6			17
10H-CC, 16	87.94	102.76	S	P	T	1																						1
11H-CC, 34	97.66	113.23	S	G	C	11								31	7			2					11		9			9
12H-CC, 42	107.81	125.46	S	M	C	37	5							13		2		9			1	1			4			68
13H-CC, 34	116.91	136.89	S	M	F					2		1	1	5	6	1	1	1	5	2	5	6	5		1			11
14H-CC, 22	125.63	147.00	S	M	F								1	100	3	4		4			2		8		39	1		46
15H-CC, 26	135.96	159.78	S	M	C	8								4				1						4	3			94
16H-CC, 22	145.31	171.40	S	M	C	4								6		1		2					1	4	10			52
17H-CC, 18	154.87	185.12	S	M	F									6				12					3	24	15			78
18H-CC, 23	164.61	196.25	S	M	C	3			1		2			22	1		1							6	18		1	82
19H-CC, 30	174.23	206.77	S	M	C				1				1	81			1	3					4	6	41		1	74
20H-CC, 1	181.33	214.39	S	G	C	1								15	2			8						6	6			47

Table T10. Distribution of diatoms, Hole 1235A. (**See table notes.** Continued on next page.)

Core, section, interval (cm)	Depth (mbsf)	Depth (mcd)	Identification	Method	Abundance	Preservation	*Actinocyclus curvatulus*	*Actinoptychus senarius*	*Aulacoseira granulata*	*Azpeitia nodulifera*	*Chaetoceros* spp. (resting spores)	*Delphineis* spp.	*Fragilariopsis doliolus*	*Hemidiscus cuneiformis*	*Paralia sulcata*	*Pseudonitzschia* spp.	*Roperia tesselata*	*Thalassionema nitzschioides*	*Thalassiosira* spp.	Freshwater benthic	Freshwater species (planktonic)	Marine benthic species	Marine neritic species (other)	Marine pelagic species (other) COSM	Marine pelagic species (other) WW	Marine pelagic species (other) CW	Remarks
202-1235A-																											
1H-1, 0–1	0.00	0.00	PAL	S	C	G		R	T	F	C	F				R			F		T	T	C–A	T	R		
1H-CC, 20–25	2.82	2.82	PAL	S	F	M	R			T	F	F						F	R			F	T				
2H-2, 40	4.71	6.81	Toothpick	S	F–C	M					F–C	F							F	T	T		T				
2H-4, 40	7.72	9.82	Toothpick	S	F–C	P					F–C	T			T				R	T	T		R				
2H-CC, 23–28	12.50	14.60	PAL	S	R–F	P–M		R			F	F				T		R	R	T	T	F	R–F	T	T		
3H-3, 40	15.73	18.53	Toothpick	S	C	M					C								F			R	F				
3H-CC, 38–43	22.54	25.34	PAL	S	C	M–G					C	R				R		T	F			R	F	T			
4H-3, 40	25.22	30.07	Toothpick	S	C	G					C		T						F								
4H-CC, 22–27	31.92	36.77	PAL	S	C–A	M					C–A								R								
5H-2, 40	33.20	39.14	Toothpick	S	C–A	M				T	C	R						R	R								
5H-3, 40	34.70	40.64	Toothpick	S	C	M–G					C	T							F	T	T	R					Very small specimens
5H-4, 40	36.20	42.14	Toothpick	S	F–C	M					F	R						T					T		T		
5H-CC, 27–32	40.46	46.40	PAL	S	C	M					C								R–F			T			T		
6H-2, 40	42.69	50.67	Toothpick	S	F	M			T		F–C									T	T				T		
6H-3, 40	44.21	52.19	Toothpick	S	C	M					C								F–C		R						
6H-4, 40	45.70	53.68	Toothpick	S	F–C	M		T			C	T							R								
6H-CC, 43–48	50.12	58.10	PAL	S	R	P					R								T								
7H-3, 40	53.53	64.43	Toothpick	S	F	M				R	F								F			T	T				
7H-CC, 29–34	59.64	70.54	PAL	S	R	P					R–F								R								
8H-3, 40	63.06	75.68	Toothpick	S	C	M				R	C					R		F	F		T	R	R				
8H-CC, 20–25	69.03	81.65	PAL	S	R–F	P		T			R–F					T			T								
9H-3, 40	72.64	86.85	Toothpick	S	F	P–M		R	F		F	R			R			R–F	F		F	R–F					
9H-CC, 34–39	78.60	92.81	PAL	S	F–C	M		R		R	C	F				R		F	F			R					
10H-2, 40	80.70	95.52	Toothpick	S	F–C	M		R			F–C	T						F	R–F	R	R		T		R		
10H-4, 40	83.70	98.52	Toothpick	S	R	P					R–F	T							T				R				
10H-6, 40	86.70	101.52	Toothpick	S	F	P	T				F								T			T					
10H-CC, 16–21	87.94	102.76	PAL	S	R	P		T			R–F	T						T	T	T	T		T				
11H-3, 40	91.70	107.27	Toothpick	S	F–C	M				R	C							R	F			R	F			T	
11H-CC, 34–39	97.67	113.23	PAL	S	F	P					F	R						R	F		T	T	R			T	
12H-3, 40	101.20	118.85	Toothpick	S	F–C	M	R			R	F–C	F						F	F			R–F				R	
12H-CC, 42–47	107.81	125.46	PAL	S	F	M–P					F					T		T	R			T					
13H-3, 40	110.65	130.63	Toothpick	S	C	M			R		C							T	C		R	C	F				Frequent *Cocconeis*
13H-CC, 34–39	116.91	136.89	PAL	S	F–C	M–P				R	F–C	R							R–F			T				T	
14H-2, 40	118.23	139.60	Toothpick	S	R–F	P					R–F				T			T	R								
14H-3, 40	119.73	141.10	Toothpick	S	F–C	M					F–C	R						R	F								
14H-CC, 22–27	125.63	147.00	PAL	S	F	M–P					F							R	F				R				
15H-3, 40	129.00	152.82	Toothpick	S	F–C	M					F–C	T				R			F–C				F				Increase in small sizes and *Thalassirosira*

Table T10 (continued).

Core, section, interval (cm)	Depth (mbsf)	Depth (mcd)	Identification	Method	Abundance	Preservation	*Actinocyclus curvatulus*	*Actinoptychus senarius*	*Aulacoseira granulata*	*Azpeitia nodulifera*	*Chaetoceros* spp. (resting spores)	*Delphineis* spp.	*Fragilariopsis doliolus*	*Hemidiscus cuneiformis*	*Paralia sulcata*	*Pseudonitzschia* spp.	*Roperia tesselata*	*Thalassionema nitzschioides*	*Thalassiosira* spp.	Freshwater benthic	Freshwater species (planktonic)	Marine benthic species	Marine neritic species (other)	Marine pelagic species (other) COSM	Marine pelagic species (other) WW	Marine pelagic species (other) CW	Remarks
15H-4, 40	130.50	154.32	Toothpick	S	A	M				T	A	T						T	C			T	F				*Nitzschia reinholdii* (reworked)
15H-CC, 26–31	135.96	159.78	PAL	S	C	M					C	R–F							F								
16H-2, 40	137.67	163.76	Toothpick	S	F	M					R–F	R–F										T	T		T		
16H-6, 40	143.16	169.25	Toothpick	S	F	M		T			F	T							R–F			T	T				
16H-CC, 22–27	145.31	171.40	PAL	S	R–F	M					F	T							F			T					*Denticulopsis* (reworked Miocene diatom)
17H-2, 40	147.20	177.45	Toothpick	S	C	M		T			C								R–F				T		T		
17H-3, 40	148.70	178.95	Toothpick	S	F–C	M					F–C							F	F		T						
17H-4, 40	150.30	180.55	Toothpick	S	F	M					F								R–F								*Denticulopsis* (reworked Miocene diatom)
17H-6, 40	153.10	183.35	Toothpick	S	C–A	M					C–A	R							F			T	T				
17H-CC, 18–23	154.87	185.12	PAL	S	C–A	M					A								T					T			
18H-2, 40	156.67	188.31	Toothpick	S	F	G–M				T	F	T		T				T	R				T				
18H-4, 40	159.67	191.31	Toothpick	S	C–A	M				R	A								F				T		R		
18H-6, 40	162.57	194.21	Toothpick	S	R–F	P					R–F							T					R		T		
18H-CC, 23–28	164.61	196.25	PAL	S	F	G–M					F							R–F									Presence of >63-µm cells of *Coscinodiscus*
19H-2, 40	166.20	198.74	Toothpick	S	R	P		T			R								T				T				
19H-4, 40	169.20	201.74	Toothpick	S	F	M–P					F					T		R	R								
19H-6, 40	172.20	204.74	Toothpick	S	T	P					R							T									
19H-CC, 30–35	174.23	206.77	PAL	S	F–C	M					F–C								F				R		R		
20H-2, 20	174.98	208.04	Toothpick	S	F	M					F	T						T	F						T		
20H-4, 40	175.89	208.95	Toothpick	S	F	M					R–F				T			R	F	T	T						
20H-6, 40	178.88	211.94	Toothpick	S	F	M		R			R				T			R	F				T	T			
20H-CC, 1	181.33	214.39	PAL	S	F	M–P			T		F							F	R		T						

Notes: PAL = paleontology sample. S = smear slide. Abundance: A = abundant, C = common, F = few, R = rare, T = trace. Preservation: G = good, M = moderate, P = poor. COSM = cosmopolitan forms, WW = warm-water forms, CW = cold-water forms.

Table T11. Headspace and vacutainer gas concentrations and C_1/C_2 ratio in sediments, Hole 1235A.

Core, section, interval (cm)	Depth (mbsf)	Depth (mcd)	Sample method	C_1 (ppmv)	C_2 (ppmv)	C_1/C_2	C_3 (ppmv)
202-1235A-							
1H-2, 0–5	1.50	1.50	HS	2			0.00
2H-4, 0–5	9.42	9.54	HS	2			0.00
3H-4, 0–5	19.63	19.70	HS	55,648	1.8	30,915	0.00
4H-4, 0–5	31.17	31.09	HS	11,522	0.5	23,045	0.00
5H-4, 0–5	41.74	42.17	HS	38,378	2.4	15,991	0.00
5H-5, 0–5	43.21	43.64	VAC	961,422	35.6	27,006	0.00
6H-4, 0–5	53.28	53.61	VAC	965,442	38.7	24,947	0.00
6H-4, 0–5	53.28	53.61	HS	12,867	1.0	12,867	0.00
7H-4, 0–5	65.54	65.87	VAC	967,312	45.8	21,130	1.29
7H-4, 0–5	65.54	65.87	HS	6,626	0.6	11,044	0.00
8H-4, 0–5	76.68	77.01	VAC	967,213	54.5	17,747	0.00
9H-4, 0–5	87.80	88.13	VAC	965,576	65.2	14,809	0.00
9H-4, 0–5	87.80	88.13	HS	7,983	1.4	5,702	0.00
10H-4, 0–5	98.15	98.48	VAC	957,908	72.2	13,267	0.00
11H-4, 0–5	108.25	108.60	VAC	971,090	81.0	11,989	0.00
11H-4, 0–5	108.25	108.60	HS	6,938	1.2	5,781	0.00
12H-4, 0–5	119.95	120.30	VAC	987,045	79.9	12,354	0.00
13H-4, 0–5	131.80	132.15	VAC	733,584	63.6	11,534	0.00
14H-3, 0–5	140.71	141.06	HS	14,398	2.4	5,999	0.00
15H-4, 0–5	153.89	154.24	VAC	988,379	95.6	10,339	0.00
16H-4, 0–5	165.87	166.22	VAC	984,751	86.0	11,451	0.00
17H-4, 0–5	180.18	180.53	VAC	985,657	100.6	9,798	0.00
19H-4, 0–5	201.37	201.72	VAC	986,524	104.2	9,468	1.00
20H-4, 0–5	208.57	208.92	VAC	984,224	105.3	9,347	0.00

Note: HS = headspace, VAC = vacutainer.

Table T12. Interstitial water data, Hole 1235A.

Core, section, interval (cm)	Depth (mbsf)	Depth (mcd)	pH	Alkalinity (mM)	Salinity	Cl^- (mM)	Na^+ (mM)	SO_4^{2-} (mM)	HPO_4^{2-} (µM)	NH_4^+ (mM)	H_4SiO_4 (µM)	Mn^{2+} (µM)	Fe^{2+} (µM)	Ca^{2+} (mM)	Mg^{2+} (mM)	B (µM)	Sr^{2+} (µM)	Ba^{2+} (µM)	Li^+ (µM)	K^+ (mM)
202-1235A-																				
1H-1, 145–150	1.45	1.45	7.78	5.3	35.0	553	468	25.5	41	BDL	624	0.8	BDL	10.3	53.3	492	85	3.3	25	14.6
2H-3, 145–150	7.27	9.37	7.90	16.9	33.0	546	469	8.4	76	1.76	624	0.8	BDL	3.5	45.7	532	57	2.4	19	12.2
3H-3, 145–150	16.78	19.58	7.87	44.1	34.0	544	477	BDL	207	5.80	746	3.1	5.8	1.7	47.8	713	50	1.8	19	12.1
4H-3, 145–150	26.27	31.12	7.88	63.8	35.0	536	471	BDL	228	8.50	778	2.0	5.5	2.4	55.8	812	51	1.4	25	12.4
5H-3, 145–150	35.75	41.69	7.80	67.3	35.0	539	483	BDL	239	8.23	810	3.5	10.7	1.6	54.1	841	51	2.4	28	11.8
6H-3, 143–148	45.24	53.22	7.93	56.6	34.0	532	470	BDL	186	6.64	845	1.7	3.3	1.2	51.8	730	46	1.3	26	12.4
7H-3, 145–150	54.58	65.48	7.99	49.6	33.0	527	465	BDL	156	6.00	713	1.6	2.8	1.3	48.2	692	45	1.4	25	12.7
8H-3, 134–139	64.01	76.63	8.04	37.9	32.0	522	453	BDL	120	5.35	700	1.8	1.8	1.6	45.5	623	45	2.9	20	12.6
9H-3, 124–134	73.49	87.70	7.93	29.6	31.0	514	440	BDL	68	5.00	768	0.8	1.1	1.5	43.4	659	49	1.0	26	13.8
10H-2, 140–150	81.71	96.53	7.89	25.0	31.0	506	435	BDL	88	4.59	818	0.5	BDL	1.0	41.2	642	52	0.8	27	11.5
11H-3, 130–140	92.57	108.14	8.04	27.9	31.0	506	426	BDL	62	5.78	758	2.6	1.3	2.0	46.1	668	51	1.2	23	11.5
12H-3, 140–150	102.19	119.84	8.01	27.4	31.0	507	425	BDL	58	5.24	771	1.8	0.8	2.6	46.9	726	53	1.0	22	10.7
13H-3, 140–150	111.71	131.69	7.94	19.8	31.0	508	423	4.2	44	5.94	663	2.5	2.5	4.1	47.4	681	69	1.2	25	10.2
14H-3, 150–160	120.84	142.21	8.13	23.3	30.0	498	414	BDL	21	6.64	585	2.0	BDL	3.4	44.6	637	62	1.3	24	11.0
15H-3, 140–150	129.96	153.78	8.01	20.3	30.0	493	402	BDL	13	5.94	678	3.7	0.8	4.8	45.4	786	80	2.9	24	10.5
16H-3, 140–150	139.68	165.77	7.96	16.4	31.0	486	392	BDL	10	6.47	684	2.0	1.1	6.1	43.6	863	106	2.0	30	10.6
17H-3, 150–160	149.82	180.07	8.15	14.6	30.0	489	391	BDL	7	6.21	611	4.3	0.8	8.4	42.1	857	142	4.2	30	11.6
18H-3, 140–150	159.19	190.83	7.91	10.9	29.0	493	392	BDL	7	5.65	672	3.4	BDL	9.6	41.2	1042	203	1.8	33	10.7
19H-3, 140–150	168.71	201.25	8.02	7.3	30.0	490	389	BDL	5	6.49	818	1.2	2.6	10.9	37.7	1025	300	2.5	34	10.7
20H-4, 140–150	176.91	209.97	7.82	6.0	28.0	483	381	BDL	4	5.71	750	2.8	1.1	14.6	34.3	1219	420	2.8	28	10.1

Note: BDL = below detection limit (SO_4^{2-} = ~0.6 mM, NH_4^+ = 0.3 mM, Fe^{2+} = 0.5 µM).

Table T13. Inorganic carbon, calcium carbonate, total carbon, total organic carbon, and total nitrogen concentrations, TOC/TN ratios total sulfur concentrations, and TOC/TS ratios, Hole 1235A. (**See table note.** Continued on next two pages.)

Core, section, interval (cm)	Depth		IC (wt%)	$CaCO_3$ (wt%)	TC (wt%)	TOC (wt%)	TN (wt%)	TOC/TN (atomic)	TS (wt%)	TOC/TS (atomic)
	(mbsf)	(mcd)								
202-1235A-										
1H-1, 74–75	0.74	0.74	0.11	0.9	1.56	1.45	0.11	10.91	0.57	2.55
1H-2, 74–75	2.24	2.24	0.31	2.6	0.88	0.57	0.07	7.26	0.96	0.59
2H-1, 74–75	3.54	5.64	0.15	1.2	0.70	0.55	0.07	7.09	0.53	1.05
2H-2, 74–75	5.05	7.15	0.30	2.5						
2H-3, 74–75	6.56	8.66	0.31	2.6	0.87	0.56	0.07	6.45	0.29	1.89
2H-4, 74–75	8.06	10.16	0.25	2.1						
2H-5, 74–75	9.57	11.67	0.38	3.2	0.81	0.43	0.07	4.97	0.58	0.74
2H-6, 74–75	11.08	13.18	0.41	3.4						
2H-7, 20–21	11.85	13.95	0.37	3.1	0.74	0.37	0.04	7.48	0.93	0.39
3H-1, 74–75	13.04	15.84	0.25	2.1	0.78	0.53	0.06	7.06	0.54	0.97
3H-2, 74–75	14.55	17.35	0.25	2.1						
3H-3, 74–75	16.07	18.87	0.22	1.9	0.82	0.60	0.09	5.82	0.67	0.89
3H-4, 74–75	17.57	20.37	0.29	2.5						
3H-5, 74–75	19.17	21.97	0.26	2.2	0.85	0.59	0.09	5.80	0.26	2.24
3H-6, 74–75	20.68	23.48	0.38	3.2						
3H-7, 20–21	21.65	24.45	0.22	1.8	0.75	0.53	0.08	5.35	0.39	1.35
4H-1, 74–75	22.54	27.39	0.25	2.1	0.93	0.68	0.09	6.72	0.54	1.27
4H-2, 74–75	24.05	28.90	0.22	1.8						
4H-3, 74–75	25.56	30.41	0.21	1.7	1.11	0.90	0.12	6.45	0.81	1.10
4H-4, 74–75	27.06	31.91	0.25	2.1						
4H-5, 74–75	28.57	33.42	0.25	2.1	1.17	0.92	0.12	6.45	0.61	1.50
4H-6, 74–75	30.08	34.93	0.20	1.6						
4H-7, 20–21	31.05	35.90	0.26	2.2	1.18	0.92	0.12	6.70	0.88	1.04
5H-1, 74–75	32.04	37.98	0.10	0.9	1.02	0.92	0.12	6.89	0.81	1.15
5H-2, 74–75	33.54	39.48	0.09	0.7						
5H-3, 74–75	35.04	40.98	0.19	1.6	0.94	0.75	0.10	6.21	0.70	1.07
5H-4, 74–75	36.54	42.48	0.27	2.2						
6H-1, 74–75	41.54	49.52	0.15	1.3	1.00	0.85	0.10	7.17	0.84	1.01
6H-2, 74–75	43.03	51.01	0.25	2.0						
6H-3, 74–75	44.55	52.53	0.10	0.8	0.75	0.65	0.08	6.69	0.82	0.79
6H-4, 74–75	46.04	54.02	0.12	1.0						
6H-5, 74–75	47.54	55.52	0.18	1.5	1.00	0.82	0.09	7.47	0.89	0.91
6H-6, 20–21	47.79	55.77	0.08	0.7						
6H-7, 20–21	49.30	57.28	0.19	1.6	0.91	0.72	0.09	7.22	0.91	0.79
202-1235B-										
6H-3, 74–75	48.75	57.79	0.07	0.6						
6H-4, 74–75	50.25	59.29	0.19	1.6						
202-1235A-										
7H-1, 74–75	51.04	61.94	0.08	0.7	0.79	0.71	0.08	7.71	0.62	1.15
7H-2, 74–75	52.36	63.26	0.26	2.2						
7H-3, 74–75	53.87	64.77	0.19	1.6	0.76	0.57	0.08	6.24	0.48	1.20
7H-4, 74–75	55.38	66.28	0.11	0.9						
7H-5, 74–75	56.86	67.76	0.23	1.9	0.90	0.67	0.08	7.45	0.64	1.04
7H-6, 74–75	58.28	69.18	0.30	2.5						
7H-7, 20–21	58.86	69.76	0.36	3.0	0.96	0.60	0.08	6.74	0.90	0.67
8H-1, 74–75	60.54	73.16	0.40	3.4						
8H-2, 74–75	62.05	74.67	0.43	3.6						
8H-3, 74–75	63.41	76.03	0.24	2.0	0.82	0.58	0.08	6.24	0.94	0.62
8H-4, 74–75	64.80	77.42	0.24	2.0						
8H-5, 74–75	66.30	78.92	0.18	1.5	0.89	0.71	0.10	6.31	0.47	1.49
8H-6, 74–75	67.80	80.42	0.22	1.8						
8H-7, 20–21	68.47	81.09	0.09	0.8	0.91	0.82	0.10	6.78	0.71	1.16
9H-1, 74–75	70.04	84.25	0.43	3.6	1.57	1.14	0.13	7.67	1.25	0.91
9H-2, 74–75	71.55	85.76	0.07	0.6						
9H-3, 74–75	72.99	87.20	0.33	2.7						
9H-4, 74–75	74.33	88.54	0.34	2.9						
9H-5, 20–21	75.29	89.50	0.46	3.8	1.04	0.58	0.08	6.31	1.36	0.42
9H-6, 20–21	76.80	91.01	0.39	3.2						
9H-7, 20–21	77.90	92.11	0.55	4.6	1.12	0.57	0.09	5.56	1.18	0.49
10H-1, 74–75	79.54	94.36	0.61	5.1	1.14	0.53	0.07	6.70	1.48	0.36
10H-2, 74–75	81.05	95.87	0.42	3.5						
10H-3, 74–75	82.56	97.38	0.21	1.7	0.70	0.49	0.08	5.45	1.39	0.35
10H-4, 74–75	84.07	98.89	0.29	2.4						

Table T13 (continued).

Core, section, interval (cm)	Depth		IC (wt%)	CaCO$_3$ (wt%)	TC (wt%)	TOC (wt%)	TN (wt%)	TOC/TN (atomic)	TS (wt%)	TOC/TS (atomic)
	(mbsf)	(mcd)								
10H-5, 74–75	85.57	100.39	0.31	2.9	1.16	0.85	0.09	7.93	1.71	0.50
10H-6, 74–75	87.09	101.91	0.34	2.9						
11H-1, 74–75	89.04	104.61	0.19	1.6	0.78	0.59	0.09	5.83	0.94	0.63
11H-2, 74–75	90.54	106.11	0.31	2.6						
11H-3, 74–75	92.01	107.58	0.12	1.0	0.78	0.66	0.08	7.12	0.73	0.91
11H-4, 74–75	93.42	108.99	0.20	1.6						
202-1235B-										
11H-3, 70–71	95.41	110.43	0.17	1.4						
202-1235A-										
11H-5, 74–75	94.91	110.48	0.26	2.1	0.72	0.46	0.07	5.86	0.64	0.71
11H-6, 74–75	96.40	111.97	0.26	2.2						
11H-7, 20–21	96.81	112.38	0.19	1.5						
202-1235B-										
11H-5, 80–81	98.52	113.54	0.38	3.2						
11H-7, 20–21	100.90	115.92	0.31	2.6						
202-1235A-										
12H-1, 74–75	98.54	116.19	0.35	2.9	0.98	0.63	0.10	5.48	0.76	0.82
12H-2, 80–81	100.10	117.75	0.32	1.7						
12H-3, 74–75	101.53	119.18	0.31	2.6	0.82	0.51	0.10	4.47	0.72	0.70
12H-4, 74–75	103.04	120.69	0.57	4.8						
12H-5, 74–75	104.54	122.19	0.32	2.7	0.75	0.43	0.08	4.80	0.75	0.57
12H-6, 74–75	106.05	123.70	0.34	2.9						
12H-7, 20–21	106.63	124.28	0.28	2.4						
13H-1, 74–75	108.04	128.02	0.31	2.6	0.75	0.44	0.08	4.67	0.70	0.63
13H-2, 74–75	109.59	129.57	0.24	2.0						
13H-3, 74–75	111.05	131.03	0.23	2.0	0.80	0.57	0.10	4.97	1.36	0.42
13H-4, 74–75	112.56	132.54	0.35	2.9						
13H-5, 74–75	114.06	134.04	0.27	2.3	0.79	0.52	0.08	5.26	1.01	0.51
13H-6, 74–75	115.53	135.51	0.35	2.9						
13H-7, 20–21	116.25	136.23	0.44	3.6						
14H-1, 74–75	117.54	138.91	0.31	2.6						
14H-2, 74–75	118.57	139.94	0.27	2.2						
14H-3, 74–75	120.08	141.45	0.24	2.0	0.71	0.47	0.09	4.57	1.01	0.46
14H-4, 74–75	121.68	143.05	0.25	2.1						
14H-5, 74–75	123.18	144.55	0.29	2.4	0.84	0.55	0.10	4.76	1.00	0.55
14H-6, 74–75	124.68	146.05	0.30	2.5						
202-1235B-										
14H-4, 74–75	126.26	148.13	0.39	3.2						
202-1235A-										
15H-1, 74–75	127.04	150.86	0.16	1.3	0.71	0.55	0.10	4.86	1.08	0.51
15H-2, 20–21	127.96	151.78	0.26	2.2						
15H-3, 50–51	129.06	152.88	0.29	2.4	0.86	0.57	0.11	4.66	0.85	0.67
15H-4, 74–75	130.81	154.63	0.43	3.6						
15H-5, 74–75	132.28	156.10	0.26	2.2	1.01	0.75	0.11	5.94	1.33	0.56
15H-6, 90–91	133.95	157.77	0.19	1.6						
15H-7, 20–21	134.52	158.34	0.18	1.5						
16H-1, 74–75	136.54	162.63	0.44	3.6	1.06	0.62	0.10	5.16	0.54	1.15
16H-2, 74–75	138.02	164.11	0.25	2.1						
16H-3, 74–75	139.02	165.11	0.23	1.9	0.73	0.50	0.08	5.12	1.11	0.45
16H-4, 74–75	140.52	166.61	0.14	1.2						
16H-5, 74–75	142.03	168.12	0.73	6.1	1.19	0.46	0.09	4.29	1.57	0.29
16H-6, 74–75	143.53	169.62	0.23	2.0						
16H-7, 20–21	144.26	170.35	0.46	3.8						
17H-1, 74–75	146.04	176.29	0.22	1.9	0.78	0.56	0.10	5.07	1.33	0.42
17H-3, 74–75	149.06	179.31	0.19	1.6	0.81	0.62	0.10	5.18	1.22	0.51
17H-5, 74–75	152.08	182.33	0.12	1.0	0.94	0.82	0.12	5.66	1.10	0.75
17H-7, 20–21	154.01	184.26	0.12	1.0						
18H-1, 74–75	155.54	187.18	0.29	2.5	0.98	0.69	0.10	6.01	1.25	0.55
18H-2, 74–75	157.02	188.66	0.09	0.7						
18H-3, 130–131	159.09	190.73	0.42	3.5	1.16	0.74	0.10	6.56	1.66	0.44
18H-4, 74–75	160.03	191.67	0.04	0.3						
18H-5, 74–75	161.45	193.09	0.07	0.6	0.74	0.67	0.09	6.23	2.10	0.32
18H-6, 74–75	162.96	194.60	0.61	5.1						
18H-7, 20–21	163.92	195.56	0.53	4.4						
19H-1, 74–75	165.04	197.58	0.27	2.3	0.83	0.56	0.09	5.12	1.90	0.29
19H-3, 74–75	168.05	200.59	0.18	1.5						

Table T13 (continued).

Core, section, interval (cm)	Depth (mbsf)	Depth (mcd)	IC (wt%)	$CaCO_3$ (wt%)	TC (wt%)	TOC (wt%)	TN (wt%)	TOC/TN (atomic)	TS (wt%)	TOC/TS (atomic)
19H-5, 74–75	171.08	203.62	0.23	1.9	0.82	0.59	0.09	5.56	2.07	0.29
19H-7, 20–21	173.54	206.08	0.51	4.3						
20H-1, 74–75	174.54	207.60	0.37	3.1	0.95	0.58	0.10	4.96	2.11	0.28
20H-4, 80–81	176.31	209.37	1.86	15.5	2.25	0.39	0.10	3.42	1.77	0.22
20H-5, 74–75	177.75	210.81	0.55	4.6	1.02	0.47	0.09	4.42	2.03	0.23
20H-6, 74–75	179.25	212.31	0.21	1.7						
20H-7, 20–21	180.22	213.28	0.33	2.8	0.84	0.51	0.10	4.54	1.61	0.32

Note: IC = inorganic carbon, TC = total carbon, TOC = total organic carbon, TN = total nitrogen, TS = total sulfur.

Table T14. Results of Rock-Eval pyrolysis analyses of selected sediment samples, Hole 1235A.

Core, section, interval (cm)	Depth (mbsf)	Depth (mcd)	TOC (wt%)	S_1 (mg/g)	S_2 (mg/g)	T_{max} (°C)	HI (mg HC/g C)
202-1235A-							
1H-1, 74–75	0.74	0.74	1.38	0.61	3.99	396	289
4H-5, 74–75	28.57	33.42	1.10	0.35	2.74	395	249
4H-7, 20–21	31.05	35.90	1.35	0.58	3.91	353	289
5H-1, 74–75	32.04	37.98	1.04	0.34	2.96	384	284
5H-3, 74–75	35.04	40.98	0.70	0.22	1.54	426	220

Notes: TOC = total organic carbon. S_1 = amount of volatile hydrocarbons, S_2 = amount of hydrocarbons due to thermal cracking of kerogen. T_{max} = peak temperature of kerogen breakdown. HI = hydrogen index ($100 \times S_2$/TOC).